Neural Mechanisms of Perceptual Decision-Making in the Fruit Fly



Long Hei Timothy Wong

Christ Church

University of Oxford

A thesis submitted for the degree of

Doctor of Philosophy

Trinity 2021

To my family and Cheryl

Acknowledgements

Four years have passed by in a flash. It has truly been a fruitful journey of learning, discovery, and growth, on both a scientific and personal level. I am grateful to my supervisor, Prof Gero Miesenböck, for his advice, inspiration, generosity, and encouragement to think critically and creatively. I have been lucky enough to be given the academic freedom to explore and engage with interesting ideas and projects, the result of which is the work presented here. I would like to thank Lukas Groschner, for his mentorship and immense guidance in patch-clamp experiments; Laura Chan Wah Hak, for patiently teaching me molecular biology; Clifford TaIbot, for his valuable help in designing and assembling the behavioural setup; and Peter Hasenhütl, for his tireless supervision in data analysis. I am also thankful to Alina Krebbers, Anissa Kempf, Celina Hartmann, Eleftheria Vrontou, Giacomo Bertuzzi, Haram Park, Jan Kropf, Katerina Christodoulou, Kay Ellison, Laura Garmendia Sanchez, Lea Ballenberger, Olof Rorsman, Patrick Liu, Raffaele Sarnataro, Susanne Szydlowski, as well as other members of the Centre for Neural Circuits and Behaviour, for their help, and most importantly, for making me feel at home. I thank my examiners Rafal Bogacz and Shamik DasGupta for their time and comments on this thesis. This work was supported by the Hong Kong Jockey Club Graduate Scholarship and the China Oxford Scholarship Fund.

Lastly, my most heartfelt gratitude must be extended to my family, for their unwavering support throughout my life, and to Cheryl, for being an angel.

Abstract

A mobile organism is faced with the challenge of having to decide, moment by moment, its next course of action. Despite extensive efforts in mapping decision-making circuits across many species, the current understanding of neural mechanisms underlying the decision process remains scarce. Fruit flies can perform an odour discrimination task with difficulty-dependent reaction times and choice accuracies, in a framework well-described by a process of evidence accumulation to bound. A subset of third-order olfactory neurons, the $\alpha\beta$ core Kenyon cells ($\alpha\beta_c$ KCs), appears to act as a temporal integrator of sensory information, encoding the amount of summed evidence in their subthreshold voltage. However, explicit demonstration of a causal role of these neurons is lacking.

Combining molecular cloning, patch-clamp electrophysiology, closed-loop optogenetics, and drift-diffusion modelling, I establish a causal relationship between the neural activity in $\alpha\beta_c$ KCs and the fly's olfactory decision-making. First, I discover that a short motif from AMPA receptors can target the optogenetic activator to the somatodendritic compartment of the cell, enabling the optical injection of small dendritic currents. I also modify the genetic construct of the optogenetic inhibitor such that its expression is restricted to the decision-relevant neurons. Second, the functionality of these tools is characterised by whole-cell recordings of $\alpha\beta_c$ KCs. Third, I bidirectionally manipulate the activity of these neurons during the perceptual task to test for behavioural consequences in speed and accuracy. I find that photostimulation quickens reaction times as a function of odour contrast and light intensity. This is mainly explained by a reduction of the bound height in drift-diffusion models, consistent with the representation of the integrated amount, rather than the momentary level, of evidence in $\alpha\beta_c$ KCs. This work sheds light on the mechanisms by which decision-making is implemented in a biological substrate.

Contents

List of Figures **vi**

List of Abbreviations **vii**

1 Introduction **1**
1.1 Neural mechanisms of decision-making 1
1.2 Drift-diffusion models 10
1.3 Olfactory circuitry of the fruit fly 13
1.4 Synaptic integration of sensory information 20
1.5 Aims 24

2 Methods **25**
2.1 Fly strains and culture 25
2.2 Plasmid construction 26
2.3 Odour-guided decision-making task 29
2.4 Behavioural analysis 32
2.5 Drift-diffusion models 33
2.6 Bayesian modelling 37
2.7 Extrema detection 38
2.8 Structural imaging 39
2.9 Fluorescence quantification 40
2.10 Electrophysiology 40
2.11 Statistics 42

3 Results **43**
3.1 Construction of optogenetic tools 43
3.2 Functional testing of optogenetic tools 48
3.3 Optogenetic activation of $\alpha\beta_c$ KCs during behaviour 54
3.4 Optogenetic silencing $\alpha\beta_c$ KCs during behaviour 83

4 Discussion **88**
4.1 Compartmentalised expression of optogenetic tools 88
4.2 Functionality of optogenetic tools 92
4.3 Causal contribution of $\alpha\beta_c$ KC activity 95

Appendix: List of Primers **103**

References **105**

List of Figures

1 Drift-diffusion model of decision-making 11
2 The olfactory system of the fruit fly 15
3 A model of olfactory decision-making in the fruit fly 22
4 Expression patterns of KC GAL4 lines 26
5 Appending dendritically targeting motifs to *Chrimson::tdTom* . . . 27
6 Behavioural setup of the olfactory decision-making task 30
7 Evidence accumulation to bound versus extrema detection 39
8 Dendritic targeting of *Chrimson::tdTom* by the AMPAR motif . . . 45
9 Restricted expression of *Gt*ACR1 in $\alpha\beta_c$ KCs 48
10 Optogenetic activation of $\alpha\beta_c$ KCs using Chrimson 50
11 Optogenetic silencing of $\alpha\beta_c$ KCs using *Gt*ACR1 52
12 Chronometric and psychometric functions 56
13 Reaction time and choice accuracy data from experimental groups . 59
14 Reaction time and choice accuracy data from control groups 62
15 Reaction and transit time distributions from experimental groups . 64
16 Analysis of transit times across task difficulties 66
17 Reaction and transit time distributions from control groups 67
18 5-fold cross-validation of Models 1 and 2 69
19 Two additional approaches of model comparison 71
20 The effects of changing A and k 72
21 Bayesian modelling of reaction time and choice accuracy 76
22 Extrema detection modelling of reaction time and choice accuracy . 79
23 Comparison of drift-diffusion and extrema detection model fits . . . 81
24 Influence of experimental duration on reaction time (I) 82
25 Behavioural data from flies expressing *Gt*ACR1 85
26 Influence of experimental duration on reaction time (II) 87
27 Two distinct mechanisms explaining changes to the DV 97

List of Abbreviations

$\alpha\beta_c$ KC . . . . $\alpha\beta_c$ Kenyon cell

$\alpha'\beta'$ KC . . . . $\alpha'\beta'$ Kenyon cell

aa . . . . . Amino acid

AIC . . . . . Akaike information criterion

AL . . . . . Antennal lobe

AMPAR . . . α-amino-3-hydroxy-5-methyl-4-isoxazolepropionic acid receptor

ANOVA . . . . Analysis of variance

APL . . . . . Anterior paired lateral neuron

ASAP3 . . . . ArfGAP with SH3 Domain, Ankyrin Repeat and PH Domain 3

BIC . . . . . Bayesian information criterion

cAMP . . . . . cyclic adenosine monophosphate

Ch2/3 . . . . . Chromosome 2/3

ChR2 . . . . . Channelrhodopsin-2

DAN . . . . . Dopaminergic neuron

DNA . . . . . Deoxyribonucleic acid

dPAG . . . . . dorsal periaqueductal grey

DV . . . . . Decision variable

EGTA . . . . . Ethylene glycol-bis(2-aminoethylether)-N,N,N',N'-tetraacetic acid

EPSC . . . . . Excitatory post-synaptic current

EPSP . . . . . Excitatory post-synaptic potential

EYFP . . . . . Enhanced yellow fluorescent protein

FEF . . . . . Frontal eye fields

FLP . . . . . Flippase

FOF . . . . . Frontal orienting fields

FoxP . . . . . Forkhead box P

FRT . . . . . Flippase recognition target

GABA . . . . . γ-aminobutyric acid

GFP . . . . . Green fluorescent protein

***Gt*ACR1/2** . . *Guillardia theta* anion channelrhodopsin-1/2

GTP . . . . . Guanosine-5'-triphosphate

HA . . . . . Haemagglutinin

HDDM . . . . Hierarchical drift-diffusion model

HEPES . . . . 4-(2-hydroxyethyl)-1-piperazineethanesulfonic acid

IC . . . . . Intracellular

IR . . . . . Infrared

KC . . . . . Kenyon cell

$\mathbf{K_v}$ . . . . . Voltage-gated potassium channel

LED . . . . . Light-emitting diode

LH . . . . . Lateral horn

LIP . . . . . Lateral intraparietal

LL . . . . . Di-leucine motif

LN . . . . . Local neuron

LR . . . . . Likelihood ratio

MB . . . . . Mushroom body

MBON . . . . Mushroom body output neuron

MCH 4-methylcyclohexanol

MCMC . . . . Markov chain Monte Carlo

MLPH . . . . . Melanophilin

MT . . . . . Middle temporal

nAChR . . . . Nicotinic acetylcholine receptor

NLG1 . . . . . Neuroligin-1

ORN . . . . . Olfactory receptor neuron

PAM . . . . . Protocerebral anterior medial

PBS . . . . . Phosphate-buffered saline

PCR . . . . . Polymerase chain reaction

PN . . . . . Projection neuron

PPC . . . . . Posterior parietal cortex

PPL1 . . . . . Paired posterior lateral 1

ppm . . . . . Parts per million

ROI . . . . . Region of interest

S1 . . . . . Primary somatosensory cortex

S2 . . . . . Secondary somatosensory cortex

SA . . . . . Sequential analysis

SC . . . . . Superior colliculus

SDT . . . . . Signal detection theory

s.e.m. . . . . . Standard error of the mean

Shal . . . . . Shaker cognate 1

SIDL . . . . . Shal interactor of di-leucine motif

SNR . . . . . Signal-to-noise ratio

SS . . . . . Sum of squares

SV40 . . . . . Simian virus 40

tdTom . . . . . Tandem dimer Tomato

TES . . . . . N-[Tris(hydroxymethyl)methyl]-2-aminoethanesulfonic acid

TLCN . . . . . Telencephalin

UAS . . . . . Upstream activating sequence

VDRC . . . . . Vienna *Drosophila* Resource Centre

Choices are the hinges of destiny.

— Pythagoras

1 Introduction

This thesis details the experimental work and data analysis conducted over the course of a four-year doctorate, motivated by a curiosity for how neural circuits precipitate behaviour. This chapter introduces the broad field of perceptual decision-making, and outlines the scientific questions from which the project stems. A description of the tools and techniques required for the work comprises the Methods section, followed by three main parts in the Results chapter. The thesis ends with a discussion on these findings, and how they may contribute to our understanding of the neural mechanisms by which a simple organism, such as the fruit fly, decides.

1.1 Neural mechanisms of decision-making

The price of motility is having to decide what to do next. The decision-maker commits to a choice or course of action based on sensory information and prior knowledge, which assigns value to possible outcomes. Crucially, the involvement of planning and deliberation entails that decision-making operates free from the immediacy of evidence acquisition — a hallmark of cognition (Shadlen and Kiani, 2013). Perhaps what makes the neurobiology of decision-making so attractive is its

tractability to experimental neuroscience, which promises to expose deep insights into the underlying mechanisms and principles governing cognitive processes.

In many sensorimotor tasks, decision-making represents a form of statistical inference (Kersten et al., 2004). The brain attempts to interpret the state of the world, given noisy information transduced by sensory systems. Competing hypotheses h_1 ... h_n (often $n = 2$) that describe the state of the world, for example, whether a stimulus is present or absent, are selected by these decisions. In order for the brain to make the optimal decision, it must rely on priors, evidence, and the value it attributes to the outcomes. The prior $P(h_i)$ refers to the probability that h_i is true before any evidence about the hypothesis is gathered. An apt analogy compares priors to the innate prejudices of jurors that may bias their collective verdict in the courtroom. In sensorimotor decisions, priors often correspond to the predicted probability of observing a particular stimulus in the trial, which can be instructed (Platt and Glimcher, 1999) or inferred from past trials (Sugrue et al., 2004). On the other hand, the evidence (e) resembles information that favours a certain hypothesis, just as fingerprints at the crime scene may attaint a particular suspect. It is useful to interpret evidence e in the context of conditional probabilities such as $P(e|h_i)$, which prescribes the likelihood of observing e if h_i is true. Value (v) is the subjective assessment of each of the potential outcomes by consideration of their costs and benefits. The obvious way to manipulate v in a perceptual task is to present reward or punishment to the subject, such that the choices gain valence. Overall, the brain appears to translate the accrual of all sources of priors, evidence, and value into a conceptual quantity called the decision variable (DV), onto which a decision rule can apply to produce a choice. The remainder of this section will attempt to refine the concept of the DV, and evaluate the progress in the search for its neural correlates.

Signal detection theory and sequential analysis

Signal detection theory (SDT) remains one of the most successful formalisms in psychophysics, or the study of perception. In this framework, the decision maker observes a piece of evidence e caused by an experimenter-controlled stimulus h_1 or h_2. In the brain, e may be represented by the spike count from a neuron or pool of neurons, or derived, e.g., the difference in spike rates for the two populations (Newsome et al., 1989). Since e is also corrupted by noise, mainly during sensory transduction, it can be viewed as a random variable whose distribution is structured by parameters (e.g., the mean) set by h_1 or h_2. The decision then becomes a comparison of these likelihoods $P(e|h_1)$ and $P(e|h_2)$, i.e., deciding which states give rise to observation e. For binary decisions, the DV is constructed by the likelihood ratio (LR): $\mathrm{LR}(e) = \frac{P(e|h_1)}{P(e|h_2)}$. The simplest decision rule applies a criterion to the DV; for instance, choose h_1 if $\mathrm{LR}(e) \geq \alpha$, where α is a constant. The advantage of SDT is that it provides flexibility to incorporate priors, evidence, and value to reach a variety of goals; different forms of decisions can be achieved by simply using different values for the criterion.

However, SDT does not construe the amount of time taken to complete the decision, which is a crucial feature of decision-making. Indeed, since the information required to commit to a choice is seldom available all at once, the brain often needs to gather multiple pieces of evidence sequentially. This occurs over timescales longer than the natural integration times of sensory receptors. Another advantage of constructing time-averaged sensory representations is to reduce the effects of noise, improving the signal-to-noise ratio (SNR) and thus the confidence about the underlying state h_i. As such, the DV needs to be updated in time. Additionally, the termination of the decision can depend on either the level of certainty (relating to the SNR), or elapsed time, as in a deadline. Sequential analysis (SA), a natural extension of SDT, accommodates multiple pieces of evidence and implements a stopping rule.

A DV that accumulates many independent samples of evidence, $e_1, e_2, \ ... \ , e_n$, is simply the sum of the logarithms of the LR corresponding to each piece of evidence:

$$\log(\text{LR}) = \log \frac{P(e_1, e_2 \ ... \ e_n|h_1)}{P(e_1, e_2 \ ... \ e_n|h_2)}$$
$$\sum_{i=1}^{n} = \log \frac{P(e_i|h_1)}{P(e_i|h_2)}$$

The stopping rule prescribes an updating of the DV until a threshold is reached. Taken together, this framework elegantly characterises decision-making as a process of evidence accumulation to bound. It represents a parsimonious description of the necessity to temporally integrate noisy sensory information, as well as the intuitive relationship between reaction time and stimulus strength. Easy decisions are fast as they are informed by clear-cut sensory evidence; difficult decisions that depend on more ambiguous information tend to be slower, as the DV takes longer to reach the bound. In the brain, this process can also be realised as a race between two integrators, one that accumulates evidence in favour of h_1, the other, of h_2 (Bogacz et al., 2006; Vickers, 1970). In many models that incorporate SA, evolution of the DV closely mirrors the mathematical description of a random walk or diffusion process (Ratcliff and Smith, 2004), giving rise to a virtual trajectory akin to the movements of a particle in Brownian motion. A more detailed explanation of such drift-diffusion models will be discussed in the next section. Overall, SA in decision theory is instructive to our understanding of how the decision process formulates. First, it provides a means to differentiate between evidence and the DV, since the former is momentary, whereas the latter evolves in time. In principle, changes to either can influence choice accuracy and reaction time, but in different ways that can be distinguished electrophysiologically (Hanks et al., 2006). Second, it specifies a termination rule, a decision bound that signals the commitment of choice. In many cases, it is unclear how this bound is implemented in a neural substrate, although most accounts have focused almost exclusively on a criterion based on some maximum level of suprathreshold neural activity quantified by spike rates (Mountcastle et al., 1990; Newsome et al., 1989).

Indeed, it remains an important goal in modern neuroscience: to search for and characterise neural correlates of the DV.

Neural correlates of the decision variable

Classical two-choice perceptual tasks have proven instrumental in the study of decision-making because they allow the experimenter to carefully manipulate the strength of sensory stimulus while measuring behavioural output simply as a binary choice. A wealth of literature documents the employment of such tasks to probe how elements of the perceptual decision are realised in a neural substrate (Gold and Shadlen, 2007; Hanks and Summerfield, 2017; Shadlen and Kiani, 2013). Early work by Mountcastle and colleagues developed the vibrotactile frequency paradigm in which monkeys are required to choose the tactile stimulus with the higher frequency (Mountcastle et al., 1990). Most neurons in the primary somatosensory cortex (S1) monotonically increases their average firing rate with increasing stimulus frequency, providing a neural representation of evidence. These signals will be compared to generate a DV in downstream areas — regions such as the secondary somatosensory cortex (S2; Romo et al., 2002), the dorsolateral prefrontal cortex (Brody et al., 2003), and the medial and ventral premotor cortices (Hernández et al., 2002; Romo et al., 2004) are thought to house neural activity that more closely resembles a DV. Many neurons in these areas show persistent firing in the period between the two stimulus presentations; during the comparison interval, a portion of them exhibits activity that appears to reflect the difference in frequencies. However, as with many other perceptual tasks, challenges remain to identify clear mechanistic pathways among complex circuits that precipitate the decision process, since it is becoming increasingly apparent that neural activity in many behavioural contexts is multiplexed (Johnston et al., 2020; Kyriazi et al., 2018; Meister et al., 2013; Park et al., 2014; Parthasarathy et al., 2017; Raposo et al., 2014; Rigotti et al., 2013; Zhou et al., 2021).

Another example, and perhaps the most insightful experimental paradigm in the past few decades, is the visual random-dot motion task, first pioneered by Britten, Newsome, Shadlen, and Movshon in the late 80s and early 90s (Britten et al., 1996, 1992; Newsome et al., 1989). In the task, the monkey is presented with an array of moving dots on a screen and is required to indicate with a saccadic movement the direction of coherent dot motion ('signal') under a masking pattern of randomly moving dots ('noise'). Varying the fraction of coherently moving dots (signal-to-noise ratio) titrates task difficulty from easy to near psychophysical threshold. When monkeys perform the task, individual neurons in various brain areas demonstrate spike rate dynamics that correlate with the strength and variability of the noisy stimulus. For instance, in the middle temporal (MT) visual area, the direction of motion can be decoded efficiently by comparing spike counts of direction-selective neurons tuned to either leftward or rightward motion. Such 'neuron' and 'antineuron' pairs (Britten et al., 1992) are thought to provide antagonistic, momentary evidence to downstream integrators in the formation of the monkey's choice. Indeed, microstimulation of a cluster of similarly tuned MT neurons not only biases the monkey's choices towards their preferred direction (Salzman et al., 1990, 1992), but also quickens the monkey's reaction times (Ditterich et al., 2003; Hanks et al., 2006).

Downstream in the flow of visual information are areas expected to exhibit activity that extends the causal chain of decision-making, thus potentially representing the decision variable. One such region is the lateral intraparietal area (LIP), anatomically positioned midway through the sensorimotor chain: on one hand receiving inputs from visual areas such as MT (Andersen et al., 1990; Blatt et al., 1990), and on the other projecting to structures involved in the control of eye movements, such as the frontal eye fields (FEF) and superior colliculus (SC; Fries, 1984). In theory, neural activity that represents the DV should be temporally prolonged, outlasting the immediate responses of visual neurons, and contain aspects of both sensory and motor information. During the epoch before the monkey's overt

commitment to a choice, pools of LIP neurons that extend receptive fields covering either of the saccadic targets exhibit difficulty-dependent, ramp-like increases in average firing rates that mirror the difference between firing rates in oppositely-tuned MT neurons, when the final choice falls on the corresponding saccadic target (Roitman and Shadlen, 2002). If the monkey chooses the alternative, out-of-field target, the same neurons show meandering activity that tends to decline. In addition, brief directional 'motion pulses' lead to persistent effects in LIP spike rates and the monkey's judgment (Huk and Shadlen, 2005). In other words, information about the stimulus strength and the monkey's choice is reflected in the trial-averaged activity of LIP neurons, at timescales (ramp activity ∼200 ms after stimulus onset, until ∼70 ms before saccade initiation) compatible with the integration of evidence from MT neurons as well as nondecision latencies. Aligning these responses across various motion coherences to saccade initiation reveal a stereotyped maximal firing rate of ∼70 sp s^{-1} (Roitman and Shadlen, 2002). Although the significance of this particular level of firing is unclear, it is attractive to speculate this as a biological implementation of the decision bound. Taken together, these experiments provide compelling evidence for the role of LIP as an integrator of sensory evidence — a neural correlate of the DV.

Subsequent experiments have probed the causal role of LIP neurons in decision-making. Electrical microstimulation of LIP clusters results in modest but significant effects on the monkey's choices, while speeding up decisions that select the within-receptive field target, but slowing down those otherwise (Hanks et al., 2006). However, more recent accounts have challenged the resemblance of ramping dynamics in LIP to evidence integration by a DV, since single-trial LIP spike trains appear to be better described by randomly timed, discrete steps between underlying states (Latimer et al., 2015; Zoltowski et al., 2019). The causal involvement of LIP is further called into question as acute pharmacological inactivation of the area exerts no measurable impact on the monkey's psychophysical performance (Katz et al., 2016), although a recent report presents conflicting evidence (Zhou and

Freedman, 2019). In addition, functional dissection of single-trial dynamics in MT and LIP reveals that the integration of MT responses cannot sufficiently explain LIP activity during motion viewing; instead, a premotor signal accounts for a large component of the ramping responses (Yates et al., 2017). The idealisations of MT and LIP in the decision process thus need to be revised to include currently unknown sensorimotor computations intervening on the two areas. Given the constellation of conflicting results, a more updated view in the field suggests that the complex, decision-related activity patterns in LIP likely parallel, rather than constitute, the integration of visual information.

In recent years, many studies of perceptual decision-making have gravitated towards the use of rodent models (Carandini and Churchland, 2013), given the cognitive repertoire that is well-suited for the study of evidence accumulation (Brunton et al., 2013; Hanks et al., 2015; Yartsev et al., 2018). Perceptual tasks implemented across diverse sensory modalities, utilising auditory (Akrami et al., 2018; Brunton et al., 2013), tactile (Guo et al., 2014), or olfactory (Uchida et al., 2006) stimuli, have revealed fascinating insights that implicate distinct brain regions, including the posterior parietal cortex (PPC; Hanks et al., 2015), frontal orienting fields (FOF; Hanks et al., 2015) in the prefrontal cortex, superior colliculus (Duan et al., 2021), and the dorsal striatum (Yartsev et al., 2018), either correlationally or causally, in evidence integration (Brody and Hanks, 2016; Scott et al., 2017), sensory history (Akrami et al., 2018), or behavioural choice (Duan et al., 2021). Increasingly complex task structures that engage a variety of cognitive functions even uncover single neurons in the rat orbitofrontal cortex whose activity co-varies with many distinct decision-related variables (Hirokawa et al., 2019). Meanwhile, advances in multi-electrode recordings (Kiani et al., 2014) and computational methods to analyse population data (Cunningham and Yu, 2014; Kobak et al., 2016) have spurred large-scale studies that examine the geometry of the DV along curved, population-response manifolds (Okazawa et al., 2021), or even decode a model DV

from population activity that is used to perform real-time, neurally contingent perturbations of the animal's decision states (Peixoto et al., 2021).

It is impossible to provide an exhaustive list here of the rich literature that probes neural correlates of the DV and other task-related variables in rodents and primates. However, despite the plethora of experimental paradigms, a general and unified mechanistic understanding of decision-making that relates definitive neural circuits remains inchoate. Perhaps more tractable progress will be achieved using simpler organisms, such as the fruit fly (DasGupta et al., 2014; Groschner et al., 2018).

1.2 Drift-diffusion models

Complementary to the search for biological substrates of decision-making is the development of mathematical models that formalise the cognitive process of decision formation and quantify the relationships between speed, accuracy, and stimulus strength. In particular, drift-diffusion models have been remarkably successful in capturing all psychophysical aspects of perceptual decisions (Bogacz et al., 2006; Gold and Shadlen, 2007). A comprehensive analysis of six distinct formalisms reveals that optimal parameters for five of them can reduce the models to a simple diffusion process (Bogacz et al., 2006), reflecting the centrality of this mechanism in decision-making.

As discussed, the marriage of signal detection theory and sequential analysis to formulate the decision process derives an evolving DV that mimics a one-dimensional random walk or diffusion process (Ratcliff and Smith, 2004). This DV embodies the sequential sampling and integration of noisy sensory evidence until threshold crossing, triggering the decision. Crucially, the samples are independently accumulated and maintained in the form of a short-term memory. In a two-choice scenario, the DV representing the net evidence favouring either one of the options evolves in time with a difficulty-dependent drift plus Gaussian diffusion noise towards the upper of lower decision bound (**Fig.1**). The drift rate quantifies the average rate of evidence accumulation and is monotonically related to the stimulus strength. Solving the first-passage problem for the DV yields analytical expressions that relate reaction time and choice accuracy to task difficulty, drift rate, bound height, and residual time (Bogacz et al., 2006; Palmer et al., 2005; see **Methods**) — nondecision delay that encompasses motor latencies and procrastination. The model is also flexible in incorporating various features of the decision process. When the animal is influenced by priors that favour one alternative over the other, the bias can be conveyed with asymmetric bounds. In addition, there is often a cost of deliberation time — the brain will minimise the cost by adding an evidence-independent 'urgency' signal to

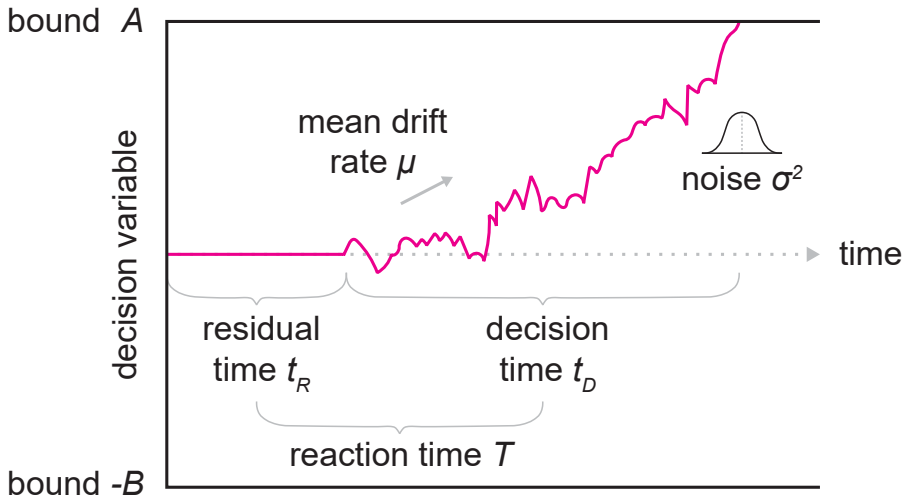


Fig. 1: Drift-diffusion model of decision-making.
Example of a random walk illustrating the accumulation of evidence over time towards a critical amount (bound A or $-B$). A decision variable representing the net evidence in favour of option A or $-B$ evolves as a function of time with difficulty-dependent drift μ and Gaussian diffusion noise (with zero mean and variance σ^2). A choice is triggered when the decision variable reaches the upper or lower bound. Here, the bounds are symmetrical, i.e., $A = B$. The reaction time T consists of the actual decision time t_D and a residual time t_R that includes motor latencies.

the accumulated information (Cisek et al., 2009). In this case, the bounds decline as a function of elapsed decision time (Drugowitsch et al., 2012).

The beauty of this model lies in its conceptual simplicity while preserving the empirically observed tradeoff between choice accuracy and reaction time: lowering the bound height reduces both parameters, as the threshold is reached sooner, but the effects of noise on the choice become more significant. The framework is so powerful that in the random-dot motion task, one can fit the model to the monkey's reaction times and use the estimated parameters to predict the accuracy at each difficulty level (Roitman and Shadlen, 2002). It also accounts for the subjects' skewed reaction time distributions, an important property of the model (Ratcliff et al., 2015). In fact, drift-diffusion models have provided excellent fits to psychometric and chronometric data from species across phyla: from monkeys (Hanks et al., 2006; Palmer et al., 2005) and rodents (Evans et al., 2018; Hanks et al., 2015; Yartsev et al.,

2018) to even fruit flies (DasGupta et al., 2014; Groschner et al., 2018), testament perhaps to the stereotypy of mechanisms involving evidence accumulation to bound.

In studies that probe causality, these models have been used to evaluate how experimental manipulations of neural activity influence the decision process. Microstimulation of MT or LIP when the monkey is performing a motion discrimination task produces changes in choice behaviour and reaction time, albeit to a different degree (Ditterich et al., 2003; Hanks et al., 2006). Model fits to the data distinguish the qualitative differences in these effects and place the two areas in distinct positions along the causal chain: MT stimulation is consistent with an increase in drift rate, linking those neurons to a representation of momentary evidence; whereas LIP stimulation induces a reduction in bound height, equivalent to an offset in the DV (Hanks et al., 2006). More recently, monkeys trained to report the orientation of a dynamic Glass pattern suffer a drop in performance after unilateral, reversible, inactivation of SC (Jun et al., 2021). Hierarchical and nonhierachical variants of the model fit to behavioural data reveal that these changes are congruent with an evidence-independent offset in the drift rate (momentary evidence), biasing the decisions. In this thesis, the drift-diffusion model has been particularly useful in the analysis of reaction time and choice accuracy data from flies performing a perceptual task.

1.3 Olfactory circuitry of the fruit fly

In contrast to the complex architectures in visual and auditory circuits, especially in the mammalian cortex, the olfactory system bears a shallow organisational structure which is favourable to the study of circuit dynamics during behaviour (Mori and Sakano, 2021). In particular, that of the fruit fly has been well-characterised by connectomics (Aso et al., 2014a; Li et al., 2020), functional and behavioural experiments (Aso et al., 2014b; Owald and Waddell, 2015), as well as computational modelling (Amin et al., 2020; Endo et al., 2020; Kadakia and Emonet, 2019). Amongst the extensive *Drosophila* research in mapping neural circuits to a broad behaviour repertoire, including sleep (e.g., Kempf et al., 2019; Pimentel et al., 2016), navigation (e.g., Currier and Nagel, 2020; Turner-Evans et al., 2020), learning and memory (e.g., Felsenberg et al., 2018; Jacob and Waddell, 2020; Owald et al., 2015), courtship (e.g., Nojima et al., 2021; Pavlou and Goodwin, 2013), and social attraction (Sun et al., 2020), the study of olfactory decision-making is beginning to gain traction (DasGupta et al., 2014; Groschner et al., 2018). In an odour discrimination task, fruit flies, like mammals, take longer to commit to difficult choices than to easy ones (DasGupta et al., 2014). The same quantitative relationships formalised by drift-diffusion models can be applied to link reaction time, accuracy, and odour contrast (task difficulty), pointing to the presence of a decision-making circuit that integrates olfactory information (Groschner et al., 2018).

The goal of any sensory system is to transduce distinct stimuli into neural representations — in the form of bioelectric signals — that are far enough apart for the organism to act accordingly (Groschner and Miesenböck, 2019). The fly olfactory system (**Fig.2**) achieves this feat by utilising a three-layer information processing motif (or 'Marr motif'; Marr, 1969) that features a combinatorial code of the stimulus encoded by the first stage (the 'encoder'), relayed with a massive expansion of neuron number to the second stage ('the decoder'), and finally a third stage that selects ethologically important information on which to impinge

valence (Stevens, 2015). This organisational motif originates from a description of the vertebrate cerebellar architecture (Marr, 1969). Indeed, the fly olfactory system shares this structure not only with the cerebellum, but also its vertebrate counterparts, as well as the hippocampus (Farris, 2011; Lin et al., 2014; Litwin-Kumar et al., 2017; Stevens, 2015).

Olfactory discrimination commences with the interaction of airborne odorants with ∼50 olfactory receptors (Clyne et al., 1999; Gao and Chess, 1999; Vosshall et al., 1999), expressed on the dendrites of ∼50 types of olfactory receptor neurons (ORNs) (**Fig.2**, yellow). These cells are located within the olfactory epithelium in the mammalian nasal cavity, or inside chemosensory protrusions (sensilla) on the fly antennae and maxillary palps (Hildebrand and Shepherd, 1997). Such anatomical differences entail that odour plume sampling is paced by the respiration cycle in mammals (Uchida and Mainen, 2003), whereas insect olfaction is liberated from these temporal constraints. Olfactory receptors are exclusively G protein-coupled in mammals (Brunet et al., 1996), but those in insects are diverse and mostly ionotropic (Sato et al., 2008; Wicher et al., 2008), enabling fast signal transduction without the need for second messengers (Szyszka et al., 2014). While many olfactory receptors are promiscuous in their binding of odorant molecules with varying concentration-dependent affinities (Hallem and Carlson, 2006), some are selective solely for a pheromone (Kurtovic et al., 2007). Each ORN typically expresses only a single functional receptor, which designates the neuron's receptive field (Hallem et al., 2004). Despite the scattered arrangement of ORNs with the same receptor profile, their bilateral axons converge with striking precision onto one of the ∼50 glomeruli in the antennal lobes (AL), where they form synapses with subsets of excitatory projection neurons (PNs; ∼160 per lobe) (**Fig.2**, grey) and inhibitory (mostly) local neurons (LNs; 100 per lobe) (**Fig.2**, green) (Gao et al., 2000; Vosshall et al., 2000). All PNs innervating the same glomerulus receive ORN input from a population that is at least tenfold larger; since neurons in this population bear identical response spectra but spike independently of one another, pooling their responses improves

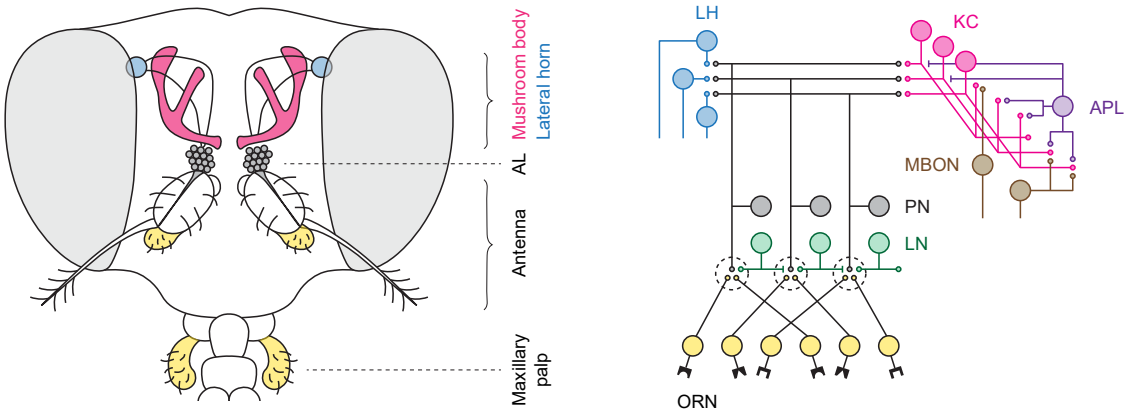


Fig. 2: The olfactory system of the fruit fly.
Simplified schematic of the fly olfactory system at macroscopic (left) and cellular (right) resolution. The system employs a three-layer information processing motif that features an 'encoder', a 'decoder', and a 'valence-matching' stage. More explanation in text. Olfactory information is transduced by olfactory receptor neurons (ORNs, yellow), located in the antennae and maxillary palps. Those expressing the same receptor gene extend converging axons into a confined glomerulus (dashed circle) in the antennal lobe (AL), where local neurons (LNs, green) also provide lateral excitation and inhibition. Projection neurons (PNs, grey) arborise in the glomeruli and project to the lateral horns (LH, blue) and the mushroom bodies (MB), where random connectivity between PNs and Kenyon cells (KCs, pink) increases the computational capacity for odour representations. KCs from each hemisphere receive global inhibition from a giant inhibitory interneuron (APL, purple). Around 2000 KCs converge onto only 34 mushroom body output neurons (MBONs, brown), the efferent arm of the MB. Dopaminergic neurons are not shown. For clarity, the circuitry, synaptic connections, and proportions of neuron number are greatly simplified. Adapted from Lukas Groschner and Groschner and Miesenböck (2019).

the signal-to-noise ratio and allows PNs to detect slight changes in firing rate amidst a noisy background of spontaneous ORN activity (Jeanne and Wilson, 2015).

The encoder of odour representations lies in this array of glomeruli in the AL, analogous to the vertebrate olfactory bulb. In a simplistic view, odours are represented by a glomerular code of ∼50 active or inactive channels, contingent on their chemical identity and concentration (Groschner and Miesenböck, 2019). Realistically, the combinatorial code also takes into account the level of activity within each channel. In a hypothetical olfactory system with only a single glomerular channel that responds strongly to odour A and more weakly to B, discrimination of the odour pair will require an inspection of their respective likelihood functions,

$P(R|A)$ and $P(R|B)$. The less overlap between these response distributions, the easier it is for the brain to circumscribe a threshold between the means and achieve accurate discrimination. However, in this example, it would be implausible for the system to know the full likelihood functions $P(R|A)$ and $P(R|B)$ in order to decide between A and B from a single observation R. In principle, by introducing a second population of neurons that manifest opposite odour responses (i.e., more strongly to B than A), or 'antineurons' (Britten et al., 1992), the activity difference in the two channels can be taken as the log likelihood ratio (Gold and Shadlen, 2007). In biological reality, the fly compares the activity within differently tuned glomerular channels. Separated in developmental complexity and evolutionary time, ∼1500 glomeruli in mice correspond to only one-thirtieth of that number in flies (Hildebrand and Shepherd, 1997), but the ∼50-dimensional coding space is already sufficient for a fly to discriminate between very similar odours (Parnas et al., 2013). In addition, several features of this processing stage serve to regulate the gain and offset of the encoder. First, odour-evoked activity desensitises the ORN through Ca^{2+}-mediated negative feedback (Störtkuhl et al., 1999) such that strong excitation (e.g., when odour concentration rises) attenuates subsequent responses. Receptor adaptation allows ORNs to represent a stimulus spectrum exceeding their dynamic range (Gorur-Shandilya et al., 2017), and accentuates changes in odour concentration (Nagel and Wilson, 2011). Second, the compressive non-linearity of ORN-PN connections amplifies weak ORN inputs, as discussed. Third, across the entire AL, ipsilaterally and bilaterally projecting LNs mediate lateral inhibition that scales with total ORN activity, further decorrelating the PN channels to facilitate odour discrimination (Olsen et al., 2007, 2010).

The combinatorial odour representations are relayed by bifurcating PN axons to the third-order olfactory neurons in two discrete decoders: the lateral horns (LH) of the protocerebrum, and the mushroom bodies (MB). The LH (**Fig.2**, blue) receive stereotypic patterns of input from PNs (Fişek and Wilson, 2014) and appear to drive innate odour-guided behaviours (Parnas et al., 2013), whereas the MB are

instrumental in associative learning and memory (Heisenberg et al., 1985; Keene and Waddell, 2007). Here, stereotyped anatomy dissolves into seemingly random wiring, as PNs are connected to Kenyon cells (KCs) (**Fig.2**, pink), the mushroom body intrinsic neurons homologous to vertebrate piriform cortex pyramidal neurons and cerebellar granule cells (Stevens, 2015), without precise specificity (Caron et al., 2013; Murthy et al., 2008). Approximately 2000 KCs per hemisphere arborise in the mushroom body calyx, elaborate 2–11 dendritic claws clasping presynaptic boutons of cholinergic PNs (Caron et al., 2013; Gruntman and Turner, 2013), and further receive global inhibition from one giant GABAergic anterior paired lateral neuron (APL) (**Fig.2**, purple) (Lin et al., 2014). The expansion ratio from PNs to KCs matches that from cerebellar mossy fibres to granule cells (Litwin-Kumar et al., 2017), exemplifying the theoretical prediction that projecting activity onto large lattices of neurons promotes stimulus separation (Marr, 1969). Spatiotemporally sparse coding in KC ensembles contrasts with the dense odour representations in the AL: any given odour only elicits a few spikes in 5–10% of KCs (Ito et al., 2008; Turner et al., 2008). This sparseness originates in part from APL-mediated feedback inhibition onto all KCs (Lin et al., 2014) and serves to decorrelate odour representations, thus expanding the capacity of associative memory (Kanerva, 1988; Treves and Rolls, 1991). KCs can be subdivided into seven genetically and biophysically distinct classes (Aso et al., 2014a; Tanaka et al., 2008). Whereas γ_{d} and γ_{main} KCs extend axons into a single horizontal lobe, projections of $\alpha\beta$ and $\alpha'\beta'$ KCs bifurcate to form vertical (α, α') and horizontal (β, β') ones. Based on morphology and clonal origin, $\alpha\beta$ KCs can be further partitioned into core ($\alpha\beta_c$), surface ($\alpha\beta_s$), posterior ($\alpha\beta_p$), and $\alpha'\beta'$ into middle ($\alpha'\beta'_m$), and anterior-posterior ($\alpha'\beta'_{ap}$) layers. KCs project to the MB lobes, which are compartmentalised by the dendritic arbors of mushroom body output neurons (MBONs) (**Fig.2**, brown) (Aso et al., 2014a). Although synaptic boutons along KC axons are non-uniformly activated by odours, those within the same compartment share a more coherent tuning, forming a functional unit (Bilz et al., 2020). Overall, in this decoder stage, odour information has transformed into a distributed representation in the MB,

where inspection of the activity in a small KC subset would suffice to retrieve all the information encoded in the glomerular channels (Stevens, 2015). This is contrary to a localised representation, for instance, in the mammalian primary visual cortex, where a specific group of neurons only confers information about a tiny patch of the visual world. Volumetric Ca^{2+} imaging of most of the PN and KC populations reveals the emergence of clustered representations for groups and mixtures of odours in the MB; this transformation from the first to second stage of information processing vastly enhances odour discrimination and generalisation (Endo et al., 2020).

For the fly, what is important after all is learning the ethological significance of different odours: in essence, whether the odour is attractive or aversive. This valence is assigned and stored as memory in the third stage of information processing, at the synapses between KCs and MBONs (Aso et al., 2014b; Claridge-Chang et al., 2009; Cohn et al., 2015; Hige et al., 2015; Owald et al., 2015; Séjourné et al., 2011). Remarkably, ∼2000 KCs converge onto only 34 MBONs of 21 types (Aso et al., 2014a), the only known efferent pathways of the MB, bridging the structure with downstream locomotor regions in the central complex (Strauss, 2002). MBONs also form connections within individual MB compartments, providing lateral inhibition and recurrent excitation (Aso et al., 2014b). Crucially, ∼130 dopaminergic neurons (DANs) that convey contextual signals also innervate the MB, forming tripartite synapses with KC axons and dendritic arborisations of MBONs. When odour exposure coincides with punishment, such as an electric shock, a subset of aversively reinforcing DANs from the paired posterior lateral 1 (PPL1) cluster innervating the vertical α lobes is co-activated with the sparse, odour-specific KC ensemble, depressing the KC-MBON synapses via a cAMP-dependent plasticity (Handler et al., 2019; Tomchik and Davis, 2009). Subsequently, when the odour is experienced again, MBONs that extend dendrites to the β lobe will receive stronger input than their α lobe counterparts, tilting the behavioural output towards avoidance. Conversely, appetitive conditioning causes DANs from the protocerebral anterior medial (PAM) cluster to provide reward-specific teaching signals that depress

the output from the β lobes, triggering approach (Aso et al., 2014b; Hige et al., 2015). In general, dopaminergic signalling can tune the transmission between an individual KC and its repertoire of postsynaptic MBON partners based on the state of the animal; consequently, the same KC odour representation can evoke different patterns of activity, facilitating flexible and adaptive behaviour (Cohn et al., 2015). Transitioning from the first (glomeruli), through the second (KCs), to the third (MB lobes) stages of processing, odour representations are converted from a high-dimensional sensory code into a low-dimensional behaviour-instructing output, stored in a sparse, distributed memory.

Fruit flies can distinguish between pairs of distinct odours (Quinn et al., 1974), overlapping odour mixtures (Campbell et al., 2013), or two different concentrations of the same odour (DasGupta et al., 2014; Heisenberg et al., 1985), exhibiting psychometric functions comparable to those in primates (DasGupta et al., 2014; Palmer et al., 2005). This suggests the presence of a temporal integrator of sensory information within their three-stage olfactory architecture, indispensable for odour-guided decision-making.

1.4 Synaptic integration of sensory information

Insights into the identity of the putative integrator came from a behavioural screen that implicates the population of $\alpha\beta_c$ KCs (∼400 out of ∼2000 KCs per hemisphere) (Tanaka et al., 2008) in the process of evidence accumulation (DasGupta et al., 2014). These neurons are distinguished by the expression of the forkhead box P transcription factor (FoxP) (DasGupta et al., 2014; Groschner et al., 2018), an ancestral member of a family of transcription factors studied in developmental neurobiology (Konopka et al., 2009), cognitive science (Hamdan et al., 2010), and linguistics (Lai et al., 2001). Vertebrate orthologues, including human *FOXP1* and *FOXP2*, have generated considerable interest owing to their proposed involvement in vocal communication (Haesler et al., 2007; Hamdan et al., 2010; Lai et al., 2001) and motor learning (Groszer et al., 2008).

FoxP mutants require more time to discriminate between odour intensities, especially at high difficulty levels, but their choice accuracies remain comparable with those of wildtype flies (DasGupta et al., 2014). This selective defect in reaction time implies an impairment of the temporal integration process in decision-making. It remains one of the few, if not the only, examples where the speed of the animal's behaviour is manipulated independently of its accuracy. Patch-clamp recordings of the sparsely firing $\alpha\beta_c$ KCs, the neurons to which FoxP localises, reveals that a voltage gap of 8.2 mV — much wider than that of other KCs, such as $\alpha'\beta'$ — separates the resting membrane potential and spike threshold, in effect rendering spontaneous activity infrequent (Groschner et al., 2018). In theory, six or seven perfectly coincident PN inputs can bridge this voltage gap; in reality, since PNs do not fire in complete synchrony, excitatory post-synaptic potentials (EPSPs) need to be integrated over time. With high input resistances and long time constants, the thin, elongated dendrites of $\alpha\beta_c$ KCs act as temporal filters that mitigate the decay of EPSPs, contributing to the persistence of an accumulator memory. Paradoxically, this memory is hindered by leak currents conducted by

the dendritically restricted voltage-gated A-type potassium channel Shal (K_v4) (Diao et al., 2010; Wei et al., 1990), since they dampen synaptically evoked voltage changes (Cai et al., 2004). Consequently, a larger number of EPSPs is required to fire an action potential, by a factor contingent on the strength of the sensory evidence: sizable changes in odour concentration cause steep depolarisations to spike threshold, whereas low-contrast stimuli only induce shallow, meandering deflections of the membrane potential, resulting in long spike latencies (Groschner et al., 2018). Given that FoxP expressed in $\alpha\beta_c$ KCs represses the Shal promoter (Groschner et al., 2018), wildtype levels of Shal are already restricted to within narrow limits. Indeed, in FoxP-deficient mutants, the abundant expression of Shal exacerbates the influence of leak currents, severely compromising the responses to odour concentration changes: rapid decay of EPSPs, prolonged spike delays, and response failures are frequently observed, pointing towards the curtailed ability of $\alpha\beta_c$ KCs to sum synaptic inputs. Analysis of these neurometric functions for both wildtype and mutant flies reveal a striking parallel between the mean latencies of the first $\alpha\beta_c$ KC spikes and the pure decision times from empirical data, for both genotypes and across all odour contrasts. Similarly, the psychometric function can be well-predicted by tallying the percentages of first spikes emitted after odour concentration steps. These experiments suggest that during olfactory decision-making, sequential analysis is implemented in the form of subthreshold synaptic integration in $\alpha\beta_c$ KCs, with the discharge of an action potential as the stopping rule (**Fig.3**, right) (Groschner and Miesenböck, 2019).

The notion that $\alpha\beta_c$ KC activity — to a large extent sculpted by the neurons' biophysical properties — dictates the speed at which the flies perform odour-guided decisions is further strengthened by two pieces of experimental evidence. First, the diffusion noise estimated from the model fit to psychophysical measurements of speed and accuracy matches the electrophysiological measurements of membrane potential noise in $\alpha\beta_c$ KCs (Groschner et al., 2018). Second, the reaction time

defect sustained by *FoxP* mutants can be rescued by the overexpression of dominant-negative Shal; conversely, it can be introduced to wildtype flies by overexpressing functional Shal (Groschner et al., 2018). In other words, manipulation of a single ionic conductance in a decision-relevant subset of neurons suffices to precipitate corrective or debilitating behavioural consequences. In addition, neural recordings of $\alpha\beta_c$ KC activity have in fact uncovered two functional classes, termed 'up' and 'down' cells, responding to odour onset or offset, respectively. These two mutually inhibiting (presumably via APL) populations can be envisioned as a pair of competing accumulators that assume the roles of neurons and antinuerons (**Fig.3**, left) (Britten et al., 1992; Groschner et al., 2018; Vrontou et al., 2021). Taken together, $\alpha\beta_c$ KCs appear to encode a quantity closely related to a DV: their subthreshold voltage tracks the amount of integrated evidence for or against a choice (**Fig.3**, right). At odour onset, the activity of 'up' cells ramps up towards spike threshold, while that of 'down' cells stays hyperpolarised; and vice versa, at odour offset. However, there is currently no direct demonstration of a causal

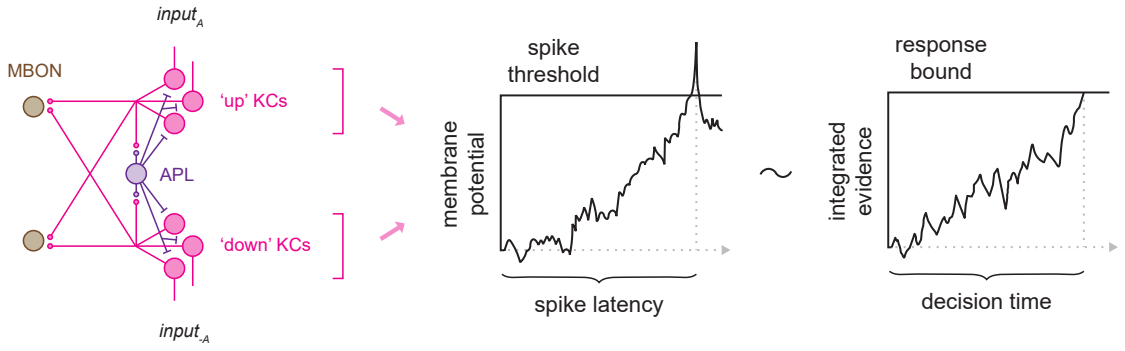


Fig. 3: A model of olfactory decision-making in the fruit fly.
Left: in this model, two antagonistic pools of $\alpha\beta_c$ KCs (pink), termed 'up' and 'down' cells, integrate information on increases and decreases in odour concentration ($input_A$ and $input_{-A}$), acting as competitive accumulators in a race architecture to direct choices towards A or $-A$, respectively. Lateral inhibition is likely mediated by APL (purple). The next processing layer is at the level of MBONs (brown). Synaptic connections and circuit architecture are grossly simplified. Right: experimental evidence (see text) suggests that the membrane potential dynamics of these cells resemble the evolution of a decision variable, with the spike threshold as a natural cutoff to trigger decision commitment. Adapted partly from Groschner et al. (2018).

connection between KC activity and the fly's behaviour. This will require real-time, stable recordings of neural activity during the lead-up to a choice, encompassing both the training and testing epochs. Alternatively, causal manipulations of $\alpha\beta_c$ KC responses, such as optogenetic activation or silencing (Miesenböck, 2009), will corroborate the integral role of these neurons in olfactory decision-making.

Most accounts of mapping the DV onto a neural substrate have focused on suprathreshold, spike-based mechanisms, such as smooth, ramping increases in mean firing rates (Roitman and Shadlen, 2002), discrete steps from low to high activity (Latimer et al., 2015), or evolving activity toward choice-specific attractors (Harvey et al., 2012; Okazawa et al., 2021). In contrast, evidence integration that relies on subliminal voltage changes is far less studied, but may not be unique to the fly olfactory system. When mice perform a visual discrimination task, neurons in the primary visual cortex that disambiguate stimulus identity release none or only one action potential, implying that the necessary computation preceding the spike occurs subthreshold (Resulaj et al., 2018). In a separate experimental paradigm, excitatory, recurrently amplified inputs from the medial superior colliculus (mSC) encode looming threat intensity; they are integrated to overcome a synaptic threshold imposed by neurons in the dorsal periaqueductal grey (dPAG), initiating escape behaviour (Evans et al., 2018). Whereas $\alpha\beta_c$ KCs seem to implement both the integration process and terminating criterion, dPAG neurons merely threshold summed synaptic inputs transmitted from the relevant collicular population. On the whole, because the generation of an action potential represents a natural cutoff of a continuously evolving variable, neural correlates of sequential sampling that compute below threshold may prove to be more prevalent in other decision-making circuits than previously thought.

1.5 Aims

Given the putative neural mechanism of temporal integration in $\alpha\beta_c$ KCs, my work intends to establish a causal relationship between neural activity in these cells and decision-making behaviour. The key experiment is to activate either the 'up' or 'down' population, or to inhibit both, during odour discrimination. Concomitant changes in reaction time and choice accuracy are expected if these neurons' activity represents the temporal bottleneck of the decision process. However, distinguishing the two opponent pools genetically poses a technical challenge, since their functional segregation appears to arise from differential connectivity rather than intrinsic cellular properties (the same neuron can be classified as an 'up' or 'down' cell depending on the olfactory context). Nonetheless, since the membrane potential of 'up' cells is closer to spiking (than that of 'down' cells) at odour onset, small, EPSC-like currents would, in principle, nudge it across spike threshold, while the membrane potential of 'down' cells remains below threshold (even after light-induced depolarisations). The resultant effect will be a selective activation of 'up' KCs during increases in odour concentration, and vice versa. The optical insertion of such currents, which will also avoid directly firing the KC-MBON synapses to trigger an immediate choice, can be achieved by targeting light-gated cation channels (e.g., Chrimson; Klapoetke et al., 2014) to the dendrites of $\alpha\beta_c$ KCs. To suppress neural activity during behaviour, the algal *Guillardia theta* anion channelrhodopsin-1 (*Gt*ACR1) can be used, taking advantage of its high conductance and rapid kinetics (Govorunova et al., 2015).

Specifically, this thesis aims to 1) generate the appropriate optogenetic tools tailored for targeted photostimulation, and 2) utilise these tools for closed-loop, bidirectional manipulation of $\alpha\beta_c$ KC activity during olfactory decision-making, investigating the behavioural consequences in speed and accuracy.

What I cannot create, I do not understand.

— Richard Feynman

2 Methods

2.1 Fly strains and culture

Fly strains were cultivated on standard cornmeal agar under a 12h light:12h dark cycle at 20℃. Experimental flies were heterozygous for all transgenes. The driver lines *NP6024-GAL4* (Tanaka et al., 2008) and *VT030604-GAL4* (VDRC ID 200228) (Kvon et al., 2014) were used to target transgene expression to $\alpha\beta_c$ and $\alpha'\beta'$ KCs, respectively (**Fig.4**). To test for dendritic targeting of Chrimson, flies expressing *UAS-Chrimson::tdTom::motif* (eight motif lines in total) were driven by *NP6024-GAL4* (Tanaka et al., 2008).

The stronger but more restricted line *NP7175-GAL4* (Tanaka et al., 2008) was also used to target expression to $\alpha\beta_c$ KCs. In patch-clamp experiments, *UAS-FRT-stop-FRT-*Gt*ACR1::EYFP* (made from *UAS-*Gt*ACR1::EYFP*, Mohammad et al., 2017, see **2.2 Plasmid construction**) driven by *NP7175-GAL4* was expressed in combination with another $\alpha\beta_c$ KC driver *R58F02-LexA* (Jenett et al., 2012) and *lexAop-FLP*, to conditionally express *Gt*ACR1 in $\alpha\beta_c$ KCs. In addition, *R34B02-LexA* (Pfeiffer et al., 2010) targeted expression in MBON-α2sc.

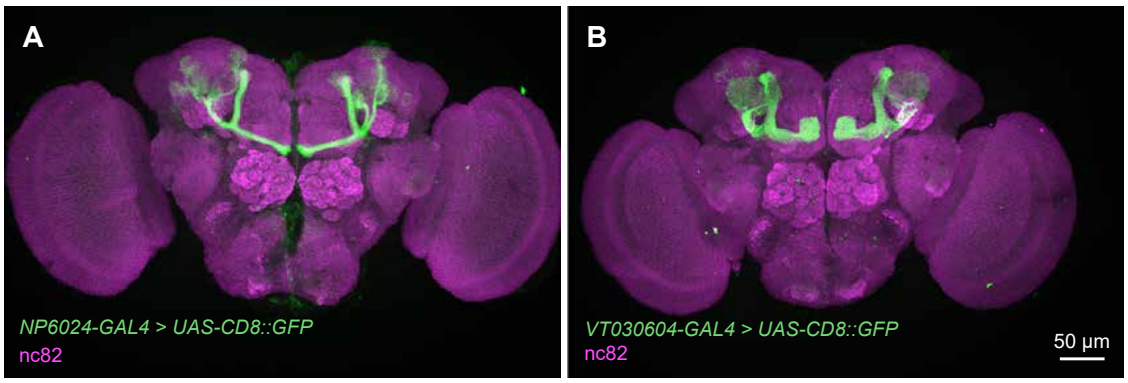


Fig. 4: Expression patterns of KC GAL4 lines.
Maximum intensity projections of confocal image stacks capturing the brains of flies expressing *UAS-CD8::GFP* (green) under the control of *NP6024-GAL4* (**A**) or *VT030604-GAL4* (**B**). Synaptic structures were counterstained with the Bruchpilot antibody nc82 (magenta).

Recordings were also taken from $\alpha\beta_c$ KCs (*NP6024-GAL4* line) expressing *UAS-Chrimson::tdTom::AMPAR-motif.*

For behavioural experiments, flies were raised in darkness and transferred to food supplemented with 0.5–0.6M all-trans retinal (Sigma-Aldrich) in dimethyl sulfoxide 18-24h before being trained and tested as described below. As Chrimson driven by *NP7175-GAL4* was lethal in development, *NP6024-GAL4* was used to target *UAS-Chrimson::tdTom::AMPAR-motif* to $\alpha\beta_c$ KCs.

2.2 Plasmid construction

To generate constructs for targeting Chrimson to the dendritic compartment, eight motifs known to be dendritically targeting were selected (**Table 1**) and codon-optimised for *Drosophila*. Shorter motifs (1-3) were attached to *Chrimson::tdTom* by PCR, using primers that incorporated the motif and linker (SGGSGG), as well as flanking NotI and Acc65I cut sites (**Fig.5A**). Longer motifs (4-8) were synthesised *de novo* (GeneArt, ThermoFisher) and appended to *Chrimson::tdTom* by fusion PCR (**Fig.5B**). First, the motif sequence and *Chrimson::tdTom* were separately

amplified, adding restriction enzyme cut sites and a region of overlap: the end of the *Chrimson::tdTom* fragment would extend to overlap with the start of the motif sequence, and vice versa. Subsequently, annealing of the overlapping sequence between the two fragments was followed by overlap extension by DNA polymerase from the 3'-ends of the overlap region. The final amplified product was a single fragment as a result of the attachment of the motif sequence to *Chrimson::tdTom*, which was then cloned into *pJFRC-MUH* (empty cloning vector with *10XUAS*).

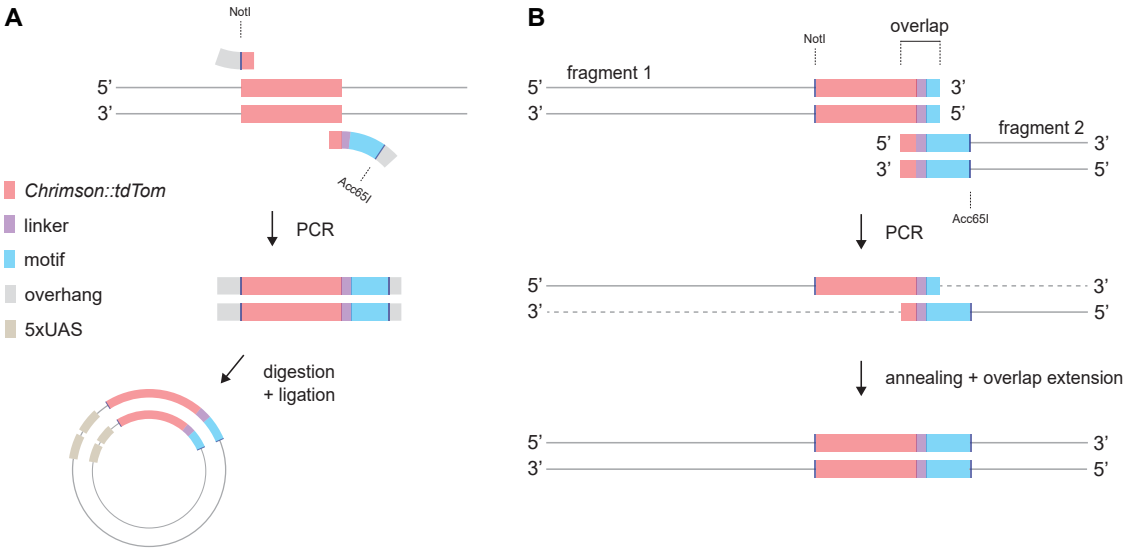


Fig. 5: Appending dendritically targeting motifs to *Chrimson::tdTom*.
A. Short targeting motifs were appended to *Chrimson::tdTom* using PCR, with primers that included the motif, linker (SGGSGG), and flanking restriction sites. The amplified product was then inserted into an empty cloning vector containing *10XUAS*. **B.** Longer targeting motifs were synthesised *de novo*. The motif sequence and *Chrimson::tdTom* were separately amplified to incorporate restriction sites and an overlap region. In fusion PCR, the two fragments annealed and extended from the overlapping region, yielding a single fragment that consisted of the motif attached to *Chrimson::tdTom*.

The genetic intersection strategy for restricted expression of Gt*ACR1* utilised the *FRT-stop-FRT* cassette. The FLP recombinase derived from *Saccharomyces cerevisiae* recognises short FRT sequences flanking a transcriptional termination STOP element (taken from SV40; Nern et al., 2011). As the *FRT* sites are oriented in the same direction, site-specific recombination results in the excision of the STOP element. Thus, expression of the transgene downstream of the cassette

is conditional upon the presence of FLP recombinase. To generate *UAS-FRT-stop-FRT-GtACR1::EYFP*, *FRT-stop-FRT* was cloned from *pJFRC177-10XUAS-FRT-stop-FRT-Chrimson::tdTom* (made by Ruth Brain) into *pJFRC7-20XUAS-GtACR1::EYFP* (gift from Adam Claridge-Chang) by restriction enzyme cloning, using 5' primers (GGGGAAGATCTGAAGTTCCTATACTTTCTAGA, CGCCGC-TCGAGGAAGTTCCTATTCTCTAGAAA) which incorporated flanking BglII and XhoI cut sites. See **Appendix** for the full list of primers.

Constructs were sent to BestGene for embryonic injections and transformant screening. The landing sites were either attP40 (ch2) or attP2 (ch3).

Motif description	**Amino acid sequence**	**Reference**
Shal; 16-aa C-terminal di-leucine motif that interacts with SIDL	FELQHHHLLRCLEKTT	Rivera et al., 2003
Rabbit telencephalin; last 17 aa of cytoplasmic domain	AESPAGGEVFAIQLTSA	Mitsui et al., 2005
Mouse telencephalin; last 17 aa of cytoplasmic domain	AESPADGEVFAIQLTSS	Nicolai et al., 2010
Neuroligin-1; 32 aa in cytoplasmic domain	VVLRTACPPDYTLAMRRSPDDVPLM TPNTITM	Rivera et al., 2003
Melanophilin; Myosin Va binding domain that binds to the Myosin Va globular tail domain	RDQPLNSKKKKRLLSFRDVDFEEDSD	Lewis et al., 2009
AMPAR GluR1 subunit; 39 aa in proximal cytoplasmic tail	EFCYKSRSESKRMKGFCLIPQQSINE AIRTSTLPRNSGA	Ruberti & Dotti, 2000
nAChR alpha7 subunit; tyrosine-di-leucine domain in M3-M4 IC loop	GEDKVRPACQHKPRRCSLASVELSA GAGPPTSNGNLLYIGFRGLEGM(H)	Xu et al., 2006
Fusion motif; telencephalin C-terminal 17 aa + K_v2.1 cytoplasmic C-terminal 65-aa fusion	QSQPILNTKEMAPQSKPPEELEMSSM PSPVAPLPARTEGVIDMRSMSSIDSFI SCATDFPEATRF-GSGSGSGSGS-AES PADGEVFAIQLTSS	Messier et al., 2018

Table 1: Eight putative dendritically targeting motifs were synthesised and appended to *Chrimson::tdTom*.

2.3 Odour-guided decision-making task

To minimise the dimensionality of the vast 'odour space' represented in the KCs, only the monomolecular odour 4-methylcyclohexanol (MCH; Quinn et al., 1974) was used in the task. Male flies aged 7-10 days were first trained in opaque plexiglass chambers (50 mm long, 5 mm wide, 1.3 mm high; see DasGupta et al., 2014; Groschner et al., 2018) with printed circuit boards as floors and ceilings, in a dodecaplex setup (not shown) that could accommodate a maximum of twelve chambers. Flies were then transferred for video acquisition during the testing phase to an identical chamber except for the replacement of circuit boards with float glass strips (UQG Optics), in a custom-made 6-chamber testing apparatus (**Fig.6A**). A final flow rate of 0.25 L/min per half-chamber was achieved by mixing filtered, flow-controlled (CMOSens, Sensirion) and humidified carrier air with flow-controlled odour streams from bottles containing MCH, in appropriate ratios. The odour delivery system was shared between the training and testing setups, and together with electric shock, controlled by software written in LabVIEW (National Instruments). Each round consisted of six flies being trained and subsequently tested in parallel.

During training, twelve consecutive 20s odour presentations of 10 ppm MCH, interspersed with 20s presentations of clean air, were paired with 1s of 70V electric shock, such that flies acquired learned avoidance. In the 2-min testing period, the fly walked in an environment where half the chamber was perfused with MCH at the reinforced concentration, the other at a lower concentration (1, 4, 5, 7 or 9 ppm) (**Fig.6B**). At the central odour interface, the fly had to choose between turning back or continuing to walk to the other side of the chamber. The odour contrast determined the difficulty of the perceptual decision. In the testing setup, chambers were backlit by 830 nm LEDs (TSHG8400, Vishay) with paper diffusers and individually videoed at 30 frames per second by separate cameras (Raspberry Pi NoIR Camera v2) with an 8-mm lens (MVL8M23, Thorlabs) through an IR filter (FL830-10, Thorlabs). Each camera was connected to a headless Raspberry Pi 4

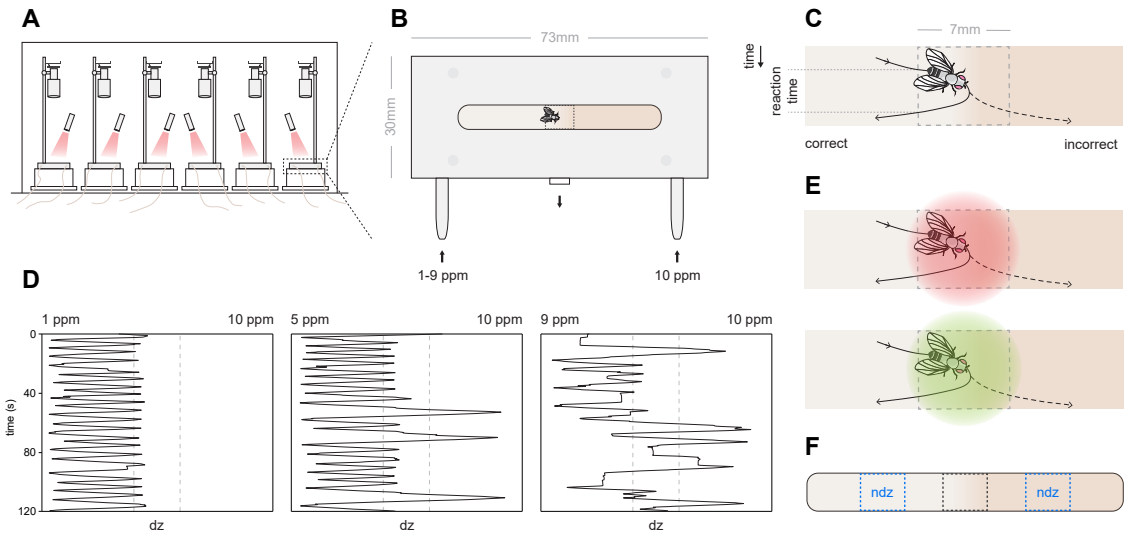


Fig. 6: Behavioural setup of the olfactory decision-making task.
A. Flies were first trained to avoid a high concentration (10 ppm) of MCH using electric shock in a dodecaplex setup (not shown). After training, they were transferred to this multi-chamber, testing setup that allowed six flies to perform the perceptual task in parallel. A separate camera and LED were installed for each fly. For more technical details, refer to text. **B.** The fly walked along the long axis of the behavioural chamber, which was perfused with MCH from both ends. The two sides received different odour concentrations: high (10 ppm; light brown; aversively reinforced), or low (1-9 ppm; beige). The odour contrast at the central interface, where the two streams converged, determined the difficulty of the task. **C.** During the experiment, the fly discriminated between the two concentrations in the central, empirically determined decision zone (7 mm; grey, dashed outline). The choice accuracy depended on which side of the chamber the fly exited the decision zone; the time spent inside the zone was quantified as the reaction time. **D.** Positions of three exemplary flies in the chamber (horizontal dimension) as a function of time (vertical dimension) during testing. When the task was easy, the fly was accurate and fast. Accuracy progressively declined when the task became more difficult (lower odour contrast). dz: decision zone. **E.** For optogenetic interrogation of $\alpha\beta_c$ KCs during the task, the LED illuminated a spot over the fly whenever it entered the decision zone. Red light: single 25 ms pulse, 0.01 (low) or 0.2 mW mm^{-2} (high); green light: constant 5s pulse, 0.2 mW mm^{-2}. **F.** Two off-centre nondecision zones (blue) either side of the decision zone were defined for the computation of transit times. ndz: nondecision zone.

(Model B, 4GB), communicating with a host PC via TCP/IP over a local network. The mechanical design of the mounts for the chambers and Pi cameras was drawn by Clifford Talbot in SolidWorks 2016 and 3D-printed (Objet Connex 260).

For optogenetic interrogation, a train of photostimulation pulses was triggered via a microcontroller running at 16 MHz (Arduino Mega 2560) whenever the fly

entered an empirically defined central decision zone, 7 mm in length (DasGupta et al., 2014) (**Fig.6E**). The motion detection software ran on each Pi individually. Real-time position data were extracted every three frames by subtracting the most recent video image from a background acquired before testing. Non-zero pixel clusters in the difference image were intensity- and size-thresholded; the centroid of the largest cluster was taken as the position of the fly. This software, written in Python 3.6, together with the microcontroller program in C in the Arduino 1.8 environment and the host PC virtual instrument in LABVIEW (National Instruments), was written by Clifford Talbot. The red (624 nm, ILH-GD01-RED1-SC201, Intelligent LED Solutions) and green (523 nm, LZ1-10G102-0000, LED Engin) LEDs were mounted on aspheric condenser lenses (focal length 16 mm, ACL25416U-A, Thorlabs) and powered by a custom circuit based on a constant current driver (Recom RCD-24-0.70 Vref). The circuit was designed by John-Paul Moszynski. For the optogenetic activation experiment with Chrimson, single 25 ms pulses of red light at either low (0.01 mW mm^{-2}) or high (0.2 mW mm^{-2}) intensity were delivered upon the fly's entry into the decision zone. For the optogenetic silencing experiment with *Gt*ACR1, the fly inside the decision zone was illuminated with a constant 5s pulse of green light (0.2 mW mm^{-2}), before the LED timed out. Reentry would again trigger illumination.

Each round consisted of six flies performing in parallel the decision-making task at the same perceptual difficulty, chosen at random. For each genotype, control rounds without light were interleaved with optogenetic rounds.

2.4 Behavioural analysis

Behavioural data were analysed offline in Python. Videos showing excessive grooming or animals making <2 end-to-centre runs were discarded. For the remaining videos, the positions (centroid) of the flies were extracted by subtracting the current frame from the average image of the video and smoothed by computing a moving average of ten frames (fly trajectories over time shown in **Fig.6D**). The time between entry into and exit from the decision zone was taken as the reaction time (DasGupta et al., 2014) (**Fig.6C**). Individual accuracy scores from combining correct and incorrect choices during the test period (choosing the side of the lower concentration was considered correct) were used to calculate population averages. For a run into the zone to be considered a decision (as opposed to a dash across the zone without responding to the odour interface), the fly had to slow down to at least 10% of its entry speed (instantaneous speed over one frame when entering the zone). The average speed between entry and speed drop-off was defined as decision zone speed. Runs in which the fly stayed in the zone for more than 15s were also discarded. To calculate the average walking speed of the flies, off-centre nondecision zones (of the same size) either side of the decision zone were defined (**Fig.6F**). The walking speeds across these zones for every fly were computed and averaged within each difficulty condition. The reaction times for individual decisions were then normalised for walking speed by multiplying by the ratio of decision zone speed to mean walking speed:

$$normalised\ RT = RT \times \frac{decision\ zone\ speed}{mean\ walking\ speed}$$

Normalised reaction times (from now on simply referred to as "reaction times" in the analysis) and task accuracies were pooled and plotted as functions of task difficulty to yield chronometric and psychometric functions, respectively. These functions were then analysed with drift-diffusion models. In addition, transit times of the flies were computed as the time taken to traverse the nondecision zones (**Fig.6F**), without normalisation.

2.5 Drift-diffusion models

A simple version of the diffusion model coupled with the simplest scaling assumptions is considered here (Palmer et al., 2005). In this model, evidence is accumulated over time until an upper or lower bound is reached, at which point a decision is committed. In the example trial (**Fig.1**), the relative evidence, or decision variable, evolves with mean drift rate μ towards the bounds A or -B; excluding residual time, the path at time t would have a mean of μt and variance of $\sigma^2 t$ (σ is the diffusion coefficient). For each stimulus condition, there are four parameters — these can be further restricted based on several assumptions. First, stimulus strength is assumed to only affect the drift rate. Second, response is assumed to be unbiased, and thus A=B. Third, the noise defined by the diffusion coefficient σ is assumed to be constant across conditions. Furthermore, because the diffusion process models decision time but not sensory and motor latencies, reaction time T is treated as having additive and independent components of pure decision time and other residual times, i.e.,

$$T = t_D + t_R$$

where t_D and t_R are decision time and residual time, respectively. Solving the first-passage problem for the decision variable (i.e., the probability of the decision variable reaching a bound at a specified time) yields analytical predictions of accuracy (probability of choosing side a, P_a) and reaction time T in Equations (1) and (2) that depend only on the parameters bound height A, drift rate μ, diffusion coefficient σ, and mean residual time t_R (Bogacz et al., 2006; Palmer et al., 2005):

$$P_a = \frac{1}{1 + e^{-2\frac{A\mu}{\sigma^2}}} \tag{1}$$

$$T = \frac{A}{\mu} \tanh(\frac{A\mu}{\sigma^2}) + t_R \tag{2}$$

As A, μ, and σ all share units of relative evidence and appear in the expressions as ratios, A and μ can be normalised by the noise (σ) to give normalised bound A' and normalised drift rate μ', where $A' = \frac{A}{\sigma}$ and $\mu' = \frac{\mu}{\sigma}$. To address stimulus

scaling, the simplest linear relation is assumed between task difficulty x and normalised drift rate μ':

$$\mu' = k_i x \tag{3}$$

where k_i is the measure of sensitivity in this proportional-rate diffusion model, and may vary in different conditions. Here, the task difficulty x is quantified as:

$$x = \log \frac{[left]}{[right]}$$

i.e., the log ratio of the odour concentrations of the two sides. Incorporating parameter normalisation and stimulus scaling into Eq. (1) and (2):

$$P_{i,x} = \frac{1}{1 + e^{-2A'k_i(-x)}} \tag{4}$$

$$T_{i,x} = \frac{A'}{k_i x} \tanh(A'k_i x) + t_R \tag{5}$$

$P_{i,x}$ describes the probability of the fly choosing left at difficulty x for genotype i. For the range of parameter values that would fit reaction time data, Eq. (4) gives $P_{i,x} \approx 1$ at $x = -1$ and $P_{i,x} \approx 0$ at $x = 1$. Since flies did not achieve perfect accuracy in the task, even at the lowest difficulty, choice probability had to be normalised by the maximal and minimal accuracies P_{max} and P_{min}:

$$P_{i,x} = P_{min} + (P_{max} - P_{min}) \frac{1}{1 + e^{-2A'k_i(-x)}} \tag{6.1}$$

As $P_{i,x}$ is symmetrical around 0.5, $P_{min} = 1 - P_{max}$, and Eq. (6.1) simplifies to:

$$P_{i,x} = (1 - P_{max}) + (2P_{max} - 1) \frac{1}{1 + e^{-2A'k_i(-x)}} \tag{6.2}$$

From Eq. (6.2), two models were considered. In Model 1, P_{max} was empirically determined, similar to the analysis in DasGupta et al. (2014) and Groschner et al. (2018). More specifically, P_{max} was taken as the mean of the accuracies at the lowest difficulties i.e., 1 vs 10ppm and 10 vs 1ppm:

$$P_{max} = \frac{P(x = -1) + 1 - P(x = 1)}{2}$$

However, since a drop in P_{max} (flattening of the psychometric curve) was observed in certain optogenetic stimulation conditions, in particular at high light intensities, a model that fit P_{max} might better describe how optical activation of $\alpha\beta_c$ KCs during behaviour influenced choice accuracy. Model 2 treated P_{max} as a free parameter.

For both models, analytical expressions (5) and (6.2) were simultaneously fit to reaction time and accuracy data using the least-squares Levenberg-Marquardt algorithm (within the minimize() function in Python LMFIT package; Newville et al., 2016) to estimate the free parameters A', k_i, t_R, and only in Model 2, P_{max}. To compare different light conditions for each genotype, the models were first fit to non-stimulated data. For simplicity, optogenetic stimulation was assumed to exert no effect on sensory and motor latencies; thus, t_R from this fit was taken and used as a constant in the models for light-stimulated data.

Models 1 and 2 differed only in the treatment of P_{max}, either as an empirically determined constant (Model 1) or a free parameter (Model 2). Nevertheless, with the introduction of this extra parameter in Model 2, there was a risk of overfitting to the noise in the data, in which case the model not only captured the underlying generating function, but also randomness due to the sample being an imperfect representation of the population. To test for overfitting, the two models were 5-fold cross-validated (**Fig.18C**). Model fitting was first performed on 80% (training) of randomly shuffled data, which generated a set of estimated parameters. This set was then used in the model to predict the remaining 20% (test) of the data. The process was repeated four more times, each time with different, non-overlapping sets of training and test data. Model predictions were plotted against the corresponding sets of test data, and R^2 quantified the goodness of prediction, which was compared between the two models. If there was overfitting, then low and variable R^2 values would be expected.

Although R^2 represents an intuitive measure of goodness-of-fit, it is not recommended to be used on its own for the comparison of nonlinear models (Spiess and

Neumeyer, 2010). Thus, two additional approaches were employed. In the first one, the extra sum-of-squares F test compares two nested model with least-squares regression. If the more complicated model is better, then the relative increase in sum-of-squares (SS, from complicated to simple model) should be greater than that of the degrees of freedom (DF):

$$\frac{SS_1 - SS_2}{SS_2} > \frac{DF_1 - DF_2}{DF_2}$$

The F ratio quantifies the relationship between the two:

$$F = \frac{(SS_1 - SS_2)/(SS_2)}{(DF_1 - DF_2)/(DF_2)}$$

The F test assesses whether this ratio was significantly greater than 1, in which case the more complicated model will be appropriate.

In the second approach, the Bayesian information criterion (BIC) (Schwarz, 1978) evaluates model fitting by balancing the goodness-of-fit and a penalty term for the number of parameters. It is given by:

$$\text{BIC} = N \ln(\frac{SS}{N}) + \ln(N) N_{param}$$

where N is the number of data points, and N_{param} is the number of variable parameters. The model with the lowest BIC is preferred. For ΔBIC values ranging from 0-2, evidence against the model with the higher BIC is minimal; 2-6, positive; 6-10, strong; and >10, very strong (Kass and Wasserman, 1995).

For the favoured model, the estimated parameters were plotted and compared across conditions and genotypes. The uncertainty of parameter i was represented by the standard error (see Curve Fitting Guide, GraphPad), taken as:

$$\text{SE}_i = \sqrt{\frac{SS}{DF} * \text{Cov}(i,i)}$$

where $\text{Cov}(i,i)$ is the i^{th} diagonal element of the parameter covariance matrix. The LMFIT package (Newville et al., 2016) calculates the covariance matrix, given by:

$$\text{Cov} = (\boldsymbol{J}^T \boldsymbol{J})^{-1}$$

where $\boldsymbol{J}$ is the Jacobian matrix of the model.

2.6 Bayesian modelling

A Bayesian approach allows inference of the full posterior distribution of each model parameter and thus quantifies their uncertainty, rather than merely estimating a most likely value. The open-source Python package Hierarchical Drift-Diffusion Model (HDDM, Wiecki et al., 2013) was run on a Docker image (created by Hu Chuan-Peng) to analyse reaction time and choice accuracy data. HDDM takes the analytic solution to the probability distribution of the termination times of the drift-diffusion process (Feller, 1968; Wald, 1947) to estimate distributions for drift rate, bound height, residual time, and starting point bias. In the hierarchical version of the model, participants within each group (or conditions) are assumed to be similar to each other, but not identical. Individual parameter estimates are constrained by group-level distributions. However, I observed considerable variability in performance within each light condition, for each task difficulty (data not shown), rendering the aforementioned assumption invalid. Thus, a non-hierarchical model was fit, where the data was considered to be from an individual subject. HDDM uses Markov chain Monte Carlo (MCMC, Gamerman and Lopes, 2006) to estimate the joint posterior distribution of all parameters. 2000 posterior samples were drawn, discarding 20 as burn-in.

In the model, the parameters drift rate and bound height were set to depend on task difficulty, i.e., a separate parameter distribution was estimated for each odour contrast. For each optogenetic condition, the mean drift rates and bound heights, together with their 95% confidence intervals, were plotted against log odour contrast. Drift rates were taken as positive when choosing left was correct, and vice versa. Their absolute values were grouped across difficulty levels and compared between stimulation conditions. In addition, drift rates were linearly related to difficulty in the central range, but saturated at the lowest difficulties (the two extremes where log odour contrast was -1 or 1). Given the previous assumption of linearity between drift rate and task difficulty (Eq. 3), only the central range was

included in linear regression; the slope thus represented the scaling factor k. Since bound height (A) did not appear to vary with difficulty, their values were grouped across task difficulty and compared between stimulation conditions.

2.7 Extrema detection

Choice accuracy and reaction time data were also fit with a model of extrema detection that assumed sequential sampling but no integration (Stine et al., 2020) (**Fig.7**). In this model, evidence is sampled from a stationary distribution until a sample exceeds one of the two bounds, terminating the decision. Evidence within the decision bounds does not affect the decision and is ignored and forgotten. Momentary evidence is modelled as random values drawn from a normal distribution with mean $\boldsymbol{\mu}$. The model primarily depends on the probability of exceeding the bounds $\pm\boldsymbol{A}$ on each sample; these probabilities are:

$$\boldsymbol{p_{+A}} = \frac{\mathbf{1}}{\mathbf{2}}\mathrm{erfc}\left(\frac{\boldsymbol{A} - \boldsymbol{k_i x \Delta t}}{\sqrt{\mathbf{2}\boldsymbol{\Delta t}}}\right) \tag{7}$$

$$\boldsymbol{p_{-A}} = \frac{\mathbf{1}}{\mathbf{2}}\mathrm{erfc}\left(\frac{\boldsymbol{A} + \boldsymbol{k_i x \Delta t}}{\sqrt{\mathbf{2}\boldsymbol{\Delta t}}}\right) \tag{8}$$

where erfc is the complementary error function, $\boldsymbol{x}$ is the log odour contrast, and $\boldsymbol{k_i x} = \boldsymbol{\mu}$, as before. Eq. (7) and (8) describe the density of the momentary evidence distribution beyond the upper and lower bounds. The increment $\boldsymbol{\Delta t}$ was taken as 0.5 ms. The psychometric and chronometric functions are:

$$\boldsymbol{P_{left}} = (\mathbf{1} - \boldsymbol{P_{max}}) + (\mathbf{2}\boldsymbol{P_{max}} - \mathbf{1})\ \frac{\boldsymbol{p_{-A}}}{\boldsymbol{p_{+A}} + \boldsymbol{p_{-A}}} \tag{9}$$

$$\boldsymbol{T} = \begin{cases} \boldsymbol{\Delta t}\frac{\mathbf{1}}{\boldsymbol{p_{-A}}} + \boldsymbol{t_R}, & \text{if } \boldsymbol{x} < \mathbf{0} \\ \boldsymbol{\Delta t}\frac{\mathbf{1}}{\boldsymbol{p_{+A}}} + \boldsymbol{t_R}, & \text{if } \boldsymbol{x} > \mathbf{0} \end{cases} \tag{10}$$

Again, the probability of choosing left was normalised by the maximal and minimal accuracies $\boldsymbol{P_{max}}$ and $\mathbf{1} - \boldsymbol{P_{max}}$, respectively. As before, Eq. (9) and (10) were

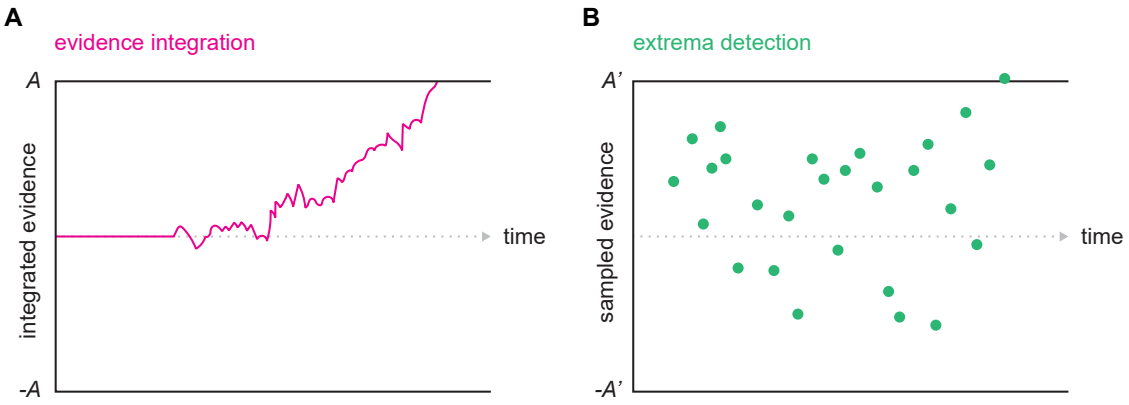


Fig. 7: Evidence accumulation to bound versus extrema detection.
A. In drift-diffusion models, sensory evidence is sequentially sampled and integrated. A decision variable representing integrated evidence (magenta line) evolves over time until a threshold is reached. **B.** In the extrema detection model, evidence is only sequentially sampled (green dots), but not integrated. A decision is committed once a sample exceeds one of the two bounds. *A*, *-A*, *A'*, *-A'*: arbitrary decision bounds. Adapted from Stine et al., 2020.

simultaneously least-squares fit to accuracy and reaction time data of various genotypes and conditions using the Python LMFIT package (Newville et al., 2016) to estimate $\boldsymbol{A}$, $\boldsymbol{k_i}$, $\boldsymbol{t_R}$, and $\boldsymbol{P_{max}}$. $\boldsymbol{t_R}$ from the unstimulated fit was used as a constant for the photostimulation conditions. BIC was used to compare the drift-diffusion and extrema detection models, plotting $\boldsymbol{\Delta}\text{BIC} = \text{BIC}_{\text{extrema}} - \text{BIC}_{\text{DD}}$.

2.8 Structural imaging

Brains of adult flies were dissected in phosphate-buffered saline (PBS; 137 mM NaCl, 3 mM KCl, 8 mM Na_2HPO_4, 1.5 mM KH_2PO_4, pH 7.3), fixed in 4% (w/v) paraformaldehyde for 15 minutes at room temperature, washed three times in PBS for 15 minutes, whole-mounted in Vectorshield (Vector Labs) and imaged on a Leica TCS SP5 confocal microscope with an HCX IRAPO L 25X/0.95W objective (Leica). Images were processed in ImageJ (NIH).

For immunostaining of GFP expressed in $\boldsymbol{\alpha\beta_c}$ and $\boldsymbol{\alpha'\beta'}$ KCs, brains were

blocked in 10% normal goat serum (NGS in 0.3% PBS-Triton) overnight at room temperature, stained with chicken anti-GFP (Abcam, 1:1000) and mouse nc82 (DSHB, 1:10) for 72h at 4℃, washed four times in 0.3% PBS-Triton for 1h at room temperature, stained with goat anti-chicken Alexa Fluor 488 (Thermo Fisher, 1:1000) and goat anti-mouse Alexa Fluor 546 (Thermo Fisher, 1:1000) for 48h at 4℃, washed four times again in 0.3% PBS-Triton for 1h at room temperature before being mounted as described above.

2.9 Fluorescence quantification

Quantification of fluorescence was conducted in ImageJ. For each brain that expressed dendritically targeted Chrimson::tdTom, a smaller stack that included the $\boldsymbol{\alpha\beta}$ lobes (or the calyces) was maximally projected. Each lobe was traced using the ROI tool and its average greyscale value measured, three times per lobe, per hemisphere. These six values were averaged, from which background fluorescence (averaged across three measurements) was subtracted to give $\boldsymbol{F}_{\text{lobe}}$. The same was repeated for the calyces to yield $\boldsymbol{F}_{\text{calyx}}$. The ratio $\boldsymbol{F}_{\text{lobe}}$ to $\boldsymbol{F}_{\text{calyx}}$ was plotted for each genotype and compared.

2.10 Electrophysiology

For in vivo whole-cell patch-clamp recordings, flies aged 1-2 days were fixed to a custom mount with soft thermoplastic wax (Agar Scientific). Cuticle, trachea, adipose tissue, and perineural sheath were surgically removed in a window large enough to provide access to $\boldsymbol{\alpha\beta_c}$ KCs or MBON-$\boldsymbol{\alpha}$2sc in the dorsal brain, with the antennae and antennal nerves intact for measuring odour responses. The brain was continuously superfused with extracellular solution (pH 7.3) containing 5 mM TES, 103 mM NaCl, 3 mM KCl, 26 mM $\mathrm{NaHCO_3}$, 1 mM $\mathrm{NaH_2PO_4}$, 1.5 mM

$CaCl_2$, 4 mM $MgCl_2$, 8 mM trehalose, 10 mM glucose, and 7 mM sucrose (275 mOsM, equilibrated with 5% CO_2 and 95% O_2). Patch pipettes (14–18 MΩ) were fabricated from borosilicate glass capillaries with outer and inner diameters of 1.5 and 0.86 mm (Sutter Instruments), using a PC-10 micropipette puller (Narishige), and filled with solution (pH 7.3) containing 10 mM HEPES, 140 mM potassium aspartate, 1 mM KCl, 4 mM MgATP, 0.5 mM Na_3GTP, 1 mM EGTA, and 10 mM biocytin (265 mOsM). Pipettes were visually targeted to green- or red-fluorescent KC or MBON somata using a combination of epifluorescence and differential interference contrast on an Axioscop 2 FS mot microscope (Zeiss) equipped with a 60X, 1.0 NA water immersion objective (LUMPLFLN60XW, Olympus) and an X-Cite 120PC Q light source (Excelitas Technologies). A red (625 nm) or green (530 nm) LED was positioned ∼10 cm away from the fly, illuminating the exposed dorsal brain at an angle from above.

Signals were acquired at room temperature (21–23℃) with a MultiClamp 700B amplifier (Molecular Devices), lowpass-filtered at 10 kHz, and sampled at 50 kHz using a Digidata 1440A digitizer controlled through pCLAMP 10 (Molecular Devices). Data were corrected for liquid junction potential (Neher, 1992) and analysed with custom procedures using the NeuroMatic package in Igor Pro (WaveMetrics).

In voltage-clamp recordings, to measure *Gt*ACR1-induced photocurrents, membrane potential was stepped from -130 mV to 0 at 10 mV intervals; a 1s pulse of green light came on at ∼3s delay (to inactivate voltage-gated currents) after the voltage step to activate *Gt*ACR1. Current measurements were baseline-corrected to yield pure photocurrents. In current-clamp recordings, bridge balance was used to compensate for series resistance. The most negative membrane potential recorded immediately after break-in, in the absence of a holding current and without correcting for errors introduced through seal conductances, was taken to represent the resting potential. 1s steps of depolarising current, from -15 pA to 50 pA at 5

pA increments, were injected at a pre-pulse potential of -54 mV ± 2 mV. Spikes were detected by finding maxima in the time derivative of the membrane potential trace. For olfactory stimulation, mass flow-controlled streams of MCH-infused air (CMOSens, Sensirion) were directed at the fly's head through a behavioural chamber cut in half; flow rates matched those in behavioural experiments (0.25 l/min). Solenoid valves (The Lee Company) under LabVIEW control (National Instruments) switched between odour streams containing a variable basal (2, 8, 14, or 18 ppm) and a constant peak (20 ppm) concentration of MCH.

2.11 Statistics

Data were first processed and modelled in Python, and then statistically analysed in Prism 7 (GraphPad). Ratios of fluorescence intensity in MB lobes and calyces were compared by one-way ANOVA. Mean reaction times, transit times, and maximal accuracies (for one genotype only) from unstimulated and photostimulated conditions were compared by either one-way ANOVA followed by post-hoc analysis using Tukey's multiple comparison test, or unpaired ***t***-test with Welch's correction, depending on the number of groups. Following the Bayesian analysis of behavioural data with HDDM, drift rate and bound height parameters across stimulation conditions were compared by one-way ANOVA followed by post-hoc analysis using Tukey's multiple comparison test.

It is our choices, Harry, that show what we truly are,
far more than our abilities.

— Albus Dumbledore

3 Results

3.1 Construction of optogenetic tools

To perform behavioural experiments in which the activity of $\boldsymbol{\alpha\beta_c}$ KCs could be bidirectionally manipulated, I first sought to generate the appropriate optogenetic tools. In the activation experiment, the idea was to append a short motif sequence that targeted Chrimson to the dendritic compartment such that its optical activation during the perceptual task would inject small, EPSC-like currents, nudging the activity of either 'up' or 'down' cells across spike threshold without directly firing KC-MBON synapses. The red-shifted channelrhodopsin Chrimson (Klapoetke et al., 2014) was chosen not only because of its fast kinetics, but also the fact that using red photostimulation would reduce light-evoked behavioural artifacts and improve cuticle penetration. In the KC inhibition experiment, modifications to the *Gt*ACR1 transgene were required to overcome the channel's leaky expression.

Dendritic targeting of Chrimson

Since the FoxP target, voltage-gated potassium channel Shal in $\boldsymbol{\alpha\beta_c}$ KCs contained a dendritic targeting di-leucine (LL) motif (Rivera et al., 2003), it was the obvious choice to use this motif to target Chrimson expression. The Shal motif was appended onto Chrimson::tdTom during PCR amplification, using primers that incorporated a flexible linker, the motif, and restriction sites (see **Methods**). Surprisingly, flies expressing this construct in $\boldsymbol{\alpha\beta_c}$ KCs showed around twice the level of fluorescence in the axonal ($\boldsymbol{\alpha\beta}$ lobes) compared with the somatodendritic (calyces) compartments (**Fig.8A,I**). The fluorescence quantification method tended to slightly underestimate the level in the sparser calyces than in the denser lobes, since it was harder to precisely trace the area of sparse structures – an overestimation of area would lead to a lower mean greyscale value. However, this marginal imprecision was not sufficient to mask the inefficacy of the Shal motif to dendritically target Chrimson::tdTom.

I then tested a series of known dendritic targeting motifs, including that of the cell adhesion molecule telencephalin (TLCN) in rabbit (Mitsui et al., 2005) and mouse (DenMark; Nicolaï et al., 2010), murine neuroligin-1 (NLG1; Rosales et al., 2005), the myosin Va binding domain from melanophilin (MLPH, Lewis et al., 2009), human AMPA receptor (AMPAR GluR1 subunit; Ruberti and Dotti, 2000), and rat nicotinic acetylcholine receptor (nAChR) $\boldsymbol{\alpha}$7 subunit (Xu et al., 2006) (**Fig.8B-G**). I further tested a hybrid motif that fused residues from the potassium channel $K_v2.1$ and TLCN (from now on referred to as fusion motif, **Fig.8H**), previously shown to effectively target *Gt*ACR2 to the somatodendritic compartment of mouse pyramidal neurons (Messier et al., 2018). As with the Shal motif, most constructs were expressed more strongly in the $\boldsymbol{\alpha\beta}$ lobes, showing an approximately twofold difference in expression compared with the calyces (**Fig.8I**). Strikingly, Chrimson::tdTom appended with the AMPAR motif was very faint in the axonal compartment, but expressed highly in the somata and dendrites (**Fig.8F**). Fluorescence in the lobes was only around half of that in the calyces (**Fig.8I**), which

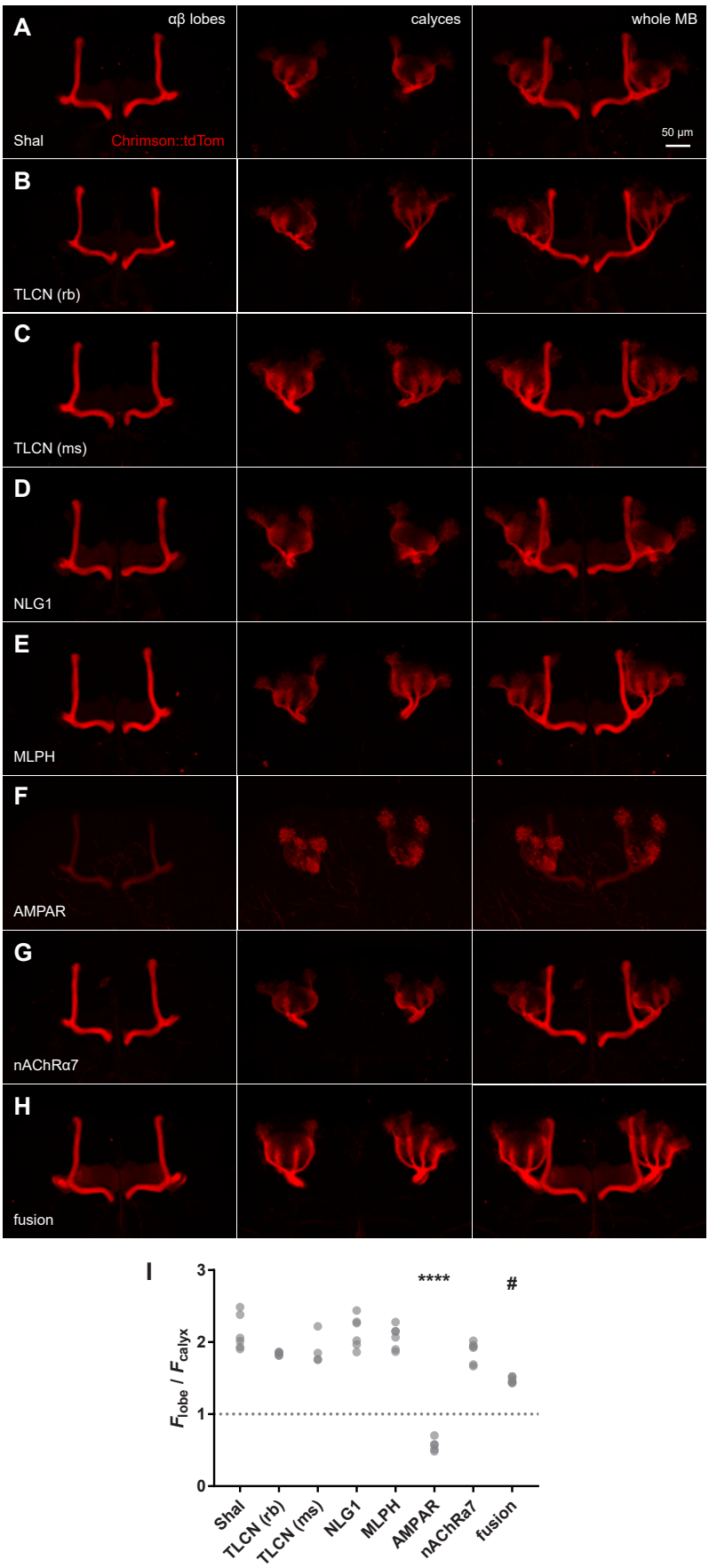


Fig. 8: Dendritic targeting of *Chrimson::tdTom* by the AMPAR motif.
(Continued on the following page)

was evidence for successful dendritic targeting. With this subcellularly localised channel, red light would in theory deliver smaller depolarisations (compared with the untargeted channel) that would nudge the neurons towards spike threshold, selectively activating the 'up' or 'down' population (depending on their membrane potentials). This spatially more precise activation would also avoid the immediate spiking of downstream MBONs. Nonetheless, functionality of this tool remained to be tested electrophysiologically (see **Results 3.2**).

For Chrimson::tdTom::fusion-motif, expression was elevated in the calyces, compared with that of many other constructs (**Fig.8A-H**). However, it also remained quite high in the $\boldsymbol{\alpha\beta}$ lobes. Indeed, the ratio $\boldsymbol{F}_{\text{lobe}}$ / $\boldsymbol{F}_{\text{calyx}}$ was lower, at $\sim$1.5 (**Fig.8I**), but since it was still well above 1 the motif could not be considered as dendritically targeting.

It was unclear why the human AMPAR motif was particularly effective in the dendritic targeting of Chrimson::tdTom in fly KCs, whereas the other ones, from various organisms, were much less so. In any case, I have made a novel Chrimson construct that targets the channel's expression to the somatodendritic compartment of the cell. This tool will hopefully be useful in many experiments where finer control in optogenetic activation of neurons is favoured. In this study, this tool was well-suited to optically inject EPSC-like currents into $\boldsymbol{\alpha\beta_c}$ KCs with red illumination during decision-making behaviour.

Fig. 8: (Continued from the previous page) **A-H.** Expression patterns of *Chrimson::tdTom::motif* in $\boldsymbol{\alpha\beta_c}$ KCs. Motifs are taken from Shal (**A**), rabbit TLCN (**B**), mouse TLCN (**C**), NLG1 (**D**), MLPH (**E**), AMPAR (**F**), nAChR$\boldsymbol{\alpha}$7 (**G**), and a fusion of residues from K_v2.1 and TLCN (**H**). For each construct, expression in the $\boldsymbol{\alpha\beta}$ lobes (left), calyces (middle), and the whole MB (merged, right) are shown. Only *Chrimson::tdTom::AMPAR-motif* exhibits targeting to the somatodendritic compartment (calyces), with drastically reduced expression in the axonal projections ($\boldsymbol{\alpha\beta}$ lobes). **I.** The ratio of fluorescence intensity between the lobes and calyces is significantly lower when the AMPAR motif is appended to *Chrimson::tdTom* (one-way ANOVA, **** $\boldsymbol{p < 0.0001}$). The fusion motif appears to increase dendritic expression, reducing the ratio (# $\boldsymbol{p < 0.0001}$); but since the ratio >1, the motif is not considered dendritically targeting. rb: rabbit. ms: mouse.

Targeted expression of *Gt*ACR1

I first sought to target the expression of the *UAS*-Gt*ACR1* transgene using an $\boldsymbol{\alpha\beta_c}$ KC GAL4 driver (*NP7175-GAL4* or *NP6024-GAL4*). However, to my surprise, I discovered that green light could paralyse *UAS*-Gt*ACR1::EYFP* flies in the absence of any GAL4 drivers; these flies would resume normal locomotion when the illumination stopped. This suggested a case of leaky expression of the *UAS* transgene that caused light-induced silencing of motor control neurons, or more likely, in muscles, as no region of strong *Gt*ACR1 expression, based on EYFP fluorescence, could be identified in the brain. These flies were unsuitable for optogenetics in my behavioural experiments, since it would be impossible to use green light to precisely hyperpolarise $\boldsymbol{\alpha\beta_c}$ KCs during the decision-making task. Nonetheless, it should be noted that the tool had been widely used in the field, in some instances to probe neuronal function in climbing (Mohammad et al., 2017) or larval crawling (Mauss et al., 2017) assays.

To circumvent this problem of transgene leakiness, I inserted an *FRT-stop-FRT* cassette between *UAS* and Gt*ACR1* by molecular cloning (see **Methods**) such that the opsin's expression was conditional on the presence of FLP recombinase, a protein that would recognise the FRT sites and excise the transcriptional STOP element. Flies expressing *UAS-FRT-stop-FRT*-Gt*ACR1::EYFP* did not freeze when illuminated with green light. This transgene could then be combined with conditional expression of FLP to target *Gt*ACR1 to $\boldsymbol{\alpha\beta_c}$ KCs.

Using the driver *GMR58F02-LexA*, I introduced FLP recombinase to $\boldsymbol{\alpha\beta_c}$ KCs with *lexAop-FLP*. In combination with *NP6024-GAL4* and the optogenetic construct I made, *Gt*ACR1 was successfully restricted to $\boldsymbol{\alpha\beta_c}$ KCs, with clear EYFP expression in the calyces and $\boldsymbol{\alpha\beta}$ lobes (**Fig.9**).

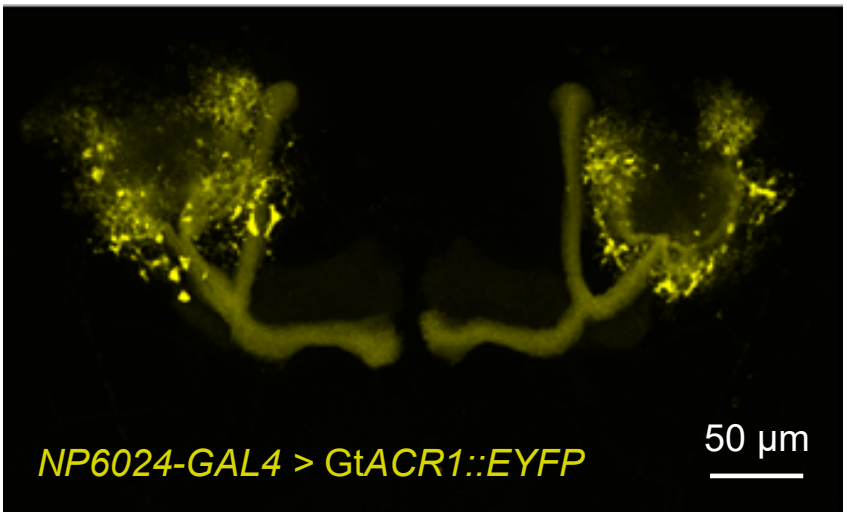


Fig. 9: Restricted expression of *Gt*ACR1 in $\alpha\beta_c$ KCs.
Genetic intersection of *UAS-FRT-stop-FRT*-Gt*ACR1* and *lexAop-FLP* using the drivers *NP6024-GAL4* and *GMR58F02-LexA*, respectively, restricts the expression of *Gt*ACR1::EYFP to $\alpha\beta_c$ KCs. This strategy circumvents the leaky expression of *UAS*-Gt*ACR1*.

3.2 Functional testing of optogenetic tools

To test the functional efficiency of the optogenetic constructs, I performed whole-cell patch-clamp recordings of $\alpha\beta_c$ KCs expressing either dendritically targeted Chrimson::tdTom or *Gt*ACR1::EYFP. Despite the fact that stimulation conditions and thus cellular response kinetics were expected to vary considerably between the behavioural chamber and electrophysiological rig, given that the fly was freely moving in the former, but head-fixed on a mount and having an open cuticular window in the latter, patch-clamp recordings remained a convincing and important procedure to verify the functionality of optogenetic tools. Results that showed efficient optical activation or inhibition of $\alpha\beta_c$ KC activity would give credence to subsequent behavioural experiments.

Dendritically targeted Chrimson in $\alpha\beta_c$ KCs

In the mushroom body calyces, red-fluorescent KC somata expressing Chrimson::tdTomato were targeted. Current clamp recordings demonstrated that a 2s pulse of 4 mW mm^{-2} red light was able to depolarise the membrane potential (**Fig.10A**). Shorter pulses at 1s, 500 ms, 250 ms, 100 ms, 50 ms, and 25 ms were also effective in increasing the membrane potential, which displayed a variety of waveforms that corresponded to the stimulus duration (**Fig.10C,D**). The maximum depolarisation recorded was around 10 mV. Theoretically, this amplitude of increase would likely drive the neuron from resting potential to spike threshold, since Groschner et al. (2018) reported an average potential difference of only 8.2 mV. It was therefore rather unusual that spiking was not observed, although it should be stated that the recording shown was only from one neuron. Regardless of whether this was due to a poor seal between the cell and the pipette or disrupted cellular kinetics as a result of transgene and channel expression, the absence of spikes might actually be leveraged to suit the purpose of the study. Since the light intensity selected was lower in the behavioural experiments, compounded by the diffusion of light through a layer of cuticle to reach the cells, the increase in membrane potential was expected to be smaller than when the cells were recorded in the rig. This would essentially constitute EPSP-like depolarisations (∼1–1.2 mV) that would be ideal in mimicking quanta of sensory information during the odour-guided task, rather than instantaneously firing the KC-MBON synapses. Of course, if the lack of spiking resulted from technical challenges in the electrophysiological recordings, then whether or not strong red light could spike KCs that expressed dendritically targeted Chrimson would remain to be determined; but the argument that weaker light-induced depolarisations during behaviour were suited to the experimental design would still stand.

Interestingly, a non-fluorescent, Chrimson-negative KC showed a slight hyperpolarisation (∼2.5 mV) upon being illuminated by a 2s pulse of red light (**Fig.10B**),

pointing to a case of KC-KC inhibition, potentially via the giant GABAergic neuron APL (Lin et al., 2014; Vrontou et al., 2021). Given the proximity of this neuron and its similar morphology to the red-fluorescent cells, it could likely be an unlabelled $\boldsymbol{\alpha\beta_c}$ KC. Since 'up' and 'down' cells could act as competing integrators to direct olfactory decision-making (Groschner et al., 2018), pooled inhibition between them becomes important to ensure that the two groups are anti-correlated (Vrontou et al., 2021, see **Discussion**). Taken together, it was evident that the *UAS-Chrimson::tdTom::AMPAR-motif* construct I made was functional: $\boldsymbol{\alpha\beta_c}$ KCs expressing it were depolarised by pulses of red light.

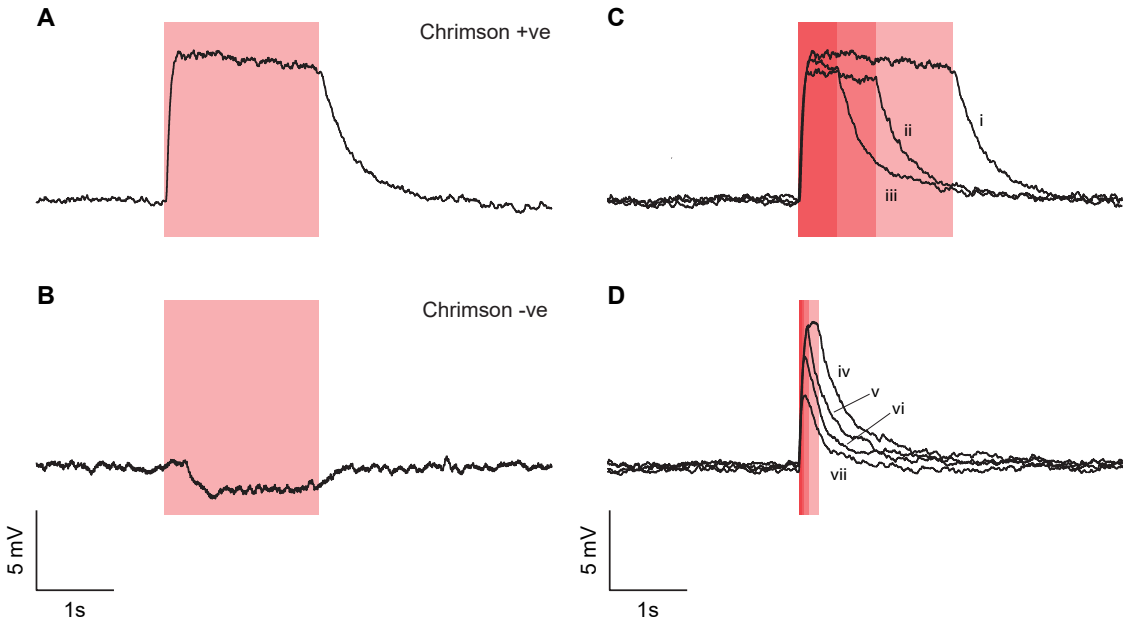


Fig. 10: Optogenetic activation of $\alpha\beta_c$ KCs using Chrimson.
Current clamp recordings of an $\boldsymbol{\alpha\beta_c}$ KC. **A.** A 2s pulse of 4 mW mm^{-2} red light elicited a ∼10 mV increase in the membrane potential of a Chrimson-positive cell. No spikes were detected. **B.** In a Chrimson-negative cell, red light induced a delayed hyperpolarisation (∼2.5 mV). **C, D.** Pulses of variable lengths — 2s (**i**), 1s (**ii**), 500 ms (**iii**), 250 ms (**iv**), 100 ms (**v**), 50 ms (**vi**), and 25 ms (**vii**) — could cause depolarisations of different waveforms dependent on stimulus duration. Resting membrane potential: -28 ± 2 mV.

*Gt*ACR1 in $\alpha\beta_c$ KCs

For green-fluorescent KCs expressing *Gt*ACR1::EYFP, current recordings to 10 mV voltage steps from -130 to 0 mV showed strong photocurrents under a 1s pulse of 1 mW mm^{-2} green illumination (**Fig.11A**). Despite the waveforms for chloride influx and efflux sharing a similar fast rise phase, positive photocurrents (influx) showed a slower, more sustained decay compared with that of negative currents. Meanwhile, photocurrents were not observed in nearby *Gt*ACR1-negative KCs (**Fig.11B**). The *I-V* relationship between photocurrents and voltage steps estimated the reversal potential ($\boldsymbol{I = 0}$) for the channel to be -96 mV (**Fig.11C**), which was considerably higher than the theoretical chloride reversal potential of -120 mV given the experimental conditions. A possible explanation to this discrepancy could be the presence of some *Gt*ACR1-mediated cation conductance, such as that of Ca^{2+}. But since the original study reported that changing the cation composition did not affect *Gt*ACR1's reversal potential (Govorunova et al., 2015), implying cation impermeability, I did not further investigate the matter.

In current clamp, voltage recordings demonstrated fast light-evoked hyperpolarisations that depressed the membrane potential for a maximum amplitude of ∼21 mV (**Fig.11F**). Shorter pulses (25 ms, 100 ms) of green light also elicited hyperpolarisations, but these were smaller than the maximum achieved by 1s and 2s pulses: the amplitude of membrane potential decrease was only ∼9 mV for the 25 ms pulse. Voltage recordings to steps of depolarising current from -15 to 50 pA showed that spiking activity (at elevated membrane potentials) (**Fig.11D**) was completely abrogated by green light (**Fig.11E**) — membrane potential waveforms became compressed when the cell was illuminated. In addition, since the antennae were kept intact when the fly was mounted, odour responses in KCs could be recorded. The fly was stimulated with a stream of MCH at 20 ppm, delivered through the opening of a behavioural chamber cut in half that was designed to recreate the fly's experience in the decision-making task. An 'up' $\boldsymbol{\alpha\beta_c}$ KC responded to the onset of

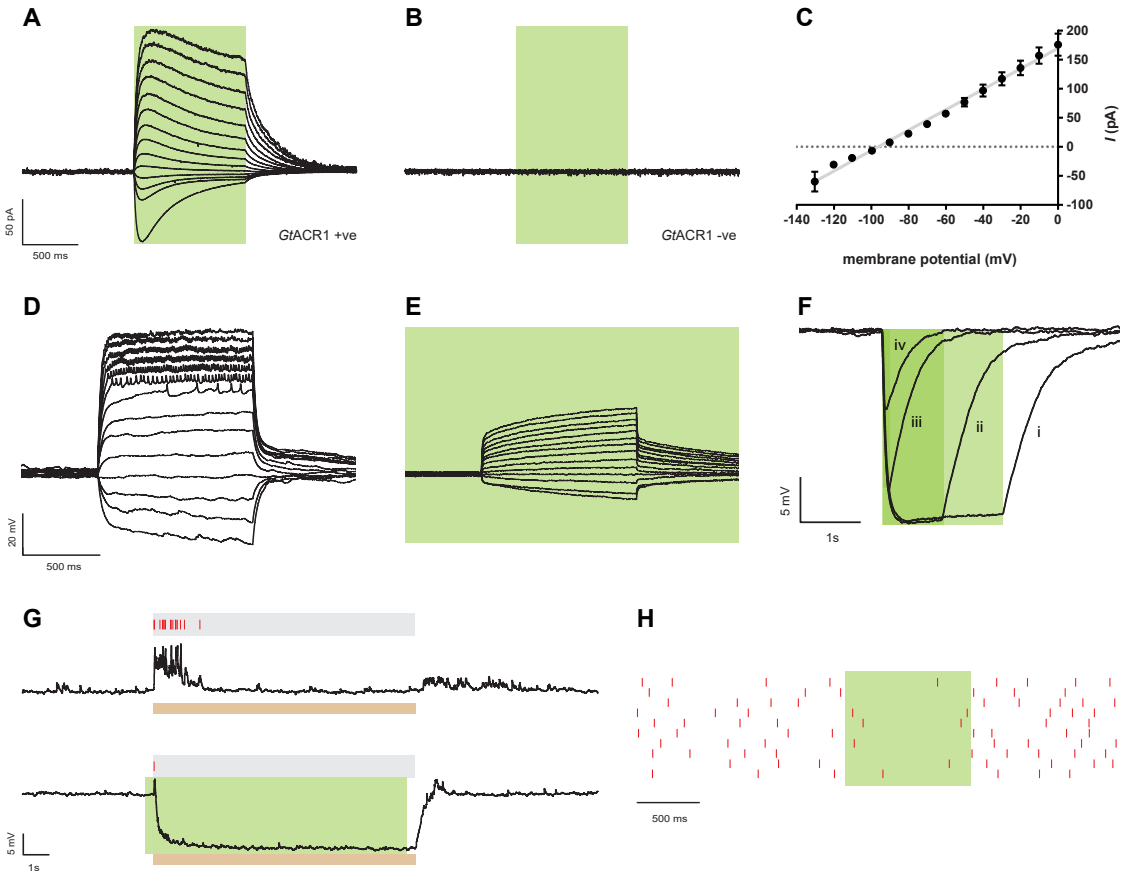


Fig. 11: Optogenetic silencing of $\alpha\beta_c$ KCs using *Gt*ACR1.
A. Current recordings to 10 mV voltage steps from -130 to 0 mV under a 1s pulse of green light (1 mW mm^{-2}) revealed strong *Gt*ACR1-mediated photocurrents ($\boldsymbol{n}$=2). **B.** Light-induced currents were not observed in *Gt*ACR1-negative cells ($\boldsymbol{n}$=2). **C.** Photocurrents were plotted against voltage steps to show the linear *I-V* relationship. The reversal potential ($\boldsymbol{I = 0}$) of *Gt*ACR1 was estimated to be -96 mV. **D.** Voltage recordings to 1s steps of depolarising current (5 pA) from -15 to 50 pA showed spiking activity, which was completely suppressed by green photostimulation at 0.25 mW mm^{-2} (**E**). Pre-pulse potential: -54 $\pm$ 2 mV. **F.** In current clamp, membrane potential was hyperpolarised by pulses of green light (0.25 mW mm^{-2}) — 2s (**i**), 1s (**ii**), 100 ms (**iii**), or 25 ms (**iv**) in duration. The maximum amplitude of decrease was $\sim$21 mV for 1s and 2s pulses. **G.** An 'up' $\boldsymbol{\alpha\beta_c}$ KC responded to a 10s pulse of MCH (brown) at odour onset, showing bursts of spikes (red ticks) before adaptation back to baseline. Green light (0.08 mW mm^{-2}) switched on $\sim$300 ms before odour onset inhibited this odour response, depressing the membrane potential by $\sim$12 mV. **H.** Spike raster of MBON-$\boldsymbol{\alpha}$2sc ($\boldsymbol{n}$=1). Silencing the upstream *Gt*ACR1-positive $\boldsymbol{\alpha\beta_c}$ KCs with a 1s pulse of green light (1.25 mW mm^{-2}) suppressed spiking.

a 10s odour pulse with bursts of spikes before falling back onto a baseline potential – a fast-adapting waveform typical of KC responses (**Fig.11G**, upper panel). This odour response could be suppressed by green light that switched on approximately 300 ms before odour onset, even at low light intensities (0.08 mW mm^{-2}) that only caused a depression of ∼12 mV (**Fig.11G**, lower panel).

Recent reports have documented that ACR activation caused neurotransmitter release (Messier et al., 2018) and even antidromic spikes (Mahn et al., 2018; Malyshev et al., 2017), possibly attributable to the excitatory chloride reversal potential in the axonal compartment (Mahn et al., 2018; Messier et al., 2018). Since these attenuated, antidromic spikes typically occurred within milliseconds after light onset (Mahn et al., 2018), this effect would probably not interfere with inhibition at the timescale of seconds. However, there was still a potential risk that light-evoked, *Gt*ACR1-mediated excitation at the axon might fire the KC-MBON synapses, which would defeat the purpose of the inhibition experiment. To test whether *Gt*ACR1-expressing $\boldsymbol{\alpha\beta_c}$ KCs activated downstream MBONs when illuminated, I recorded from MBON-$\boldsymbol{\alpha}$2sc (one per hemisphere), the immediate postsynaptic cell to $\boldsymbol{\alpha}$2 surface and core neurons (Aso et al., 2014a). No evidence was found to support MBON activation by light-induced currents; instead, spiking in MBON-$\boldsymbol{\alpha}$2sc was suppressed by a 1s pulse of green light (**Fig.11H**).

Taken together, I have validated the functionality of an inhibitory optogenetic tool by showing that it mediated strong photocurrents, reliably caused hyperpolarisations that suppressed odour responses, and silenced the activity of the downstream neuron.

3.3 Optogenetic activation of $\alpha\beta_c$ KCs during behaviour

Equipped with the novel optogenetic tools, I proceeded to utilise them for manipulating $\boldsymbol{\alpha\beta_c}$ KC activity and thus testing for those neurons' causal involvement in decision-making. Flies were trained to avoid a specific concentration (10 ppm) of MCH by pairing odour exposures with electric shock (Claridge-Chang et al., 2009; DasGupta et al., 2014; Groschner et al., 2018). During the task, animals had to discriminate the reinforced MCH concentration with a lower (1, 4, 5, 7, or 9 ppm) concentration of the same odour. The difficulty of discrimination was represented by the odour contrast at the interface between the two concentrations. Here, the fly decided whether to continue walking to the other half of the chamber, or to turn back. The time it spent in the empirically defined, central decision zone (where the odour interface lies) was its reaction time (DasGupta et al., 2014) (**Fig.6C**); the correct decision was to choose the lower concentration, given the flies' conditioned avoidance of the higher one. Since videos of the behaving flies were taken for the entirety of the testing period, they could be analysed to extract behavioural parameters, the most interesting of which were the reaction times and choice accuracies.

The chambers were designed with transparent floors and ceilings to enable optogenetic stimulation whenever the flies entered the decision zone. In the next few sections, I will focus on the activation experiment, which probed the consequences of increasing $\boldsymbol{\alpha\beta_c}$ KC activity during decision-making. I tested flies expressing the dendritically targeted Chrimson that I constructed, which was shown in patch-clamp recordings to effectively elicit small depolarisations (**Fig.10**). If the activity in these neurons causally contributed to the fly's decision, selective activation of 'up' or 'down' KCs would speed up the fly's reaction time. Unfortunately, these two subsets of KCs were genetically indiscriminate, resulting in ubiquitous Chrimson expression across both populations. Nonetheless, injection of small amplitudes of depolarising

current when the membrane potentials of one population are closer to spike threshold than those of the other, should, in theory, selectively activate 'up' or 'down' cells.

Chronometric and psychometric functions

This section examines in detail how the psychometric and chronometric functions changed when $\boldsymbol{\alpha\beta_c}$ KC activity was optogenetically activated during behaviour, in an 'up' or 'down' cell-selective, EPSC-injecting (using dendritically targeted Chrimson), or a non-selective, strongly depolarising (using untargeted Chrimson) manner. I hope to tackle the crux of this thesis: testing for a causal relationship between $\boldsymbol{\alpha\beta_c}$ KC activity and odour-guided decision-making behaviour.

Mean reaction times and accuracies from flies expressing *UAS-Chrimson::tdTom ::AMPAR-motif* (dendritically targeted) in $\boldsymbol{\alpha\beta_c}$ KCs were plotted as a function of task difficulty in chronometric (**Fig.12**, middle panel) and psychometric functions (**Fig.12**, right panel), respectively. Here, difficulty was represented as the log of the odour concentration ratio ([left] / [right]) to linearise the intervals. The two extremes ($\boldsymbol{x = -1}$ and $\boldsymbol{x = 1}$) represented the highest odour contrasts. In this unstimulated control condition, the mean reaction times increased non-linearly as the task became more difficult, from 0.674 $\pm$ 0.027s (mean $\pm$ s.e.m.) and 0.77 $\pm$ 0.028s at the easiest to 1.28 $\pm$ 0.044s and 1.53 $\pm$ 0.072s at the hardest difficulty (an approximately twofold increase), showing a characteristic dome shape in the chronometric function (Hanks et al., 2011; Stine et al., 2020). As expected, reaction times were generally more varied when the task was harder, since the signal-to-noise ratio was reduced when low drift rates were driven by ambiguous evidence (see **Methods** and the section **Drift-Diffusion Modelling of Reaction Time and Choice Accuracy**). Comparing the flies' performance between trials when the odour concentrations swapped sides (e.g., 1 vs 10 ppm and 10 vs 1 ppm), the reaction times were consistently higher when the high concentration was on the left

— this trend was generally observed across all stimulation conditions and genotypes. Since the behavioural chambers were structurally symmetrical, it was unclear why switching sides would matter. One explanation could be a miniscule discrepancy in flow rate between the two odour streams, leading to a slightly off-centre odour interface that was impossible to detect by the experimenter (there was no reliable way to visualise the interface). In any case, given that the points on the chronometric function were roughly symmetrical, the slight differences between sides should not significantly influence the subsequent analysis and modelling of reaction times.

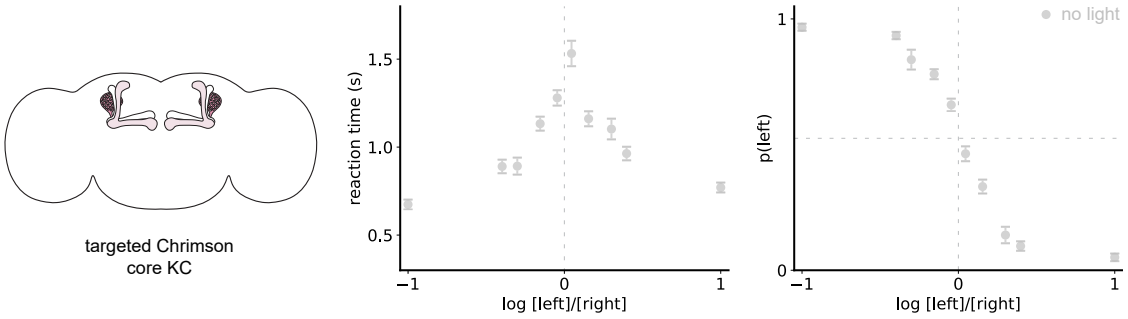


Fig. 12: Chronometric and psychometric functions.
Reaction times and choice accuracies plotted as a function of task difficulty, taken as log odour contrast. The easiest difficulties (1 vs 10 ppm and 10 vs 1 ppm) lie on the two extremes of the curves. Data from flies expressing dendritically targeted Chrimson, without light stimulation, are shown here. Middle: reaction times increased non-linearly with difficulty, yielding a dome-shaped chronometric function ($\boldsymbol{n}$=354–1084 reactions per difficulty). Right: accuracy is represented by the probability of choosing left. In the left half, the curve plots the fraction correct given 'left' is the correct choice; the right half is the inverse of accuracies given 'right' is correct ($\boldsymbol{n}$=32–122 flies per difficulty). Flies performed well at easy difficulties, reaching ∼95% accuracy. Performance approached chance level as task difficulty increased. Error bars: s.e.m.

The psychometric function described the flies' probability of choosing the left side as a function of difficulty (**Fig.12**, right panel). Another way of expressing this was that the left half represented choice accuracies (or fraction correct) given that 'left' was correct, whereas the right was the inverse of accuracies given 'right' was correct. In the unstimulated control condition, flies achieved a high level of performance, reaching ∼95% accuracy at the easiest difficulties. As the odour

contrast decreased, performance approached chance level. As expected, variances were larger when the task was more difficult, consistent with the augmented influence of noise when evidence was ambiguous.

To examine the effects of optogenetic activation of $\boldsymbol{\alpha\beta_c}$ KCs, mean reaction times and accuracies of illuminated flies were plotted on the same graph (**Fig.13A,B**). Error bars are not shown for the chronometric function, as full reaction time distributions will be displayed in the next section. For flies expressing dendritically targeted Chrimson (*UAS-Chrimson::tdTom::AMPAR-motif*), photostimulation with a single 25 ms pulse of low intensity (0.01 mW mm^{-2}) red light, triggered upon entry into the decision zone, lowered the chronometric function (**Fig.13A**, middle panel) — the mean reaction times were quickened. The effect of light appeared to be difficulty-dependent: a clear decrease in mean reaction times was evident only in difficult tasks. At high light intensity (0.2 mW mm^{-2}), the chronometric function was further depressed in a similarly difficulty-dependent manner: the reduction in speed even reached 0.33s (26%) and 0.38s (25%) at the lowest odour contrasts. The correlation between reaction time speedup and task difficulty was consistent with the idea that the DV was closer to threshold at low, and further away at high difficulties: equal depolarisations would have a more salient effect on the time taken to reach threshold in the latter case than the former. Whether or not these changes in mean reaction times are significant will be evaluated in the next section, together with an examination of the reaction time distributions.

Given a decrease in mean reaction times elicited by optogenetic activation, a concomitant decline in choice accuracies was expected, since the flies had less time to commit to a choice. Indeed, the slopes of psychometric functions in the two photostimulated conditions appeared to become less steep, albeit only slightly (**Fig.13A**, right panel). However, the maximal accuracies $\boldsymbol{P_{max}}$ at the easiest levels were unchanged at around 95%. This minimal influence of photostimulation on psychometry was reasonable because small, light-gated depolarisations transduced

by dendritically targeted Chrimson were not expected to cause such extreme deflections of the membrane potential to fire downstream neurons and directly impact behavioural choice. This manipulation appeared to only perturb the evidence integration step: flies were able to maintain their performance levels despite quickening their mean reaction times.

Flies expressing dendritically targeted Chrimson in $\boldsymbol{\alpha\beta_c}$ KCs only belonged to one of the two experimental genotypes. I compared them with flies expressing an untargeted version: the 32-aa motif from the cytoplasmic domain of murine neuroligin-1 (NLG1) was chosen since it failed to target Chrimson::tdTom to the somatodendritic compartment (**Fig.8D,I**) and was of comparable length with the AMPAR motif (39 aa). Since Chrimson expressed highly in the axons in this genotype, red light illumination would, in principle, strongly fire the whole $\boldsymbol{\alpha\beta_c}$ KC population (both 'up' and 'down'), and thus downstream MBONs as well, regardless of task difficulty. Consequently, if neural activity in $\boldsymbol{\alpha\beta_c}$ KCs was indeed causal to olfactory decision-making, the prediction was that the chronometric function would flatten as result of the decoupling between reaction time and difficulty changes. Concurrent flattening of the psychometric function, approaching chance level, would also be expected, since bulk activation of both the 'up' and 'down' populations would interfere with the race between evidence integrators.

Indeed, when flies expressed this untargeted version of Chrimson, photostimulation exerted a greater effect on both mean reaction times and mean choice accuracies (**Fig.13B**). The drop in reaction times was less apparent at low, but very drastic at high light intensity: at 7 vs 10 ppm, 9 vs 10 ppm, 10 vs 9 ppm, and 10 vs 7 ppm for example, mean reaction times were reduced by 0.28s, 0.37s, 0.34s, and 0.3s, which equated to 26%, 30%, 23%, and 25%, respectively. Again, these changes in mean reaction times will be statistically analysed together with an examination of reaction time distributions in the next section. Overall, a flattening of the chronometric function was observed, as predicted. Nonetheless, the curve was

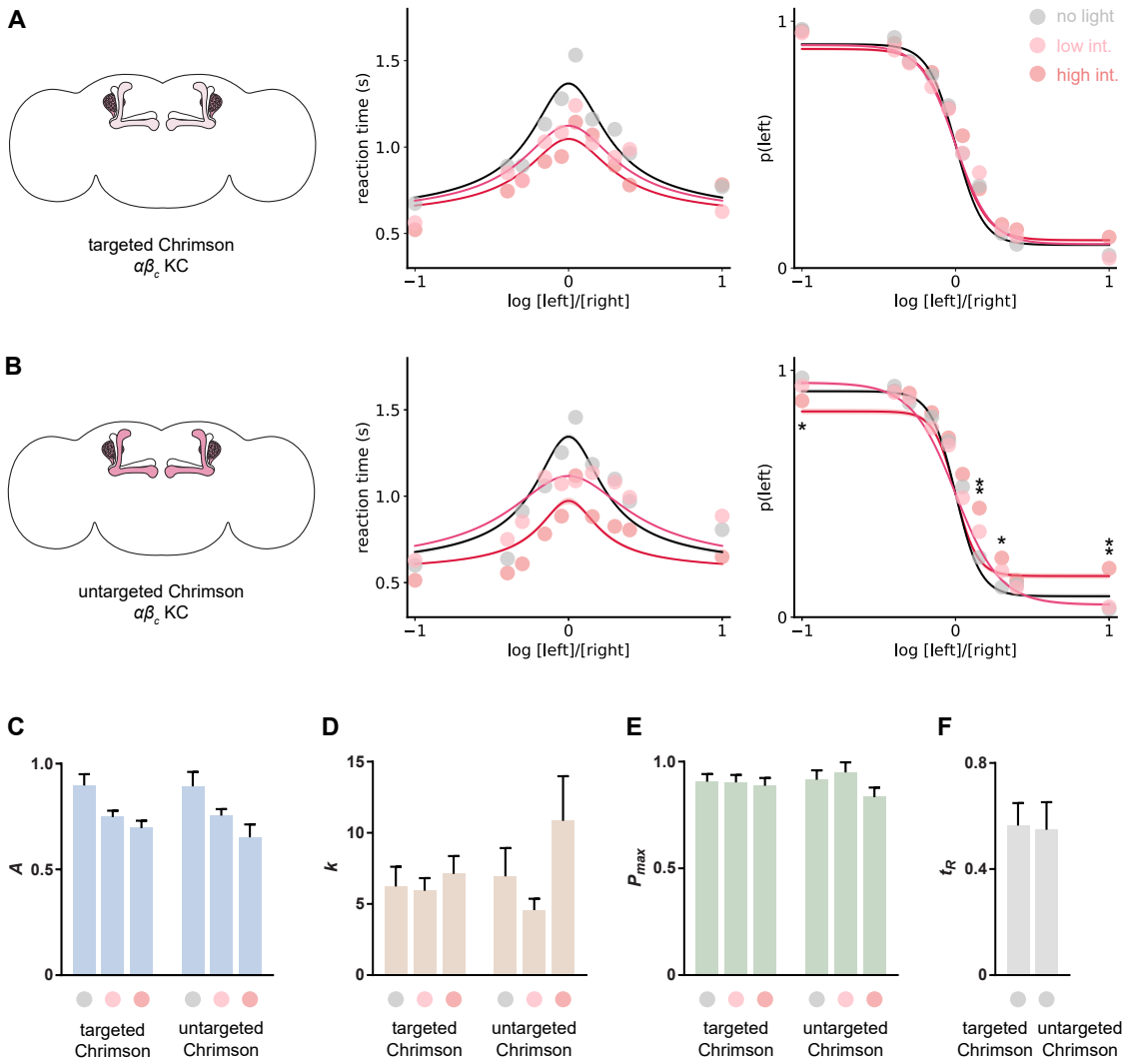


Fig. 13: Reaction time and choice accuracy data from experimental groups. **A.** Data from flies expressing dendritically targeted Chrimson in $\boldsymbol{\alpha\beta_c}$ KCs. Mean reaction times and accuracies from the weakly (0.01 mW mm^{-2}, pink points) and strongly (0.2 mW mm^{-2}, red points) photostimulated conditions are plotted on the same graph as **Fig.12**. Error bars not shown. Middle: optogenetic activation of $\boldsymbol{\alpha\beta_c}$ KCs by injecting small, EPSC-like currents to the dendrites quickened mean reaction times in a difficulty-dependent manner. The effect was more pronounced with increased light intensity. Low intensity: $\boldsymbol{n}$=350–674; high intensity: $\boldsymbol{n}$=326–530 reactions per difficulty. Right: Photostimulation did not appear to influence the psychometric function. Low intensity: $\boldsymbol{n}$=29–86; high intensity: $\boldsymbol{n}$=38–60 flies per difficulty. **B.** Data from flies expressing untargeted Chrimson (*UAS-Chrimson::tdTom::NLG1-motif*). Middle: compared with **A**, photostimulation further depressed mean reaction times, flattening the chronometric function. Unstimulated: $\boldsymbol{n}$=376–655; low intensity: $\boldsymbol{n}$=388–710; high intensity: $\boldsymbol{n}$=182–394 reactions per difficulty. Right: at high light intensity, the psychometric curve flattened (one-way ANOVA; 1 vs 10 ppm: * $\boldsymbol{p = 0.028}$; 10 vs 7: ** $\boldsymbol{p = 0.002}$; 10 vs 5: * $\boldsymbol{p = 0.013}$; 10 vs 1: ** $\boldsymbol{p = 0.028}$). Unstimulated: $\boldsymbol{n}$=37–64; low intensity: $\boldsymbol{n}$=42–62; high intensity: $\boldsymbol{n}$=31–70 flies per difficulty. For both genotypes in **A** and **B**, a drift-diffusion model was fit to the behavioural data (black, pink, and red lines) by varying three or four free parameters. **C-F.** (Continued on the next page)

not completely flat, implying that changes in difficulty were not entirely decoupled from mean reaction times. Meanwhile, the psychometric function at high light intensity was compressed (**Fig.13B**, right panel): the probability of choosing left at the two extremes approached 0.5, which meant that flies became more inaccurate even when the task was easy. The maximal accuracy $\boldsymbol{P_{max}}$ significantly dropped from 97% to 87% (1 vs 10 ppm) ($\boldsymbol{p = 0.028}$, one-way ANOVA) and from 96% to 80% (10 vs 1 ppm) ($\boldsymbol{p = 0.002}$). Significant changes at 10 vs 7 and 10 vs 5 ppm were also observed ($\boldsymbol{p = 0.002}$ and $\boldsymbol{p = 0.013}$, respectively).

Despite the prominent photostimulated effects on reaction time and accuracy, it was unclear whether the animals were visually reacting to the red light itself. I utilised two genotypes as control groups: flies expressing targeted Chrimson in $\boldsymbol{\alpha'\beta'}$ KCs, using the driver *VT030604-GAL4* (Kvon et al., 2014), and those solely expressing the $\boldsymbol{\alpha\beta_c}$ KC driver *NP6024-GAL4*. The former was considered a control since the biophysically dissimilar $\boldsymbol{\alpha'\beta'}$ KCs were poor sequential integrators of information, uninvolved in the evidence accumulation step in odour-guided decision-making (Groschner et al., 2018). In theory, increasing their activity during the task should not affect the speed at which decisions were committed. The latter was treated as the no-Chrimson control.

Fig. 13: (Continued from the previous page) Changes in parameters are described in this order: unstimulated; weakly photostimulated; strongly photostimulated. Error bar: s.e. **C.** The bound height A decreased with increasing light intensity for both genotypes. Targeted Chrimson: A dropped from 0.90 ± 0.054 to 0.75 ± 0.03, then to 0.70 ± 0.035. Untargeted Chrimson: A dropped from 0.89 ± 0.069 to 0.75 ± 0.032, then to 0.65 ± 0.061. **D.** Photostimulation exerted no conclusive effects on the sensitivity coefficient k. Targeted Chrimson: 6.24 ± 1.39; 5.93 ± 0.88; 7.12 ± 1.24. Untargeted Chrimson: 6.94 ± 1.99; 4.57 ± 0.79; 10.83 ± 3.15. **E.** Targeted Chrimson: $\boldsymbol{P_{max}}$ was unaffected by optogenetic activation, maintained at ∼0.9 (0.91 ± 0.04; 0.90 ± 0.04; 0.89 ± 0.04). For flies expressing untargeted Chrimson, the model captured the reduction in maximal accuracy at high light intensity: 0.92 ± 0.04; 0.95 ± 0.05; 0.83 ± 0.05. **F.** $\boldsymbol{t_R}$ was estimated for the unstimulated condition (targeted: 0.56 ± 0.08s; untargeted: 0.55 ± 0.10s); the value for each genotype was then taken as a constant in the model fits for photostimulated flies.

In the $\boldsymbol{\alpha'\beta'}$ KC control, reaction time data were more variable (**Fig.14A**, middle panel). Means of the reaction times might differ between unstimulated and lowly photostimulated conditions, but the overall contours of the two chronometric functions were similar. Although the psychometric functions were much shallower than those in the $\boldsymbol{\alpha\beta_c}$ KC experimental groups (maximal accuracies of only ∼90%), possibly reflecting genotype-specific discrepancies in associative learning, the mean accuracies between light conditions were unchanged across all difficulty levels (**Fig.14A**, right panel). Similarly, in the no-Chrimson, $\boldsymbol{\alpha\beta_c}$ KC driver control, the chronometric and psychometric functions in unstimulated and photostimulated conditions were virtually congruent, despite a significant change at 5 vs 10 ppm (Welch's *t*-test, $\boldsymbol{p = 0.02}$). Subsequent analyses with data modelling will further consolidate this notion. The effects of light on mean reaction times will be statistically analysed in the next section. Meanwhile, the near-overlap between the psychometric functions implied that light alone did not influence choice accuracies. Photostimulated effects on the chronometric and psychometric functions were due to the optogenetic activation of $\boldsymbol{\alpha\beta_c}$ KCs during behaviour.

Optogenetic activation quickened mean reaction times

Reaction times for pairs of reciprocal difficulties (e.g., 1 vs 10 ppm and 10 vs 1 ppm) were pooled. In all conditions, the distributions exhibited positive skew across difficulty levels (**Fig.15A**), a distinguishing feature of information accumulation to threshold (Gold and Shadlen, 2007; Ratcliff et al., 2016; Roitman and Shadlen, 2002). The origin of this asymmetry can be explained by the drift diffusion model (see **Introduction**, **Methods**, and next section): equal differences in drift rate generate unequal differences in reaction time (which has a minimum but no maximum) at the intersection with the decision bound. Therefore, as drift rates became lower with increasing evidence ambiguity, the tails of the distributions spread out,

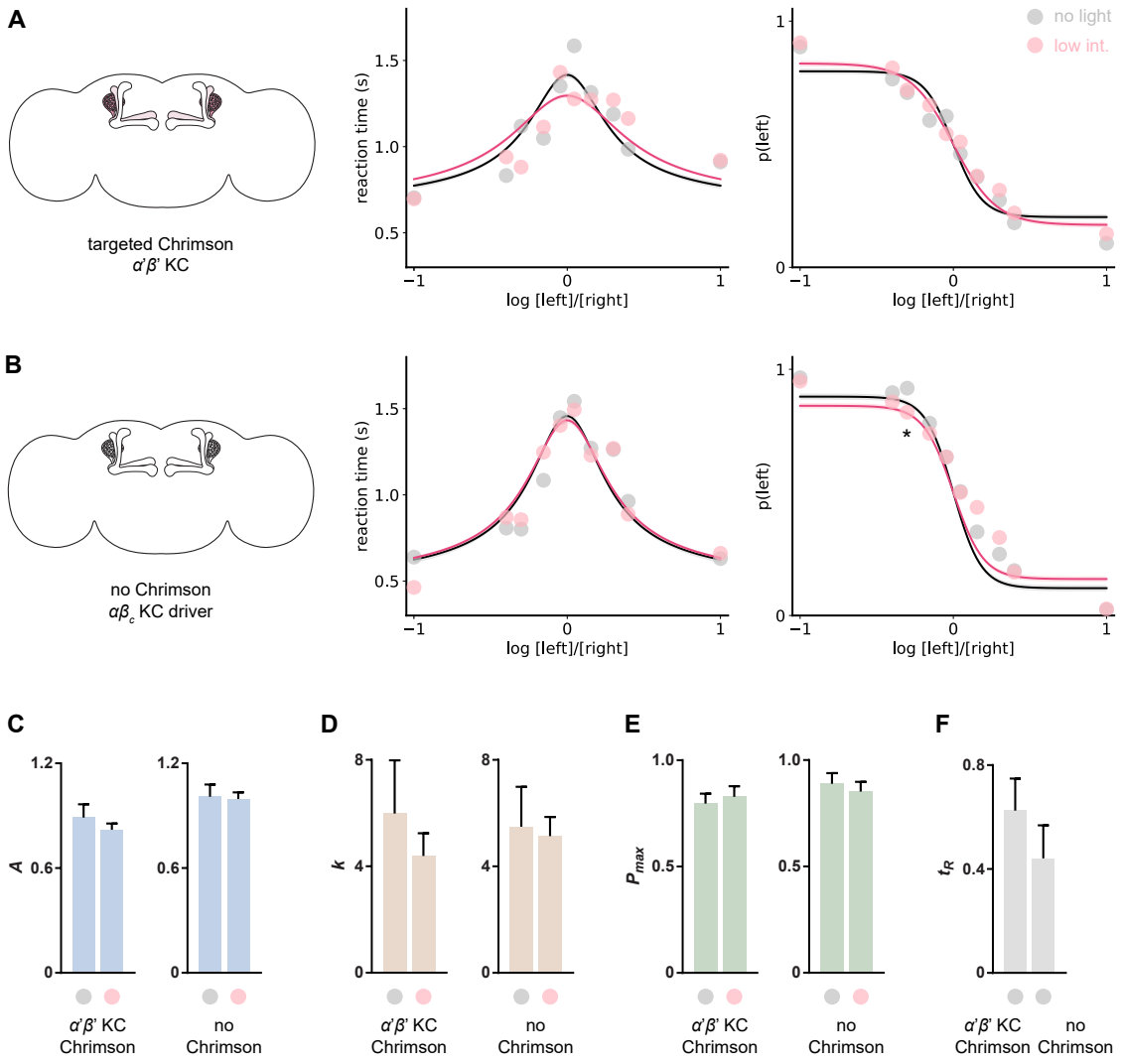


Fig. 14: Reaction time and choice accuracy data from control groups. Mean reaction times and choice accuracies in the unstimulated and photostimulated conditions are plotted as a function of difficulty, then fit with a drift-diffusion model (black and pink lines), as in **Fig.13**. **A.** Data from flies expressing dendritically targeted Chrimson in $\boldsymbol{\alpha'\beta'}$ KCs. Middle: chronometric functions for both the unstimulated and weakly photostimulated (0.01 mW mm^{-2}) conditions appeared more compressed than those of the experimental groups. Although differences in mean reaction times between the two conditions were observed at several difficulty levels, the overall contours of the chronometric functions were similar. Unstimulated: $\boldsymbol{n}$=296–600; low intensity: $\boldsymbol{n}$=197–444 reactions per difficulty. Right: psychometric functions for both conditions were shallow — maximal accuracies were only ∼90%. Optogenetic activation of $\boldsymbol{\alpha'\beta'}$ KCs did not seem to influence choice accuracy. Unstimulated: $\boldsymbol{n}$=48–107; low intensity: $\boldsymbol{n}$=33–72 flies per difficulty. **B.** Data from flies expressing the $\boldsymbol{\alpha\beta_c}$ KC driver, without Chrimson. Middle: reaction times were not affected by photostimulation; drift-diffusion fits were nearly overlapping. Unstimulated: $\boldsymbol{n}$=202–403; low intensity: $\boldsymbol{n}$=151–429 reactions per difficulty. Right: despite the significant reduction of accuracy only at 5 vs 10 ppm (Welch's t-test, * $\boldsymbol{p = 0.02}$), photostimulation on the whole exerted little effect on the shape of the psychometric function. Unstimulated: $\boldsymbol{n}$=30–48; low intensity: $\boldsymbol{n}$=22–54 flies per difficulty. **C-F.** (Continued on the next page)

corresponding to a larger number of slow responses, while the leading edge barely changed (**Fig.15A**). In contrast, transit times computed from off-centre nondecision zones displayed nearly symmetrical distributions and did not vary with task difficulty (**Fig.15B**). The mean transit times for all conditions were around 1.1–1.3s.

Photostimulation shifted reaction time distributions to the left (**Fig.15A i-iv**, upper panels), reflecting the decreases in mean reaction times (**Fig.13A,B**). For flies expressing dendritically targeted Chrimson, mean reaction times were significantly reduced when flies were weakly or strongly photostimulated (one-way ANOVA), but the effect was generally more prominent at high intensity. These decreases were difficulty-dependent, most significant when the task was hard (the sizeable reduction seen at the easiest difficulty and low light intensity was somewhat anomalous). These trends were also observed when flies expressed untargeted Chrimson. The quickening of mean reaction times was more drastic, especially when light intensity was high (one-way ANOVA). In contrast, photostimulation barely skewed the distributions of transit times (**Fig.15B i-iv**). However, it was surprising that the mean transit times statistically differed between unstimulated and photostimulated conditions for some difficulty levels, despite the values fluctuating only between 1.1–1.3s. A likely explanation was that the sample sizes were large, with small variances, such that tiny deviations of the mean still produced statistical significance. A more careful analysis of transit times revealed that they were indeed difficulty-independent, across the full spectrum of odour contrasts (**Fig.16A,B**, middle panels). In

Fig. 14: (Continued from the previous page) Changes in parameters are described in this order: unstimulated; weakly photostimulated. Error bar: s.e. For both of the control genotypes, optogenetic activation did not seem to exert significant effects on the bound height A, sensitivity k, and maximal accuracy $\boldsymbol{P_{max}}$. **C.** Model estimation of A. $\boldsymbol{\alpha'\beta'}$ KC control: 0.89 ± 0.08; 0.82 ± 0.04. No-Chrimson control: 1.01 ± 0.07; 1.00 ± 0.04. **D.** Model estimation of k. $\boldsymbol{\alpha'\beta'}$ KC control: 5.99 ± 1.99; 4.39 ± 0.86. No-Chrimson control: 5.49 ± 1.50; 5.14 ± 0.72. **E.** Model estimation of $\boldsymbol{P_{max}}$. $\boldsymbol{\alpha'\beta'}$ KC control: 0.80 ± 0.05; 0.83 ± 0.05. No-Chrimson control: 0.89 ± 0.05; 0.85 ± 0.05. **F.** $\boldsymbol{t_R}$ was longer in the $\boldsymbol{\alpha'\beta'}$ KC control (0.63 ± 0.12s) compared with the no-Chrimson control (0.44 ± 0.13s).

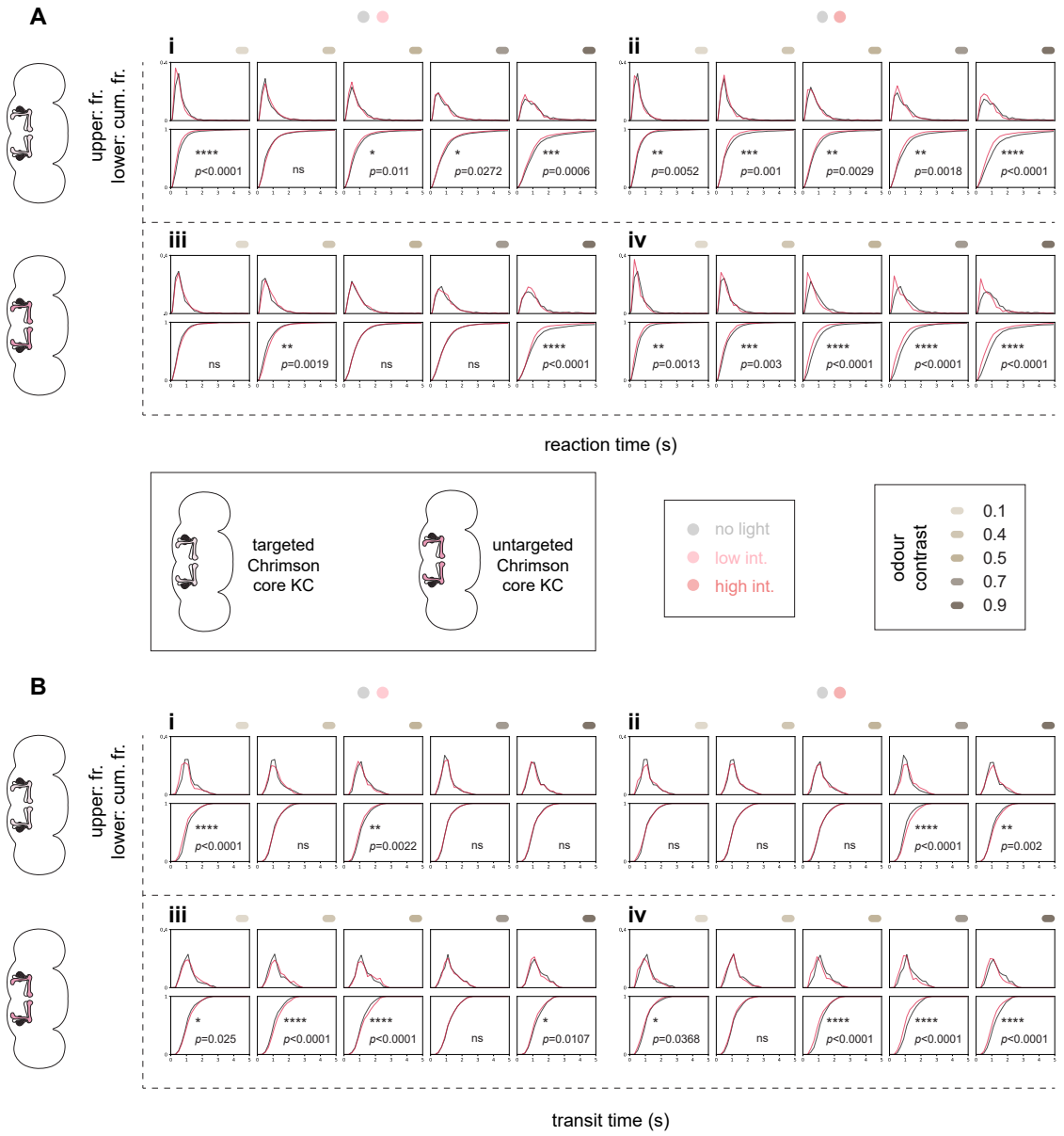


Fig. 15: Reaction and transit time distributions from experimental groups. **A.** Comparison of reaction time distributions and cumulative distributions for flies expressing dendritically targeted (**i, ii**) or untargeted (**iii, iv**) Chrimson between unstimulated (black line) and weakly (0.01 mW mm^{-2}; **i, iii**, red line) or strongly (0.2 mW mm^{-2}; **ii, iv**, red line) photostimulated conditions. Across all conditions and difficulty levels, the distributions exhibited positive skew. Photostimulation shifted these distributions to the left, reflecting decreases in mean reaction times. For each of the odour contrasts, mean reaction times from both genotypes were reduced by light (one-way ANOVA, *p*-values shown in figure), more prominently at high difficulties. **B.** Same convention as **A**, but with transit times. The distributions approximated normality. Across odour contrasts, mean transit times, which remained within the range 1.1-1.3s, were compared between unstimulated and photostimulated conditions (one-way ANOVA, *p*-values reported in figure). ns: not significant.

flies expressing targeted Chrimson, the mean percentage change in transit times, compared with the unstimulated condition, centred around zero (<4%) (**Fig.16A**, right panel). This was also observed when flies expressed untargeted Chrimson, under low intensity photostimulation (**Fig.16B**, right panel). However, when light intensity was high, transit times appeared to quicken by, on average, 9%. It was unclear why red light precipitated an effect in walking speed in this genotype, but this should not affect the analysis of reaction times, given their normalisation to entry velocities into the decision zone.

For control genotypes, photostimulation had a minimal effect on mean reaction times (**Fig.17**). As before, reaction times for the same odour contrasts (e.g., 1 vs 10 ppm and 10 vs 1 ppm) were pooled. Their distributions were positively skewed, as with those for the experimental genotypes. For flies expressing dendritically targeted Chrimson in $\boldsymbol{\alpha'\beta'}$ KCs, mean reaction times were unchanged by low intensity photostimulation at all difficulties except when the odour contrast was 0.4, a slight increase was observed (Welch's t-test, $\boldsymbol{p = 0.00206}$) (**Fig.17i**). For flies solely expressing the $\boldsymbol{\alpha\beta_c}$ KC driver, photostimulation had no effect on mean reaction times (**Fig.17iii**). Meanwhile, the transit time distributions were symmetrical, and mean transit times were generally unaffected by low intensity photostimulation, except for two anomalous cases (**Fig.17ii,iv**).

Overall, in conclusion of the last two sections, changes in reaction time and choice accuracy in different stimulation conditions when flies expressed dendritically targeted and untargeted Chrimson (compared with the controls) provided compelling evidence that 1) optogenetically increasing $\boldsymbol{\alpha\beta_c}$ KC activity led to quicker decisions but poorer accuracy in a graded manner dependent on light intensity, and that 2) a difference in Chrimson localisation could tailor the activation paradigm to precipitate different effects on behavioural parameters. The analysis of such evidence will be made more rigorous with drift-diffusion modelling in the subsequent section.

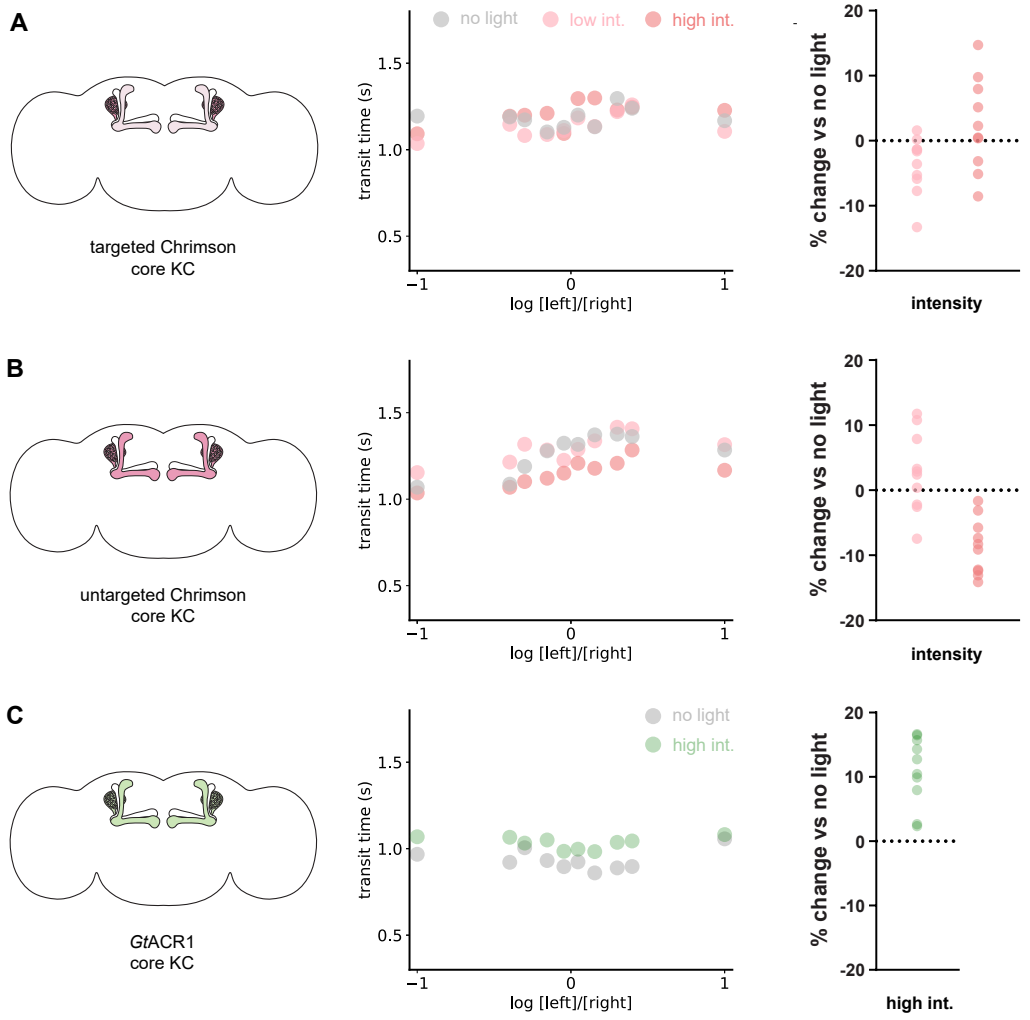


Fig. 16: Analysis of transit times across task difficulties.
Transit times were plotted as a function of task difficulty, given as log odour contrast, as with **Fig.13, 14**. **A.** Middle: for flies expressing dendritically targeted Chrimson, transit times did not vary with difficulty, across all three photostimulation conditions. Right: compared with the unstimulated control, the average changes in transit times across difficulties were -3.8% and 2.4% for low and high light intensities, respectively. **B.** Same convention as **A**, but for flies expressing untargeted Chrimson. Middle: transit times were difficulty-independent. Right: average changes were 2.7% and -8.7% for low and high light intensities, respectively. **C.** Transit times from flies expressing *Gt*ACR1 in $\boldsymbol{\alpha\beta_c}$ KCs. Middle: unstimulated flies (on average, transit time = 0.93s) appeared to walk slightly faster than photostimulated ones (average = 1.03s). Right: average change in transit time during green light stimulation was 10.9%.

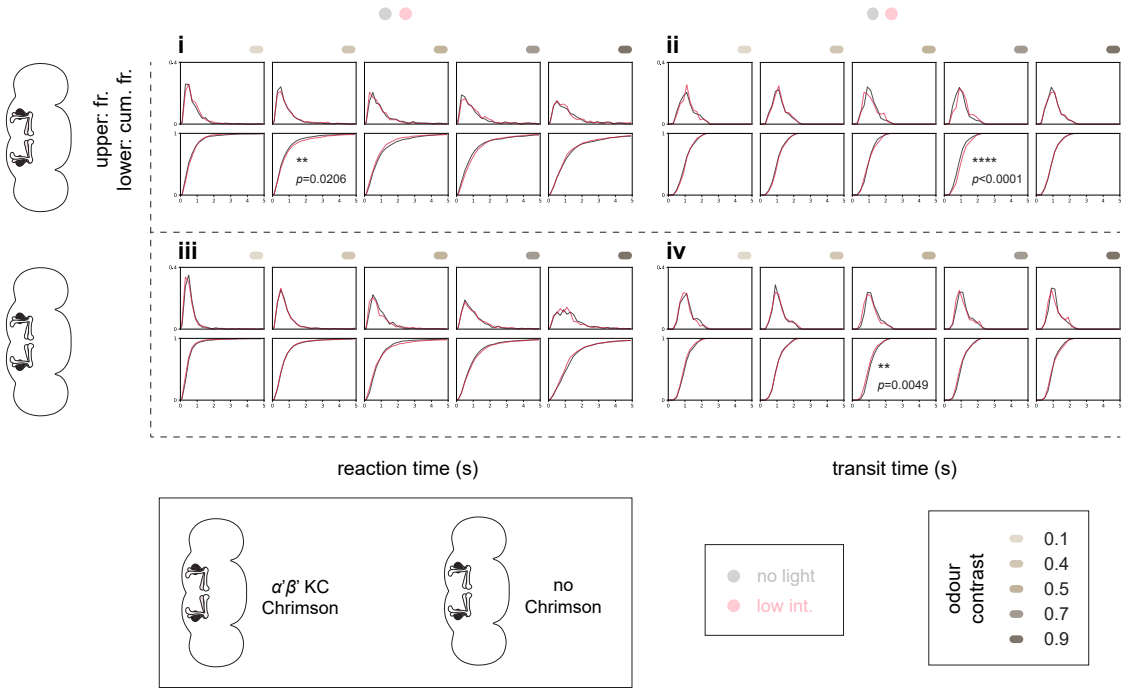


Fig. 17: Reaction and transit time distributions from control groups. Comparison of reaction (**i, iii**) and transit time (**ii, iv**) distributions and cumulative distributions for control flies expressing dendritically targeted Chrimson in $\boldsymbol{\alpha'\beta'}$ KCs (**i, ii**) or without Chrimson (**iii, iv**) between unstimulated (black line) and weakly photostimulated (0.01 mW mm^{-2}; red line) conditions. Across all conditions and difficulty levels, reaction time distributions exhibited positive skew, whereas those of transit times did not. For the $\boldsymbol{\alpha'\beta'}$ KC control, photostimulation did not significantly alter reaction times, except at odour contrast = 0.4 (unpaired t test with Welch's correction, **i**). Transit times: photostimulation elicited significant changes only in two cases (**ii, iv**). p-values shown in figure.

Drift-diffusion modelling of reaction time and choice accuracy

To mathematically formalise the effects of optogenetic activation on reaction time and choice accuracy, I fit the data with drift-diffusion models of evidence accumulation. These models assume integration of noisy sensory evidence to decision threshold (see **Introduction**) (Bogacz et al., 2006), and simple analytical expressions (Eq. (5) and (6.2), see **Methods**) relate choice accuracy and reaction time to task difficulty $\boldsymbol{x}$, bound height $\boldsymbol{A}$, drift rate $\boldsymbol{\mu} = \boldsymbol{kx}$ where $\boldsymbol{k}$ is the

sensitivity coefficient, residual time $\boldsymbol{t_R}$, and maximal accuracy $\boldsymbol{P_{max}}$ (see **Methods**), providing excellent fits to chronometric and psychometric data (DasGupta et al., 2014; Groschner et al., 2018; Palmer et al., 2005; Roitman and Shadlen, 2002). The model also accounts for the empirically observed, difficulty-dependent trend in the skewed reaction time distributions (Ratcliff et al., 2016). At high difficulty, evidence remains ambiguous: the decision variable evolves with lower mean drift rates but fixed noise, stretching the long tail in the distributions, i.e., reaction times become more variable (**Fig.12**). Another advantage of fitting suitable models to data is that it offers the experimenter a more comprehensive outline of the underlying generating functions, giving less weight to the variability of individual data points.

Two similar models were considered. In Model 1, $\boldsymbol{P_{max}}$ was empirically determined (DasGupta et al., 2014; Groschner et al., 2018). Here, it was computed as the average of the accuracies at 1 vs 10 ppm and 10 vs 1 ppm. Model 2 had one important difference in that $\boldsymbol{P_{max}}$ was treated as a free parameter. Given that high intensity optogenetic activation compressed the psychometric function — reducing the maximal accuracy $\boldsymbol{P_{max}}$ — in flies expressing non-dendritically targeted Chrimson (**Fig.13B**, right panel), Model 2 would capture this reduction in its fit and thus better describe the effect of light on choice accuracy. However, the extra parameter in Model 2 risked overfitting to noise. To compare the models, 5-fold cross-validation was performed (**Fig.18C**), and model predictions were plotted against test data for both experimental genotypes (**Fig.18A,B**). If Model 2 suffered from overfitting, it would generate greatly variable cross-validated fits, some of which would fail to predict the test data. What was observed was that for both models, the cross-validated fits provided satisfying predictions of chronometric and psychometric functions: the $\boldsymbol{R^2}$ of model versus test data was highly clustered and maintained at least at 0.5; for many psychometric predictions $\boldsymbol{R^2}$ even climbed to $>$0.95 (**Fig.18D**). This implied that the two models shared comparable fits without overfitting of the data. There were no distinguishable differences in $\boldsymbol{R^2}$ between the cross-validated fits of Models 1 and 2, using data from both genotypes

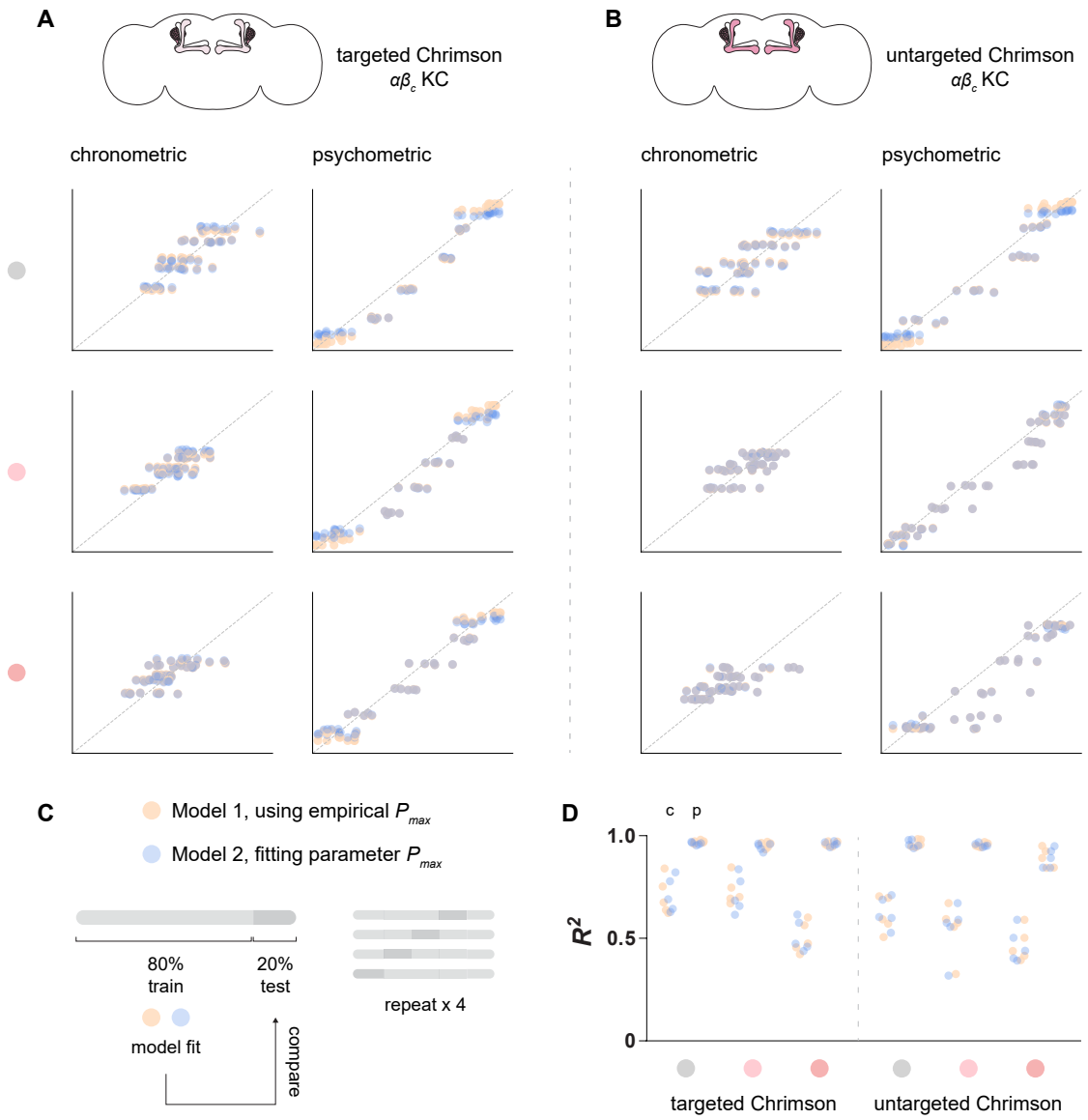


Fig. 18: 5-fold cross-validation of Models 1 and 2.
A. Data from flies expressing dendritically targeted Chrimson. The reaction times (chronometric, left) and accuracies (psychometric, right) predicted from 5-fold cross-validated model fits (y-axis) are plotted against test data (x-axis). Dashed line indicates perfect prediction. Peach dot: data point from Model 1 prediction; blue dot: from Model 2. Grey: unstimulated; light pink: weakly photostimulated (0.01 mW mm^{-2}); pink: strongly photostimulated (0.2 mW mm^{-2}). Across three light conditions, both models seemed to provide fairly satisfying predictions of reaction time and choice accuracy. **B.** Same convention as **A**, but for flies expressing untargeted Chrimson. **C.** The 5-fold cross-validation procedure. Model (1 or 2) fitting was first performed on 80% (training) of shuffled data to generate a set of estimated parameters, which were then used to predict the remaining 20% (test) of the dataset. This process was repeated four more times. See **Methods** for details. **D.** $\boldsymbol{R^2}$ quantified the goodness-of-fit of the model predictions. For both models, $\boldsymbol{R^2}$ generally was maintained at least at 0.5; the respective values were indistinguishable between models. c: chronometric; p: psychometric.

across three stimulation conditions. However, given that $\boldsymbol{R^2}$ was reported to be an inadequate measure of goodness-of-fit in nonlinear models (Spiess and Neumeyer, 2010), two additional approaches, namely, the extra sum-of-squares F test and Bayesian information criterion (BIC), were utilised to compare Models 1 and 2. The former examined the probability that the improvement in fit in the more complicated model could be explained by chance, whereas the latter was based on information theory, balancing the goodness-of-fit (sum-of-squares) and the number of free parameters (see **Methods**). The F ratios across photostimulation conditions in the two genotypes were shown in **Fig.19A**. Since none of the values were significantly greater than 1, random scatter was sufficient to explain the differences in the model fits. On the other hand, differences in BIC across the photostimulation conditions were plotted, given $\boldsymbol{\Delta}\text{BIC} = \text{BIC}_{\text{Model2}} - \text{BIC}_{\text{Model1}}$ (**Fig.19B**). Since lower BIC values were preferred, a positive $\boldsymbol{\Delta}$BIC indicated that the experimenter should in fact opt for Model 1. However, the small $\boldsymbol{\Delta}$BIC values across all conditions translated to only moderate evidence against Model 2. Keeping in mind that BIC was a rather conservative approach (compared to say, Aikake Information Criterion, AIC) that penalised more stringently the increase in parameter number, it was not surprising that Model 1 fared better under this criterion, given similar sum-of-squares between the two models. They described the data equally well, but since only Model 2 treated $\boldsymbol{P_{max}}$ — which could be experimentally modified by optogenetic activation — as a variable, it was chosen for subsequent analyses.

Reaction times and choice accuracies were simultaneously fit using drift-diffusion Model 2 to assess how photostimulation of $\boldsymbol{\alpha\beta_c}$ KCs during behaviour influenced the various parameters (**Fig.13**, black, pink, and red lines). The model fit would better describe the overall shapes of the chronometric and psychometric functions, making the analysis less susceptible to noisy individual points, for instance, in the control dataset where flies expressed targeted Chrimson in $\boldsymbol{\alpha'\beta'}$ KCs (**Fig.14A**). For simplicity, $\boldsymbol{t_R}$ from the fit to unstimulated data was taken and used as a constant for the photostimulated conditions, since residual times of the flies were not expected

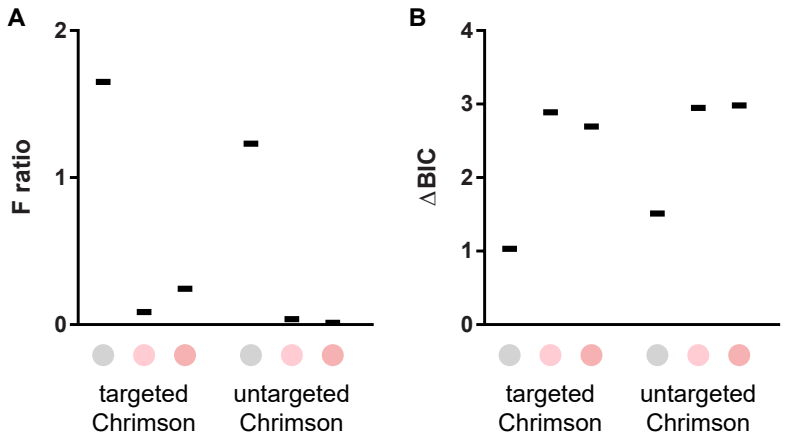


Fig. 19: Two additional approaches of model comparison. The extra sum-of-squares F test and Bayesian information criterion (BIC) were used to evaluate whether Model 1 or 2 provided significantly better fits to data. **A.** Since the F ratio across all conditions did not significantly exceed 1, random scatter sufficed to explain differences in model fits. See **Methods** for test details. **B.** $\boldsymbol{\Delta}\text{BIC} = \text{BIC}_{\text{Model2}} - \text{BIC}_{\text{Model1}}$. Lower BIC values were favoured, thus large, positive $\boldsymbol{\Delta}$BIC would support Model 1. $\boldsymbol{\Delta}$BIC values across all conditions <4, providing only moderate evidence against Model 2.

to fluctuate when $\boldsymbol{\alpha\beta_c}$ KCs were optogenetically activated. To better convey the intuition of how changing the bound height $\boldsymbol{A}$ and sensitivity coefficient $\boldsymbol{k}$ might alter the shapes of the chronometric and psychometric functions, **Fig.20** shows arbitrary cases of high or low parameters. Manipulating $\boldsymbol{A}$ changes the height of the chronometric peak, but has little effect on the psychometric curve — its slope only slightly steepens when $\boldsymbol{A}$ increases. Meanwhile, elevating $\boldsymbol{k}$ mainly renders the chronometric peak sharper and more pronounced without changing its amplitude. It does, however, considerably steepens the psychometric slope. It is apparent that changes in $\boldsymbol{A}$ and $\boldsymbol{k}$ induce antagonistic effects on the reaction time — a crucial tradeoff in the drift-diffusion model. Comparing the shapes of the model fits of actual data, in particular the chronometric functions, optogenetic activation appeared to primarily lower and widen the peaks, suggesting a reduction in $\boldsymbol{A}$.

Estimated parameters fit to data from different conditions were plotted side by

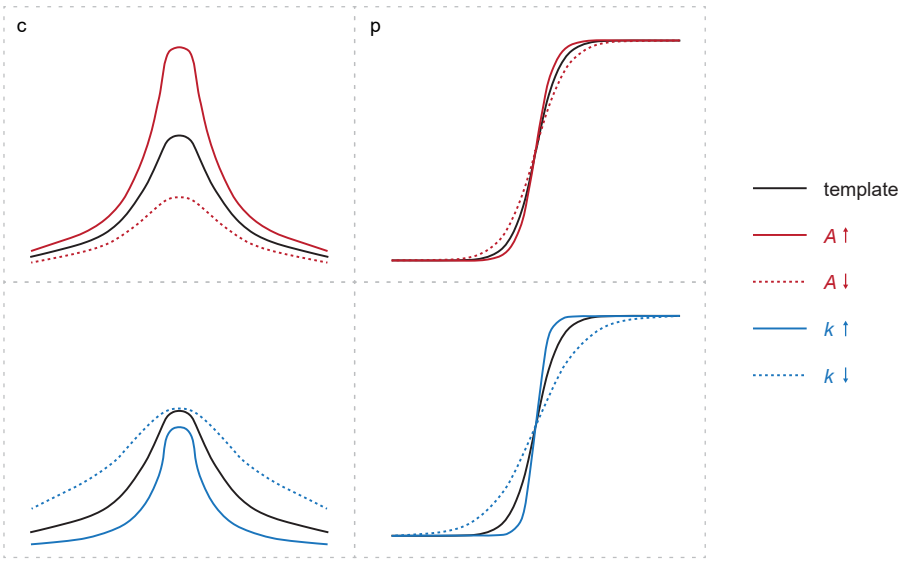


Fig. 20: The effects of changing *A* and *k*.
Simulation demonstrating how changing the values of A and k affects the shapes of the behavioural functions. Black line represents a template of arbitrary values of A and k. Increasing A stretches the peak of the chronometric curve vertically and slightly steepens the psychometric curve. Increasing k sharpens, but does not elongate, the chronometric peak; it similarly steepens the psychometric function, but to a larger extent. c: chronometric; p: psychometric. Red and blue lines indicate changes in the parameters; dashed lines when the parameter decreases. Simulated functions from Long Ding, 2017.

side (**Fig.13C-F**). Indeed, the bound height ***A*** decreased with increasing optogenetic activation (**Fig.13C**). When flies expressed dendritically targeted Chrimson, ***A*** was 0.90 ± 0.054 (mean ± s.e.) when unstimulated, dropped to 0.75 ± 0.03 at low light intensity stimulation, and was further reduced to 0.70 ± 0.035 when light intensity was high. Similarly, when untargeted Chrimson was expressed, ***A*** decreased from 0.89 ± 0.069 to 0.75 ± 0.032, and further to 0.65 ± 0.061 when flies were photostimulated with low and high light intensities, respectively. Surprisingly, these changes in the bound are similar for the two genotypes, failing to reflect differences in the severity of behavioural effects. On the other hand, the sensitivity coefficient ***k*** was unchanged by photostimulation, maintaining its value at ∼6 when Chrimson was targeted (**Fig.13D**). In contrast, ***k*** showed more variable changes when flies expressed untargeted Chrimson, decreasing from 6.94 ± 1.99 to

4.57 ± 0.79 when weakly photostimulated, but jumped up to 10.83 ± 3.15 when photostimulation was stronger; these changes, however, were inconclusive due to relatively large parameter uncertainties. Meanwhile, the maximal accuracy $\boldsymbol{P_{max}}$ was ∼0.9, unaffected by optogenetic activation in the targeted Chrimson genotype (**Fig.13E**). For flies expressing untargeted Chrimson, $\boldsymbol{P_{max}}$ exhibited a considerable reduction from 0.92 ± 0.045 to 0.83 ± 0.046, echoing the trend from the analysis of mean accuracies in the previous section. It was of note that there seemed a shortage of data points for easy task levels, e.g. between 1 vs 10 ppm and 4 vs 10 ppm, on the log scale, augmenting the uncertainty in the estimation of this parameter. Lastly, the residual times $\boldsymbol{t_R}$ were comparable at ∼0.55s for the two genotypes (**Fig.13F**).

Drift-diffusion model fits were also performed on data from the control groups (**Fig.14A,B**, black and pink lines). Flies expressing dendritically targeted Chrimson in $\boldsymbol{\alpha'\beta'}$ KCs had a slightly longer $\boldsymbol{t_R}$ of 0.63s (**Fig.14F**). The bound height $\boldsymbol{A}$ estimated from model fits showed a mild decrease from 0.89 ± 0.076 to 0.82 ± 0.037 (**Fig.14C**), and the scaling factor $\boldsymbol{k}$, from 5.99 ± 2 to 4.39 ± 0.86 (**Fig.14D**), although the standard errors of these parameters should be taken into account. $\boldsymbol{P_{max}}$ was rather low compared with the experimental genotypes, and remained unaffected by light at ∼0.8 (**Fig.14E**). Despite the variable data, it appeared that the model could extract underlying chronometric and psychometric functions and demonstrate that optogenetic activation of $\boldsymbol{\alpha'\beta'}$ KCs exerted no significant effects on the parameters. Similarly, for flies solely expressing *NP6024-GAL4*, photostimulation had virtually no influence: $\boldsymbol{A}$ remained at ∼1, $\boldsymbol{k}$ at ∼5, and $\boldsymbol{P_{max}}$ at ∼0.87 (**Fig.14C,D,E**). The residual time $\boldsymbol{t_R}$ was comparatively fast, at 0.44 (**Fig.14F**). Detailed scrutiny of the raw data suggested that the slight compression of the psychometric function was likely a result of two particular points, at 10 vs 7 and 10 vs 5 ppm, which displayed unusually low accuracies. Nonetheless, this was insufficient to produce statistically significant deviations in the model parameters. Overall, flies in the control groups seemed impervious to

photostimulation, suggesting that the light-induced changes in the experimental groups were genotype-specific.

Taken together, the most conclusive effects of optogenetic activation of $\boldsymbol{\alpha\beta_c}$ KCs, at low and high intensities, appeared to be a reduction of bound height $\boldsymbol{A}$. This was similar in amplitude regardless of Chrimson localisation. The scaling factor $\boldsymbol{k}$ showed more variability, although there was no significant change within each genotype. Based on these results, it will be interesting to consider how optogenetic activation translates to changes in the decision bound in a biological substrate — this will be further examined in **Discussion**.

Bayesian modelling of reaction time and choice accuracy

To complement the analysis in the previous section, a Bayesian drift-diffusion model was also fit to reaction time and choice accuracy data, using HDDM (Wiecki et al., 2013). An advantage of Bayesian models is that they estimate parameters, in this case, bound height $\boldsymbol{A}$, drift rate $\boldsymbol{\mu}$, and residual time $\boldsymbol{t_R}$, as posterior distributions rather than single, most likely values. In addition, these models are preferred in many instances because full reaction time distributions, instead of the mean values, are taken into account. Here, for each stimulation condition in the experimental genotypes, separate drift rates and bound heights were estimated for each difficulty level. As an example, **Fig.21E** shows the posterior densities of drift rates and bound heights at different odour contrasts, when flies expressing targeted Chrimson were unstimulated. The mean and uncertainty of each parameter value were plotted as a function of task difficulty (**Fig.21A,B**, left panels). Positive drift rates indicated that choosing left was the correct choice, while negative ones indicated the opposite. Consistent with the central idea that vague evidence in hard tasks contributed low drift rates, the Bayesian model fit also showed decreasing drift rates with

increasing difficulty levels. To test if the drift rates became more extreme under photostimulated conditions, their absolute values were taken and compared. For both genotypes (targeted and untargeted Chrimson), optogenetic activation exerted no significant difference (one-way ANOVA) (**Fig.21D**). To render this notion more rigorous, I examined how this analysis related to changes in the sensitivity coefficient $\boldsymbol{k}$. Interestingly, despite saturating at the two extremes ($\boldsymbol{x = -1}$ and $\boldsymbol{x = 1}$; lowest difficulties), the correlation between drift rate and task difficulty demonstrated linearity in the central range. This was encouraging, since one of the assumptions made in the previous drift-diffusion fits was the linear relationship $\boldsymbol{\mu' = kx}$, where $\boldsymbol{\mu}$' was the normalised drift rate, and $\boldsymbol{x}$ was the task difficulty (see **Methods**, Eq. (3)). Although the empirical relationship observed here was not strictly linear, I reasoned that taking the slope in the central linear range would approximate $\boldsymbol{k}$ (absolute values of the negative slopes were taken) (**Fig.21E**). For flies expressing dendritically targeted Chrimson, $\boldsymbol{|k|}$ appeared unchanged by low and high intensity photostimulation. Similarly, optogenetic activation did not conclusively alter $\boldsymbol{|k|}$ when untargeted Chrimson was expressed. These results were consistent with those from the last section (**Fig.13D**), strengthening the idea that optogenetic activation of $\boldsymbol{\alpha\beta_c}$ KCs quickened reaction times, but did not appear to modify the scaling factor $\boldsymbol{k}$.

On the contrary, means of the posterior distributions of bound heights did not vary with difficulty (**Fig.21A,B**, right panels). This was reasonable within the framework of the drift-diffusion model. Values for $\boldsymbol{A}$ across difficulty levels were grouped and compared between stimulation conditions. Photostimulation significantly lowered $\boldsymbol{A}$ when flies expressed targeted Chrimson ($\boldsymbol{p = 0.009}$ and $\boldsymbol{p < 0.001}$ for the two light intensities) (**Fig.21C**). When untargeted Chrimson was expressed instead, low intensity photostimulation failed to significantly alter $\boldsymbol{A}$ ($\boldsymbol{p = 0.6}$), while high intensity light did ($\boldsymbol{p = 0.002}$). Overall, it was apparent from the Bayesian model fit that optogenetic activation lowered the decision bound, recapitulating the results from last section.

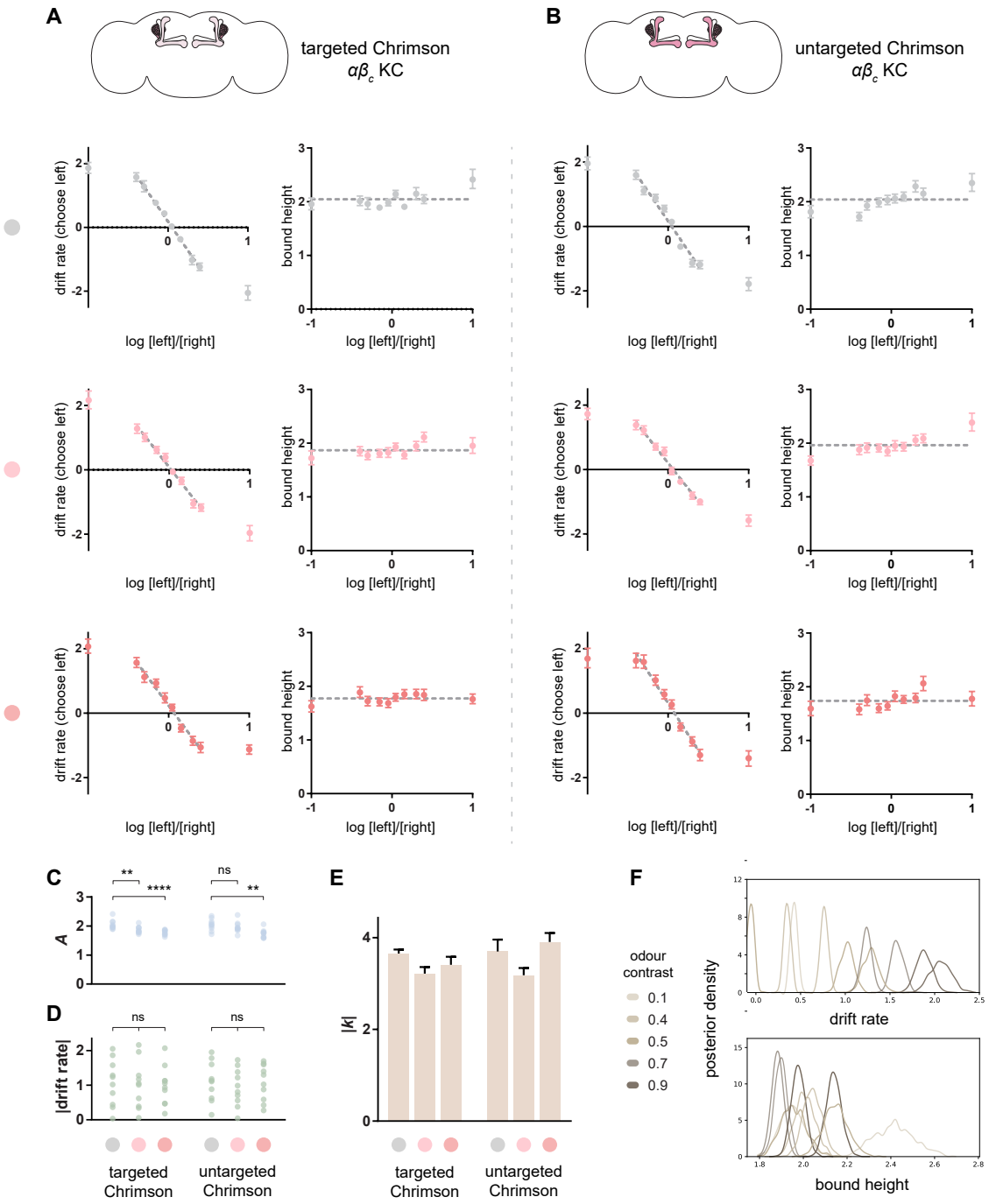


Fig. 21: Bayesian modelling of reaction time and choice accuracy.
Reaction time and choice accuracy data analysed by HDDM (Wiecki et al., 2013). **A.** For flies expressing dendritically targeted Chrimson, separate drift rates and bound heights were estimated for each difficulty level, and plotted as a function of log odour contrast (mean ± 95% C.I.). All three photostimulation conditions showed difficulty-dependence in drift rate. Left: the relationship was linear in the central range, excluding the two extremes (1 vs 10 ppm and 10 vs 1 ppm). Linear regression extracted the slope (dashed line) in this region, whose absolute value approximated the sensitivity coefficient k. (Continued on the next page)

Extrema detection

So far, the entirety of my data analysis rested upon the treatment of odour-guided decision-making as a process of evidence accumulation, based on the role of $\boldsymbol{\alpha\beta_c}$ KCs as temporal integrators of sensory information (Groschner et al., 2018). However, a recent study reported that in many cases, it was not straightforward to distinguish which behavioural observations corroborated an integration strategy, since non-integration models appeared to provide good fits for behavioural data as well (Stine et al., 2020). To test this idea, I analysed the reaction time and choice accuracy data with the extrema detection model, which only assumed sequential sampling, but not evidence integration (Stine et al., 2020). In this framework, momentary evidence is sampled sequentially from a stationary distribution until a sample exceeds one of the two decision bounds (an extremum), at which point a decision is committed based on the option favoured by that sample (**Fig.7**). The model estimates the parameters $\boldsymbol{k}$ — which relates the mean of the evidence distribution $\boldsymbol{\mu}$ and difficulty $\boldsymbol{x}$ in $\boldsymbol{\mu = kx}$ — as well as $\boldsymbol{A}$, $\boldsymbol{t_R}$, and $\boldsymbol{P_{max}}$.

Fig. 21: A. (Continued from the previous page) Right: bound heights were difficulty-independent; dashed lines represent the mean values. Grey: unstimulated; pink: weakly photostimulated (0.01 mW mm^{-2}); red: strongly photostimulated (0.2 mW mm^{-2}). **B.** Same convention as **A**, but for flies expressing untargeted Chrimson. **C.** Bound heights across difficulties were grouped and compared between conditions, described in this order: unstimulated; weakly photostimulated; strongly photostimulated. Untargeted Chrimson: A decreased from 2.05 ± 0.05 (mean ± s.e.m.) to 1.87 ± 0.04 (one-way ANOVA, ** $\boldsymbol{p = 0.009}$), then to 1.77 ± 0.03 (**** $\boldsymbol{p < 0.0001}$). Targeted Chrimson: A decreased from 2.04 ± 0.06 to 1.96 ± 0.06 ($\boldsymbol{p = 0.6}$), then to 1.74 ± 0.05 (** $\boldsymbol{p = 0.002}$). ns: not significant. **D.** Absolute values of drift rates across difficulties were grouped and compared, testing if they were more extreme in any photostimulated condition - there were no significant changes (one-way ANOVA). Untargeted Chrimson: 1.07 ± 0.21; 1.01 ± 0.22; 0.99 ± 0.18. Targeted Chrimson: 1.10 ± 0.18; 0.94 ± 0.17; 1.08 ± 0.17. **E.** Slopes of the linear regression ($|\boldsymbol{k}|$) did not appear to significantly differ between the three light conditions, for both genotypes. Error bar: s.e. Targeted Chrimson: 3.65 ± 0.09; 3.21 ± 0.15; 3.41 ± 0.18. Untargeted Chrimson: 3.70 ± 0.26; 3.18 ± 0.16; 3.90 ± 0.20. **F.** Example of the model estimation of posterior densities for drift rate and bound height across odour contrasts. Data from flies expressing dendritically targeted Chrimson.

Visually, the model fits did not appear to fully capture the shapes of the chronometric functions for all photostimulation conditions across the experimental genotypes (**Fig.22A,B**). The fit over-saturated at the extremes, overestimating the reaction times at low difficulties. Nevertheless, there was some semblance in the trends exhibited between these parameters and those in the drift-diffusion fits. In flies expressing dendritically targeted Chrimson, the bound height decreased with increasing light intensities, from 0.22 $\pm$ 0.05 (mean $\pm$ s.e.) to 0.03 $\pm$ 0.05, and eventually to 0 $\pm$ 0.03 (**Fig.22C**). Similarly, when the untargeted version was expressed, $\boldsymbol{A}$ dropped from 0.22 $\pm$ 0.07 (unstimulated) to 0.06 $\pm$ 0.06 (weakly stimulated), and to 0 $\pm$ 0.03 (strongly stimulated). A decision bound of height 0 meant that any evidence, regardless of its distribution, would be utilised to instantaneously drive a decision. This contradicted with the empirical data, since difficulty-dependent reaction times were still observed at high intensity optogenetic activation. This argues against the extrema detection model being the underlying process of olfactory decision-making.

For the sake of completeness, other parameters were also examined. Similar to the drift-diffusion model fit, the scaling factor $\boldsymbol{k}$ remained relatively unchanged by photostimulation in flies expressing targeted Chrimson; when the untargeted version was expressed, it appeared to be largest at high light intensity (**Fig.22D**). A reduction in $\boldsymbol{P_{max}}$, representing a flattening of the psychometric function, was also captured by this non-integration model (**Fig.22E**). Lastly, the residual times $\boldsymbol{t_R}$ were estimated to be around 0.25s here (**Fig.22F**), which was approximately half of what was computed in the drift-diffusion model (**Fig.22F**).

To quantitatively compare the extrema detection and drift-diffusion models, the BIC was used as the measure. $\boldsymbol{\Delta}$BIC values for unstimulated and stimulated data were plotted, given $\boldsymbol{\Delta}\mathrm{BIC} = \mathrm{BIC}_{\mathrm{extrema}} - \mathrm{BIC}_{\mathrm{DD}}$ (**Fig.23**). Since the model with a lower BIC value was preferred, the drift-diffusion model was favourable when $\boldsymbol{\Delta}$BIC was positive. In general, the drift-diffusion model provided a better description of

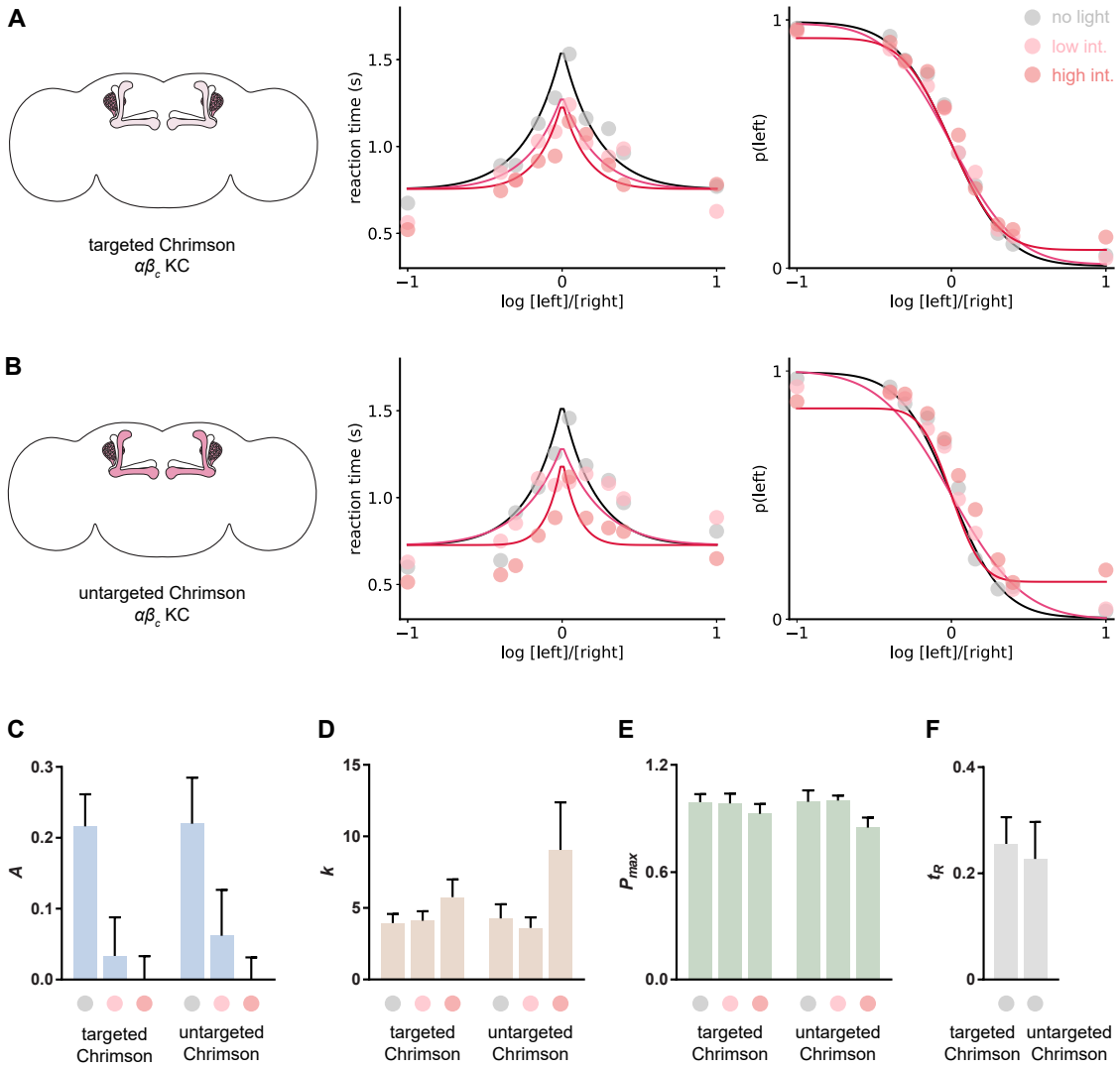


Fig. 22: Extrema detection modelling of reaction time and choice accuracy. Reaction time and choice accuracy plotted as a function of task difficulty for flies expressing dendritically targeted (**A**) or untargeted (**B**) Chrimson. Data points are identical to the ones presented in **Fig.13**. Data were fit with the extrema detection model (black, pink, and red lines), which assumed sequential sampling but not evidence integration. See **Methods** for model details. **A.** Middle: the model did not appear to fully capture the data, overestimating reaction times at the two ends of the chronometric function. Right: psychometric functions were similar for the three light conditions. **B.** Middle: model fits appeared visibly worse. Right: the model captured the decrease in maximal accuracy at high intensity, compressing the psychometric curve. **C.** Estimated parameters are described in this order: unstimulated; weakly photostimulated (0.01 mW mm^{-2}); strongly photostimulated (0.2 mW mm^{-2}). Error bar: s.e. Photostimulation progressively lowered the bound height A. Targeted Chrimson: A dropped from 0.22 ± 0.05 to 0.03 ± 0.05, then to 0 ± 0.03. Untargeted Chrimson: A dropped from 0.22 ± 0.07 to 0.06 ± 0.06, then to 0 ± 0.03. **D-F.** (Continued on the next page)

the data, apart from the unstimulated condition with targeted Chrimson (**Fig.23**). In particular, for strongly photostimulated flies expressing targeted Chrimson and weakly stimulated ones expressing untargeted Chrismon, the **Δ**BIC conveyed strong evidence (**Δ**BIC = 6–10) against the extrema detection model. Taken together, even though this model estimated somewhat similar trends in the free parameters compared with those in the drift-diffusion model (**Fig.13C-F**), the latter was superior in describing the chronometric and psychometric functions. The behavioural observations thus favoured an evidence integration strategy in decision-making.

Reaction time and experiment time

During the testing period, prolonged exposure to the odour without punishment might cause extinction of the aversive memory (Bouton, 2004; Felsenberg et al., 2018). Although the timescale of extinction was likely much longer than the 2-min testing period, I asked whether the flies' reaction times would change as a result of learning that the odour was no longer penalised. Focusing on the genotype in which dendritically targeted Chrimson was expressed, reaction times were plotted against their corresponding experiment times (i.e., when in the 2-min period the decision was made) (**Fig.24A**). Despite the difficulty-dependent increase in reaction times, there was no observable differences as the experiment progressed, in the

Fig. 22: A. (Continued from the previous page) **D.** From the extrema detection model fit, k seemed uninfuenced by photostimulation when targeted Chrimson was expressed: 3.94 ± 0.64; 4.10 ± 0.67; 5.75 ± 1.25. For untargeted Chrimson, k appeared largest at high intensity: 4.27 ± 0.99; 3.60 ± 0.75; 9.05 ± 3.33. **E.** Photostimulation generally did not change $\boldsymbol{P_{max}}$, although the model seemed to capture the reduction of maximal accuracy at high light intensity, in the untargeted condition (**B**, right). Targeted Chrimson: 0.99 ± 0.05; 0.98 ± 0.05; 0.93 ± 0.05. Untargeted Chrimson: 0.99 ± 0.06; 1.0 ± 0.03; 0.85 ± 0.06. **F.** As with drift-diffusion models, $\boldsymbol{t_R}$ was estimated only in the unstimulated condition, and taken as constant in the models of photostimulated data. They were 0.26 ± 0.05s and 0.23 ± 0.07s for the dendritically targeted and untargeted genotypes, respectively.

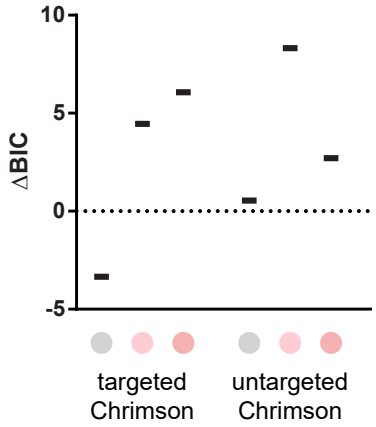


Fig. 23: Comparison of drift-diffusion and extrema detection model fits. The two models were evaluated by BIC. **Δ**BIC = $\text{BIC}_{\text{extrema}} - \text{BIC}_{\text{DD}}$. A positive **Δ**BIC favoured the drift-diffusion model, since the lower the BIC value, the better the model fit. Apart from the unstimulated condition for flies expressing targeted Chrimson, drift-diffusion model performed better than extrema detection. **Δ**BIC values between 6-10 conveyed strong evidence against the latter.

unstimulated (**Fig.24Ai**), weakly stimulated (**Fig.24Aii**), and strongly stimulated (**Fig.24Aiii**) conditions. This was confirmed by the extremely low $\boldsymbol{R^2}$ values between reaction time and experiment time (**Fig.24B**).

Interestingly, I noticed in **Fig.24A** that the density of decisions appeared to decrease with experiment time. To quantify this, I divided the experimental duration into four 30s quarters, and tallied the number of decisions within each one (**Fig.24C**). Across all odour contrasts, there was a clear descending trend in the decision frequency which was unaffected by photostimulation. Possible explanations for this behaviour included excessive grooming, lethargy, and potentially exhaustion.

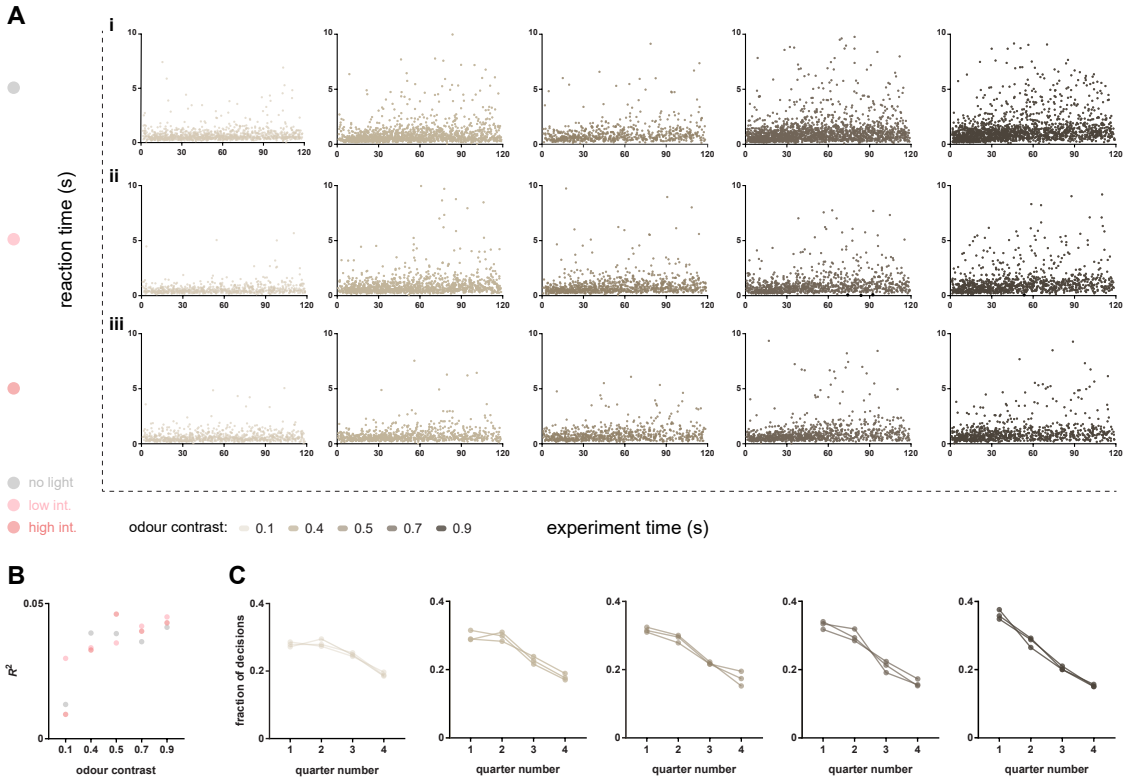


Fig. 24: Influence of experimental duration on reaction time (I).
Data from flies expressing dendritically targeted Chrimson. **A.** Reaction times are plotted as a function of their corresponding experiment times, in the unstimulated (**i**), weakly photostimulated (0.01 mW mm^{-2}, **ii**), and strongly photostimulated (0.2 mW mm^{-2}, **iii**) conditions. There was no correlation between the two variables, exemplified by the very low (<0.05) $\boldsymbol{R^2}$ values, shown in **B**. **C.** Experimental duration was divided into four 30s quarters, and the number of decisions made within each one was quantified. Decision frequency, unaffected by photostimulation, declined as the experiment progressed.

3.4 Optogenetic silencing $\alpha\beta_c$ KCs during behaviour

Given that optogenetic activation of $\boldsymbol{\alpha\beta_c}$ KCs during the odour-guided task sped up the flies' reaction times (**Fig.13**), I reasoned that observing the opposite behavioural effects (e.g., slowing down of reaction time) when core KCs were silenced would reinforce the argument of causality. I sought to optogenetically suppress KC activity during decision-making using flies that restrictively expressed *Gt*ACR1 in $\boldsymbol{\alpha\beta_c}$ KCs. The combination of *GAL4* and *LexA* core KC drivers, *lexAopFLP*, as well as *UAS-FRT-stop-FRT*-Gt*ACR1::EYFP*, which I constructed, achieved this restrictive expression (**Fig.9**). Patch-clamp recordings then demonstrated the chloride channel's functionality in transducing photocurrents to hyperpolarise the membrane potential (**Fig.11**). In the behavioural chamber, these flies were either unstimulated (control), or photostimulated with a constant pulse of strong green light (0.2 mW mm^{-2}) whenever they entered the decision zone. Reaction times and choice accuracies were analysed similarly as with the activation experiment.

The chronometric and psychometric functions in the unstimulated condition were very different in shape compared with those of flies expressing targeted or untargeted Chrimson (**Fig.25A**). Although variable, mean reaction times displayed a rough difficulty-dependence, from 0.92 $\pm$ 0.03s (mean $\pm$ s.e.m.) and 1.02 $\pm$ 0.03s at the easiest difficulties, to 1.26 $\pm$ 0.06s and 1.3 $\pm$ 0.08s at the highest (**Fig.25A**, middle panel). However, the increase was small, and as a result, the chronometric function appeared flattened. Equally, the psychometric function had a shallow slope, with low maximal accuracies of 84% and 86% (**Fig.25A**, right panel).

Under green photostimulation, the reaction times and accuracies differed. Again, the chronometric function appeared compressed, with only a $\sim$0.3s increase between the lowest and highest difficulties (**Fig.25A**, middle panel). Contrary to previous expectation, hyperpolarising the membrane potential of $\boldsymbol{\alpha\beta_c}$ KCs during behaviour seemed to quicken the flies' decisions. Nonetheless, when reaction times at the

same odour contrast were pooled, the means were only significantly different at the easiest difficulty (unpaired, two-tailed $\boldsymbol{t}$ test, $\boldsymbol{p = 0.014}$) (**Fig.25F**). The reaction time distributions for both conditions exhibited positive skew, whereas those of transit times were more symmetrical (**Fig.25F**). As with the Chrimson experiments, transit times of flies expressing *Gt*ACR1 were difficulty-independent (**Fig.16C**, middle panel); however, they were slightly quicker (∼1s) than those in Chrimson-expressing flies (1.1–1.3s). Green photostimulation consistently elevated transit times across difficulties: the mean percentage increase was ∼11% (**Fig.16C**, right panel). Meanwhile, the psychometric function was smoother and steeper compared with the unstimulated condition (**Fig.25A**, right panel). The maximal accuracies were higher, at 89% and 90%. Overall, photostimulation appeared to enhance the flies' performance across all difficulties, which was unexpected.

Despite these baffling differences, I proceeded to fit the data with a drift-diffusion model to examine how photostimulation might alter the bound height $\boldsymbol{A}$, sensitivity coefficient $\boldsymbol{k}$, and maximal accuracy $\boldsymbol{P_{max}}$ (residual time $\boldsymbol{t_R}$ was assumed to be unchanged) (**Fig.25B-E**). $\boldsymbol{t_R}$ was estimated to be 0.77 ± 0.13s (mean ± s.e.), which was larger than the ∼0.55s in the Chrimson genotypes (**Fig.25E**). $\boldsymbol{A}$ and $\boldsymbol{P_{max}}$ remained unaffected by light, at ∼0.63 and ∼0.85, respectively (**Fig.25B,D**). The scaling factor $\boldsymbol{k}$ seemed higher in the photostimulated condition, at 6.23 ± 0.97, compared with 3.67 ± 1.72 in the unstimulated control, but there were large uncertainties in the parameter estimation (**Fig.25C**). Taken together, it appeared that changes in $\boldsymbol{k}$, which pertained to an enhanced coupling between difficulty and drift rate, explained the majority of the photostimulated effect on reaction time and choice accuracy. However, biologically, it was unclear how the silencing of $\boldsymbol{\alpha\beta_c}$ KCs would result in higher drift rates. Assuming that this was what caused the reaction times to be faster, it was even more puzzling that there was a concomitant increase in choice accuracies when photostimulated (**Fig.25A**, right panel).

In search for clues to explain these unexpected behavioural data, I further examined whether flies altered their reaction times as the experiment progressed,

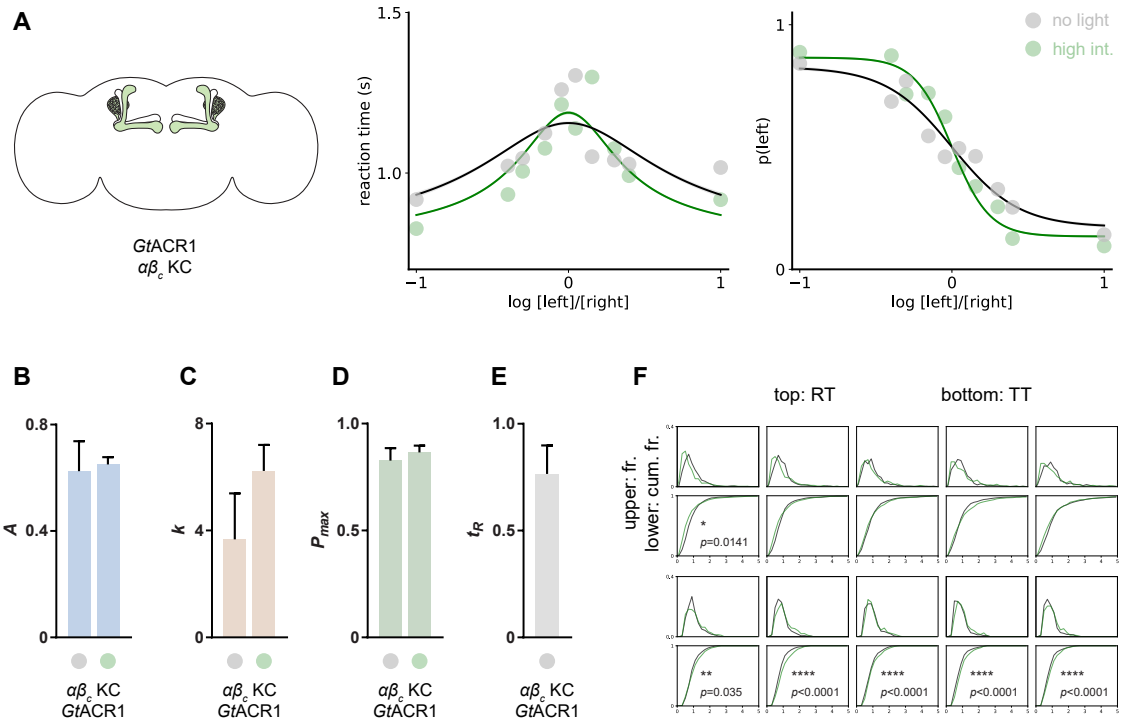


Fig. 25: Behavioural data from flies expressing *Gt*ACR1.
A. Reaction time and choice accuracy data from flies expressing *Gt*ACR1 in $\boldsymbol{\alpha\beta_c}$ KCs are plotted as a function of task difficulty, and fit with a drift-diffusion model (black and green lines). Middle: the difficulty-dependent increase in reaction time was small (only ∼0.3s for both unstimulated and photostimulated — 0.2 mW mm^{-2} — flies), which meant that the chronometric functions were shallower than those when flies expressed Chrimson. For most difficulty levels, optogenetic silencing of $\boldsymbol{\alpha\beta_c}$ KCs appeared to quicken mean reaction times. Unstimulated: $\boldsymbol{n}$=239–580; photostimulated: $\boldsymbol{n}$=277–374 reactions per difficulty. Right: in the unstimulated control, the psychometric function was shallow, with maximal accuracies: 84% and 86%. Green photostimulation steepened the curve, enhancing the maximal accuracies to 89% and 90%. Unstimulated: $\boldsymbol{n}$=43–56; photostimulated: $\boldsymbol{n}$=40–63 flies per difficulty. **B.** Estimated parameters are described in this order: unstimulated; strongly photostimulated. Error bar: s.e. A was unaffected by photostimulation: 0.62 ± 0.11; 0.65 ± 0.03. **C.** k changed from 3.67 ± 1.72 to 6.23 ± 0.97 upon illumination. **D.** $\boldsymbol{P_{max}}$ remained unchanged: 0.83 ± 0.06; 0.87 ± 0.03. **E.** $\boldsymbol{t_R}$ (0.77 ± 0.13s) was only estimated for the unstimulated condition, and the value was used as a constant in the photostimulated condition. **F.** Reaction (top) and transit (bottom) time distributions and cumulative distriutions, exhibiting positive skew and symmetry, respectively. Across five odour contrasts, mean reaction and transit times between light conditions were compared using unpaired t test with Welch's correction. p-values shown in figure. RT: reaction time. TT: transit time.

since the high odour concentration (10 ppm) was no longer penalised during the testing phase. Reaction times were unaffected by experiment times (**Fig.26A**), exemplified by the low $\boldsymbol{R^2}$ values between the two variables (**Fig.26B**). As with flies expressing Chrimson (**Fig.24C**), decision frequency declined as a function of time, although this trend appeared to be more salient at high difficulties (**Fig.26C**).

To conclude, the variable reaction time and accuracy data seemed to suggest that optogenetic silencing of $\boldsymbol{\alpha\beta_c}$ KCs quickened the flies' reaction times and made them more accurate, although their performance in the unstimulated control was poor. The drift-diffusion model fit further estimated that photostimulation increased the sensitivity coefficient $\boldsymbol{k}$, despite a considerable standard error in the parameter fit. Lastly, since these flies carried a rather high transgene load (4 transgenes), their behavioural output might be compromised, which could affect the reliability of the reaction time and accuracy data shown here. It would be best if this experiment were to be repeated, and analysed in conjunction with more control groups where *Gt*ACR1 was expressed in say, $\boldsymbol{\alpha}$'$\boldsymbol{\beta}$' KCs, or not expressed at all.

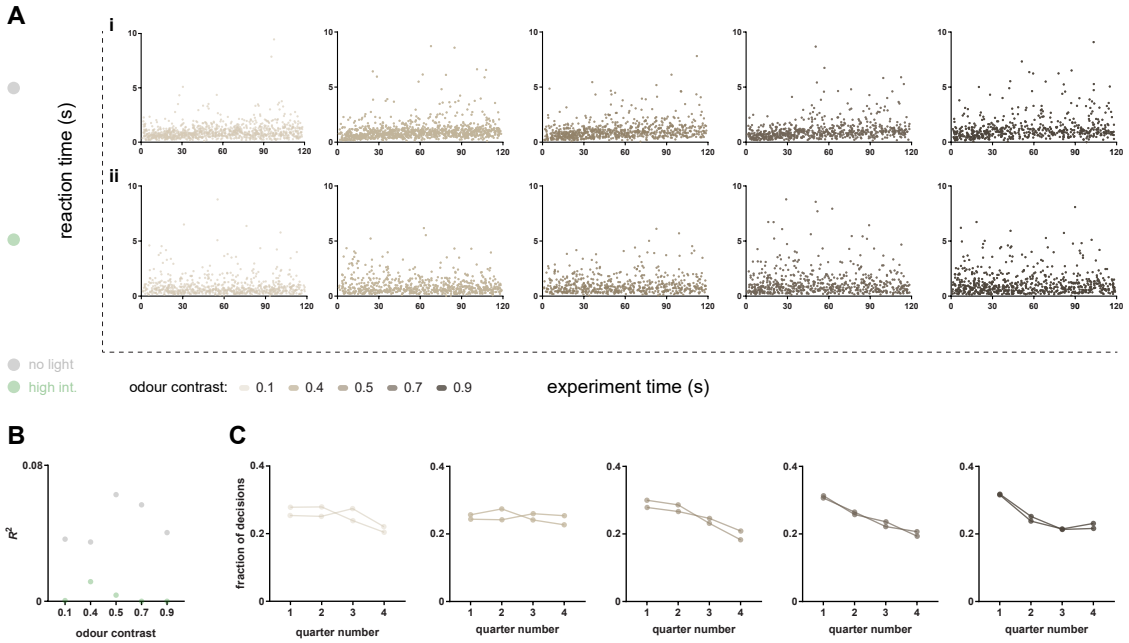


Fig. 26: Influence of experimental duration on reaction time (II).
Same convention as **Fig.24**. Data from flies expressing *Gt*ACR1 in $\boldsymbol{\alpha\beta_c}$ KCs. **A.** Experiment time did not influence reaction times in both unstimulated (**i**) and strongly photostimulated (0.2 mW mm^{-2}; **ii**) conditions. **B.** $\boldsymbol{R^2}$ values between these two variables were low. **C.** The testing phase was divided into four 30s quarters. As the experiment progressed, decision frequencies showed a decreasing trend, more prominently at high difficulties.

I never discuss discussions.

— Dag Hammarskjöld

4 Discussion

To investigate the neural mechanisms of temporal integration when fruit flies make odour-guided decisions, my work connects molecular cloning, electrophysiological recordings, closed-loop optogenetics, and drift-diffusion modelling to test for the causal contribution of $\boldsymbol{\alpha\beta_c}$ KC activity to behaviour.

4.1 Compartmentalised expression of optogenetic tools

Experiments that probe the causal relationship between cell-localised neural activity and behavioural output often benefit from spatiotemporally precise manipulations of neuronal firing (Emiliani et al., 2015; Shemesh et al., 2017; Zhang et al., 2018). This can be aided by the subcellular localisation of optogenetic actuators that tailors stimulation kinetics to the experimental design (Rost et al., 2017). For instance, in optogenetic circuit mapping, targeting of Channelrhodopsin-2 (ChR2) to the somatodendritic compartment of presynaptic neurons can prevent the concurrent activation of co-localised, but often functionally irrelevant axons (Lewis et al., 2009; Petreanu et al., 2007).

In my experimental paradigm, dendritic expression of the light-gated cation channel Chrimson is necessary for the optical injection of small amplitudes of depolarising current, mimicking EPSCs that carry sensory information. By testing eight different motifs selected based on known examples of dendritic targeting, I show that only the 39-aa sequence from the proximal cytoplasmic tail of human AMPAR GluR1 subunit (Ruberti and Dotti, 2000) can restrict Chrimson expression to MB calyces, the somatodendritic compartment of $\boldsymbol{\alpha\beta_c}$ KCs (**Fig.8**). Fluorescence intensity of tdTomato fused with Chrimson is markedly concentrated in the four spherical clusters per hemisphere, where KCs arborise dendritic claws to receive PN inputs (**Fig.8F**). Since this signal can direct a chimera that contains the primarily axonal glycoprotein HA to the dendrites of cultured hippocampal neurons (Ruberti and Dotti, 2000), its targeting efficacy in this study is perhaps not surprising. The unforeseen result is that it remains the only motif in my assorted selection capable of targeting the expression of Chrimson::tdTom. Shal, being the endogenously expressed, dendritically targeted K_v**4** channel in $\boldsymbol{\alpha\beta_c}$ KCs (Groschner et al., 2018; Rivera et al., 2003), should provide a motif most compatible with the protein-sorting machinery and physiological conditions of these neurons. Yet Chrimson::tdTom appended with the 16-aa Shal motif still expresses ubiquitously and strongly in both the axonal and somatodendritic compartments (**Fig.8A**). It is difficult to pinpoint the reason behind this subversion of expectation, given that our understanding of the mechanisms of Shal localisation is restricted to its interaction with SIDL via the di-leucine motif (Diao et al., 2010), but a potential clue is the size difference of the target proteins. Shal is composed of 571 aa, whereas the fusion protein Chrimson::tdTom is 855 aa in length, similar to AMPAR GluR1 (888 aa). It is possible that the Shal dendritic signal is nullified by either the more extensive folding, or the bulkiness during cytoskeletal transport, of larger proteins. Indeed, the rat nAChR$\boldsymbol{\alpha}$7 subunit, whose 47-aa motif shows no dendritic targeting effect (**Fig.8G**), also consists of only 509 aa. Of course, this is a crude comparison and merely speculative — by no means experimentally grounded; a counterexample is

the 843 aa-long mouse NLG1, which contributes an equally non-functional targeting signal for Chrimson (**Fig.8D**).

It appears that in many cases, dendritic targeting of proteins relies not only on correct sorting in the trans-Golgi network, but also on directional intracellular trafficking (Lasiecka and Winckler, 2011), implicating motor proteins such as myosins (Correia et al., 2008; Osterweil et al., 2005), kinesins (Chu et al., 2006), and dyneins (Kapitein et al., 2010) in the process. In particular, myosin Va has been demonstrated to mediate the dendritic targeting of AMPAR GluR1, because expression of its dominant-negative variant disrupts the subunit's cellular localisation (Lewis et al., 2009). Fusion with the myosin Va binding domain from melanophilin suffices to target ChR2 to the dendritic arbors of cortical pyramidal neurons (Lewis et al., 2009). However, this motif is ineffective in targeting Chrimson::tdTom (**Fig.8E**). One explanation could be that the *Drosophila* orthologue myosin V and the vertebrate myosin Va have diverged in sequence, structure, and function to a degree that the motif extracted from murine melanophilin does not recognise the globular tail domain of fly myosin V. Indeed, *Drosophila* myosin V seems to employ a distinct motor mechanism from its vertebrate counterpart (Tóth et al., 2005), and analysis of the melanophilin binding site (Fukuda and Kuroda, 2004) reveals only modest homology (∼35% identity) between the two orthologues.

Another unexpected result comes from the motif in the mouse cell adhesion molecule TLCN, taken as the targeting component in the dendritic marker DenMark (Nicolaï et al., 2010), a genetic tool frequently used in *Drosophila* neurobiology. Whereas DenMark expressed in adult MB in the original study shows clean, near-perfect mCherry fluorescence restricted to the calyces, Chrimson::tdTom::TLCN-motif exhibits ubiquitous expression throughout the KCs (**Fig.8B,C**). It appears that fusion with Chrimson::tdTom drastically affects the dendritic targeting efficacy of the 17-aa peptide. Similarly, although a hybrid motif that fuses sequences from TLCN and K_v**2.1** can restrict *Gt*ACR1 and *Gt*ACR2 to the dendrites of layer 2/3

pyramidal neurons (Messier et al., 2018), it is inefficient in $\boldsymbol{\alpha\beta_c}$ KCs, allowing widespread Chrimson::tdTom trafficking to the $\boldsymbol{\alpha\beta}$ lobes (**Fig.8H**). In any case, it is becoming increasingly obvious that somatodendritic targeting is regulated by multiple sorting signals and binding partners (Lasiecka and Winckler, 2011), and it is difficult to predict whether putatively targeting signals are functionally conserved in different contexts and across species: for example, the dendritic sorting sequence in AMPAR GluR1 lacks the well-described tyrosine, di-leucine (as in Shal; Rivera et al., 2003) or PSD-95/Dlg/ZO-1 (PDZ) motifs (Ruberti and Dotti, 2000), but it is the sole successful candidate in my work. In mouse retinal ganglion cells, however, it fails to target ChR2 to the dendritic field (Wu et al., 2013). It is the NLG1 motif, ironically, that mediates significant dendritic targeting there.

4.2 Functionality of optogenetic tools

I further demonstrate that these optogenetic tools function *in vivo* by performing whole-cell patch-clamp recordings of $\boldsymbol{\alpha\beta_c}$ KCs in head-fixed flies. In neurons expressing dendritically targeted Chrimson, red photostimulation elicits depolarisations with a maximum amplitude of ∼10 mV (**Fig.10A,C,D**), which is sufficient to bridge the voltage gap of 8.2 mV between resting membrane potential and spike threshold (Groschner et al., 2018). As discussed in **Results**, the absence of spiking may simply be a consequence of poor technique or cellular ill health; however, a larger number of Chrimson-positive neurons need to be recorded in order to obtain more conclusive results. Here, the light intensity used is very high, at 4 mW mm^{-2}, which is significantly greater than those selected for the behavioural experiments (0.01 and 0.2 mW mm^{-2}). Of course, the conditions of photostimulation between the electrophysiological rig and behavioural chamber can hardly be compared, since the brain is stationary and directly exposed to light when neurons are patch-clamp recorded, whereas during behaviour, light has to penetrate the intact cuticle of a freely moving fly to reach the $\boldsymbol{\alpha\beta_c}$ KCs. In my experimental paradigm, there is no reliable way to measure the real-time activity of decision-relevant neurons during the task, as well as how this activity may change during optogenetic interrogation (see next section). Nonetheless, within the current framework, it would be ideal to test a wider range of light intensities (including the two levels specified in behavioural experiments) and stimulation protocols (e.g., single versus frequency pulses). It would also be informative to perform voltage-clamping to measure Chrimson photocurrents and deduce the channel's reversal potential, just as I have done for *Gt*ACR1. In the olfactory decision-making task, I compare the reaction times and choice accuracies between flies expressing dendritically targeted or untargeted Chrimson, and justify the differences based on the assumption that Chrimson localisation (or lack thereof) would alter the kinetics of photostimulation: when the activator is strongly and ubiquitously expressed, large light-induced depolarisations would quickly bring the neuron to spiking. This

has not been explicitly demonstrated. Therefore, whole-cell recordings of $\boldsymbol{\alpha\beta_c}$ KCs expressing Chrimson::tdTom::NLG1-motif (untargeted) would greatly complement my results, such that differences in optogenetic stimulation parallel differences in behavioural measures of speed and accuracy.

One of the major arguments I present for the usage of a dendritically localised optogenetic actuator is to avoid direct, light-evoked activation of downstream MBONs. Again, this has not been shown here in electrophysiological recordings (Vrontou et al., 2021), but merely inferred from behaviour: optogenetic activation mediated by targeted Chrimson quickens reaction times in a difficulty-dependent manner, and barely affects choice accuracy (**Fig.13A**). The argument follows that photostimulation of widespread, untargeted Chrimson, in contrast, would promptly fire KC-MBON synapses, leading to a flattening of both the chronometric and psychometric functions. Currently, this is only construed from behavioural observations as well. Indeed, patch-clamp recordings of MBONs, such as the downstream MBON-$\boldsymbol{\alpha}$2sc, would provide the most direct evidence to support or refute this argument.

Intriguingly, photostimulation causes a slight hyperpolarisation in an unlabelled, thus Chrimson-negative KC (**Fig.10B**). It is unclear whether this is an $\boldsymbol{\alpha\beta_c}$ KC excluded by the *NP6024-GAL4* driver, or another type of KC, such as $\boldsymbol{\alpha'\beta'}$. However, its location within the same cluster as the red-fluorescent, Chrimson-positive cells as well as the similar morphology with its neighbours favour its membership in the $\boldsymbol{\alpha\beta_c}$ population. This could be evidence for KC-KC lateral inhibition, most probably mediated by the giant GABAergic neuron APL (Lin et al., 2014; Vrontou et al., 2021). In a race structure of decision-making, mutual inhibition between competing integrators is a crucial element in the description of a drift-diffusion process (Bogacz et al., 2006). The dense, global KC connectivity of APL can provide inhibitory feedback onto 'up' or 'down' KCs, facilitating the decorrelation of antagonistic representations by amplifying differences in conflicting evidence (Amin

et al., 2020; Lin et al., 2014). Presynaptic active zones have been found on both KCs and the non-spiking APL at MB calyces, suggestive of the bidirectional interaction between them. At the APL-KC synapses, the rate of GABA release mirrors local voltage changes in a graded manner, similar to how APL's locust analogue, the giant GABAergic neuron (GGN), exerts inhibition on KCs (Papadopoulou et al., 2011. On the other hand, neurotransmitter release from $\boldsymbol{\alpha\beta_c}$ KC dendrites also appears to be driven by analogue, graded potential (Vrontou et al., 2021), in contrast to the spike-dependent transmission at KC-MBON synapses. Interestingly though, the timeframe of delayed hyperpolarisation (latency of $\sim$290 ms) to light onset seen in **Fig.10B** seems inconsistent with the fast kinetics of $GABA_A$ receptors (Su and O'Dowd, 2003; Vrontou et al., 2021). Perhaps a more complex, polysynaptic inhibitory network is at work here.

For the optogenetic silencing of $\boldsymbol{\alpha\beta_c}$ KC activity, I present a more comprehensive characterisation of the functionality of *Gt*ACR1, the light-gated chloride channel. Measurements of voltage-clamped photocurrents estimate a reversal potential of -96 mV for the channel (**Fig.11A-C**), which exceeds the theoretical value of -120 mV (given the extracellular and intracellular ionic concentrations) by some margin. In principle, some degree of cation conductance, such as that of Ca^{2+}, may elevate the reversal potential. However, this seems highly unlikely, given previous reports of *Gt*ACR1's cation impermeability (Govorunova et al., 2015). Without more detailed experimentation, it is currently difficult to explain this conundrum. Meanwhile, pulses of green illumination hyperpolarise *Gt*ACR1-positive cells (**Fig.11F**), abrogate spiking activity (**Fig.11D,E**), suppress odour responses (**Fig.11G**), and silence the downstream MBON (**Fig.11H**). Contrary to previous studies (Mahn et al., 2018; Messier et al., 2018), no andtidromic spikes are observed, and photostimulation does not excite the postsynaptic neuron (MBON-$\boldsymbol{\alpha}$2sc) (**Fig.11H**). These recordings provide firm support for *Gt*ACR1 as an effective optogenetic inhibitor suitable for my closed-loop silencing experiments.

4.3 Causal contribution of $\alpha\beta_c$ KC activity

Combining an odour-guided decision-making task with closed-loop optogenetics on a custom-designed experimental setup, I show that activation of $\boldsymbol{\alpha\beta_c}$ KCs by injecting small, EPSC-like currents to their dendrites during behaviour suffices to speed up the fly's reaction times (**Fig.13**), akin to widening the temporal bottleneck of the decision process. Importantly, this light-induced effect is a function of task difficulty. When the activation is reinforced (using untargeted Chrimson), reaction times become even shorter, and a concomitant worsening of task accuracy is observed (**Fig.13**). Furthermore, similar activation of the $\boldsymbol{\alpha'\beta'}$ KCs, as well as illumination of control flies that lack Chrimson, yield no significant changes to parameters of speed and accuracy (**Fig.14**). These behavioural changes directly demonstrate the causal role of $\boldsymbol{\alpha\beta_c}$ KC activity in olfactory decision-making.

The relationship between reaction time, choice accuracy, and perceptual difficulty is well-described by a drift-diffusion model (**Fig.1**), consistent with the process of evidence accumulation to bound (Bogacz et al., 2006; Palmer et al., 2005). Both DasGupta et al. (2014) and Groschner et al., (2018) pool data from reciprocal difficulties (e.g., 1 vs 10 and 10 vs 1 ppm), yielding truncated plots of the psychometric and chronometric functions. Here, I show the full curves across the whole spectrum of odour contrast, producing characteristic dome-shaped and sigmoidal functions for reaction times and accuracies, respectively (**Fig.13A,B**). The assumed linear scaling between drift rate and difficulty (by the coefficient $\boldsymbol{k}$) can be explicitly demonstrated with a Bayesian drift-diffusion model, but only in the central range of difficulty levels (**Fig.21A,B**). A more realistic scaling relationship between $\boldsymbol{\mu'}$ and $\boldsymbol{x}$, such as a sigmoidal, is expected to contribute to a better model. In the current study, I fit a parsimonious model of three or four parameters (depending on whether $\boldsymbol{t_R}$ is fixed) that excludes any biases or collapsing bounds — an implementation of the so-called 'urgency signal' (Drugowitsch et al., 2012). Additional complexities such as this, i.e., time-dependent decrease of bound

height, can be implemented in future modelling work for a better approximation of biological reality. Unlike the model in Hanks et al. (2006), the one I utilise is blind to the effects of stimulation, since there is no explicit term to describe light-induced changes. Instead, comparison of parameter values — or in the Bayesian model, posterior distributions — serves as the proxy for evaluating the influence of optogenetic activation. On the whole, the parsimonious drift-diffusion model I employ produces satisfactory fits to empirical data (**Fig.13**, **Fig.14**).

The most prominent effect of photostimulation appears to be a reduction in the bound height $\boldsymbol{A}$, observed in both the targeted and untargeted Chrimson genotypes (**Fig.13C**). On the contrary, the sensitivity coefficient $\boldsymbol{k}$ remains unaffected (**Fig.13D**). These trends are replicated by data analysis using a Bayesian model (**Fig.21**). What do these changes, or lack thereof, in $\boldsymbol{A}$ and $\boldsymbol{k}$ entail in regard to the role of $\boldsymbol{\alpha\beta_c}$ KC activity in the decision process? In the drift-diffusion framework, a decrease in bound height can also be treated as an increase, or a constant offset towards threshold, in the DV, compatible with the addition of neural activity by Chrimson photocurrents (**Fig.27A**). It represents a direct perturbation of the DV, a quantity representing the integrated evidence. On the other hand, changing $\boldsymbol{k}$ is equivalent to varying the strength of momentary evidence: in this case, olfactory information favouring either the left or right choice. It should only indirectly affect the DV, by changing the rate at which momentary evidence accrues (**Fig.27B**). The fact that photostimulation of $\boldsymbol{\alpha\beta_c}$ KCs, at low and high intensities, only precipitates an effect in $\boldsymbol{A}$ but not $\boldsymbol{k}$, provides a strong case for the encoding of a DV, or a closely related quantity, by these neurons. They are temporal integrators of sensory information (Groschner et al., 2018). This line of thinking is reminiscent of the analysis in Hanks et al. (2006), in which the behavioural effects of MT and LIP microstimulation when monkeys perform the random-dot motion task are modelled and compared. The authors reason that stimulation of LIP leads to an offset to the decision bound, whereas that of MT increases drift rates, implicating the two regions in distinct positions along the causal chain of decision-making (Hanks et al., 2006).

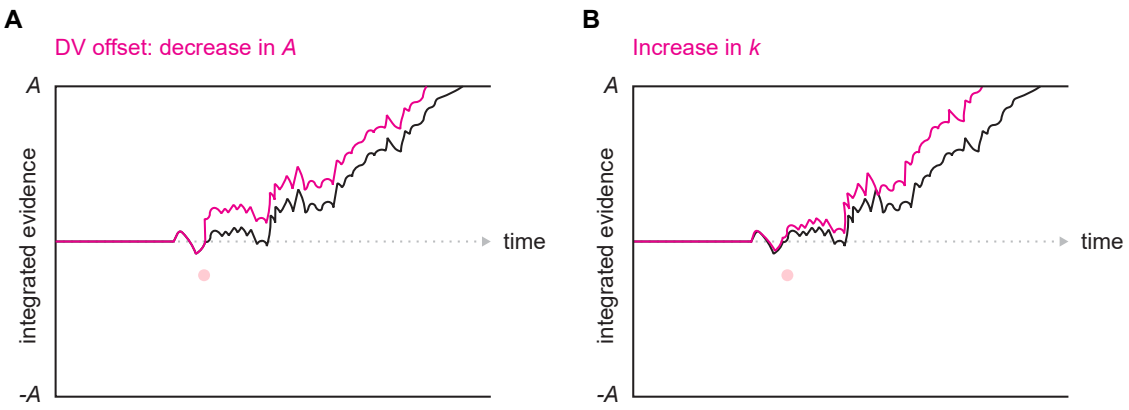


Fig. 27: Two distinct mechanisms explaining changes to the DV.
A. In the drift-diffusion framework, a decrease in bound height A equates to a constant offset towards threshold in the DV. Optogenetic activation (red curve) of 'up' or 'down' $\boldsymbol{\alpha\beta_c}$ KCs by injecting EPSC-like currents to the dendrites appears to mimic an additive offset to the DV. **B.** Alternatively, an increase in the sensitivity coefficient k quickens the drift rate and influences the evolution of the DV. Pink dot indicates the onset of optogenetic activation. Adapted from Gold and Shadlen, 2007.

The idea behind the dendritic targeting of Chrimson is to enable the addition of small, subthreshold amplitudes of voltage, which also serves to differentially activate either the 'up' or 'down' subsets of $\boldsymbol{\alpha\beta_c}$ KCs. Whether or not Chrimson is localised should dictate how the neurons are excited: dendritically restricted Chrimson brings about increases in subthreshold membrane potential, leading to the eventual emission of an action potential, whereas ubiquitously expressed Chrimson introduces suprathreshold activation. Compared with the former, the latter condition suffers from a more severe light-induced flattening of the chronometric function, in conjunction with a reduction in maximal accuracy when strongly photostimulated (**Fig.13A,B**). One may argue that this only reflects a difference in the abundance of the channel, rather than the manner in which the neurons are activated. Admittedly, it is difficult to discriminate between the two mechanisms based on the current results, but in future experiments, one can titrate the levels of functional Chrimson by varying the concentration of all-trans retinal in the fly food, or the duration for which the flies are kept on this food. On the other hand, it is surprisingly that the behavioural difference between the two genotypes is not captured by model estimates of $\boldsymbol{A}$: the amplitude of reduction is very similar (**Fig.13C**). A possible

explanation is that this difference is instead expressed in the concurrent, albeit statistically indistinguishable, changes in $\boldsymbol{k}$ (**Fig.13D**).

So far, my results point to a process of temporal integration (also compare the drift-diffusion framework with extrema detection; **Fig.22**) causally involving the neural activity in $\boldsymbol{\alpha\beta_c}$ KCs. However, they do not seem to provide clear evidence to dissociate between subthreshold or suprathreshold mechanisms in the rate-limiting integration step. Indeed, how is the light-induced offset in DV implemented in a neural substrate — is it principally mediated by deflections of the membrane potential or increases in spike rates? The fact that a single 25 ms pulse of red light — two orders of magnitudes smaller than the timescales of fly reaction times — suffices to quicken the animal's decisions by adding dendritic voltage, offers some food for thought. How long does the light-evoked activity persist in the integrator, such that it translates to changes in behaviour? $\boldsymbol{\alpha\beta_c}$ KCs are characterised by their prolonged decay time constants of ∼300 ms (Groschner et al., 2018), i.e., it may take ∼1s for EPSPs to dissipate. Meanwhile, suprathreshold mechanisms may provide even longer accumulator memory, possibly in the range of several seconds. Hypothetically, downstream MBONs could employ simple spike-based strategies, such as spike counting, in the process of integration. The time constants that such a mechanism entails will be highly dependent on the complex recurrent circuitry between KCs and MBONs (Aso et al., 2014a; Li et al., 2020), and are currently unknown. At a single-trial level, for the latencies to first spike in subsets of $\boldsymbol{\alpha\beta_c}$ KCs to dictate reaction times (Groschner et al., 2018), a high degree of noise correlation is presumably necessary; otherwise, a considerable portion of neurons will have released action potentials before the population average of spike latencies, and it becomes ambiguous when the choice should be triggered. In vertebrate pyramidal neurons, mean noise correlations of 0.1–0.2, depending on the cortical area, are typically observed (Cohen and Kohn, 2011; Zohary et al., 1994). In *Drosophila* KCs, such correlations may arise from shared inputs (Aso et al., 2014a), but the

extent of this correlated variability remains to be quantified, possibly by paired recordings of $\boldsymbol{\alpha\beta_c}$ KCs during odour exposure.

Given that increasing the activity of $\boldsymbol{\alpha\beta_c}$ KCs causes flies to speed up their decisions, it is tempting to speculate that the opposite manipulation, i.e., an inhibition of the evidence integrator during behaviour, would prolong reaction times. Surprisingly, my results from flies expressing *Gt*ACR1 suggest otherwise (**Fig.25**). The light-induced quickening of reaction times points to paradoxical KC activation — a premature emission of action potentials. This seems highly unlikely, in view of the evidence from whole-cell patch-clamp recordings (**Fig.11**). However, green illumination may not have silenced all odour-evoked first spikes: in **Fig.11G**, a single action potential has 'escaped'. Another possible explanation involves a change in ionic conditions in response to repeated photoinhibition, as the cells fill with chloride. Admittedly though, it is difficult to imagine a steep chloride gradient between the extracellular (114 mM Cl^-) and intracellular (1 mM Cl^-) environment being reversed by a passive channel such as *Gt*ACR1. Since $\boldsymbol{\alpha\beta_c}$ represents only a subset of KCs — one that is particularly adept in encoding changes in odour concentration — there is also a possibility that other odour-responsive KC populations take over when $\boldsymbol{\alpha\beta_c}$ KCs are suppressed. It is unclear, however, whether this will entail a quicker commitment to choice, and it remains deeply baffling that photoinhibition improves choice accuracy. In any case, a more in-depth investigation, perhaps in conjunction with *Gt*ACR1-negative control experiments, is needed.

While many studies of olfactory behaviour and sensorimotor processing in the fruit fly have focused on odour-guided navigation (Álvarez-Salvado et al., 2018) and complex plume tracking (Demir et al., 2020), my work examines the psychophysical consequences of a learned behaviour, using a novel, closed-loop optogenetic paradigm of a perceptual task. Perhaps not surprisingly, the fly's decision-making performance causally relates to structures that have long been the research subject in insect learning and memory (Heisenberg et al., 1985; Keene and

Waddell, 2007), since the task relies on a short-term memory of negative valence of the reinforced odour concentration. The fly employs this flexible circuit that includes sparse, high-dimensional KC representations and valence-mapping in the KC-MBON compartments to inform odour-guided decisions. In this paradigm, $\boldsymbol{\alpha\beta_c}$ KCs are well-suited to act as the temporally rate-limiting integrators of information due to their characteristic biophysical properties (Groschner et al., 2018). I envision that other types of perceptual decisions may utilise analogous sets of neurons as evidence accumulators.

The most convincing approach in the mapping of neural mechanisms to behaviour is to visualise the activity in individual or populations of neurons during single trials. Here however, the experimental paradigm precludes the real-time tracking of $\boldsymbol{\alpha\beta_c}$ KC activity when olfactory information is presented and during the period leading up to a choice. Measurements of neural activity and behaviour are performed separately. This represents a major limitation in the study, which is difficult to overcome unless the setup for the perceptual task is radically modified. An attractive alternative is to tether (head- and body-fixed) the fly onto an air-supported, spherical treadmill, allowing free locomotion while the experimenter records neural activity via electrophysiology or Ca^{2+} imaging (Loesche and Reiser, 2021; Pimentel et al., 2016; Seelig et al., 2010). While patch-clamping can only probe the activity of one or two neurons, population imaging using Ca^{2+} indicators may be too slow to capture the rapid kinetics of spiking events, and poor in tracking subliminal voltage changes, especially at low contrasts (Lin and Schnitzer, 2016). Fluorescent genetically encoded voltage indicators, such as ASAP3, can potentially overcome these challenges, as they reveal subthreshold activity as well as action potentials with sub-millisecond and subcellular resolution (Villette et al., 2019). This kind of fly-on-the-ball setup has mainly been utilised to indulge the animal in a virtual reality for the study of navigational behaviours (Dombeck and Reiser, 2012; Kim et al., 2019; Turner-Evans et al., 2020), taking advantage of the spatiotemporal control in the presentation of visual stimuli. The situation is more technically

challenging in olfactory decision-making tasks, given the turbulent dynamics of odour plumes. I imagine a setup where streams of different odours, or the same odour at various concentrations, are carefully delivered to (and measured at) the antennae, prompting the fly to make a choice by 'running', or turning the ball, towards either side, while the activity of unstimulated or photostimulated $\boldsymbol{\alpha\beta_c}$ KCs is recorded. Odour delivery needs to be under closed-loop control, since the turning of the ball simulates running away from an odour for the fly. Because of the nature of the stimulus, it will still be extremely difficult to accurately define the odour interface (Pannunzi and Nowotny, 2019) — the best effort is perhaps to imitate the chamber environment by using two closely positioned half-chambers, minimising odour diffusion. Direct tracking of $\boldsymbol{\alpha\beta_c}$ KC activity using this kind of experimental setup will hopefully offer deeper insights into the subthreshold voltage- or spike-dependent mechanisms of temporal integration, as well as the noise correlations between populations of $\boldsymbol{\alpha\beta_c}$ KCs. A re-evaluation of the effects of optogenetic silencing will also be important to strengthen the argument of causality, given the inconclusive photoinhibition results. If the experimenter is more adventurous, neurally contingent, closed-loop optogenetics experiments can be attempted, in which the fly's choice is decoded and manipulated based on a model DV derived from population activity (Peixoto et al., 2021).

Appendix

List of primers

The primers follow the convention from 5' to 3'. FP: forward primer. RP: reverse primer. Red: restriction sites; blue: motif sequence; brown: flexible linker.

Dendritic targeting of Chrimson

Short motifs:
NotI – Chrimson::tdTom::Shal-motif – Acc65I
FP: ATAAGAATGCGGCCGCATGAGCAGACTGGTCGCCGCT
RP: TCCAATGCATTGGTTATTATTACGTTGTCTTCTCCAGACATCGCAGCAAATGATGGTGCTGCAGCTCGA
AGCCGCCGGAGCCGCCGGATTTATACAGTTCGTCCATACC

NotI – Chrimson::tdTom::RbTLCN-motif – Acc65I
FP: ATAAGAATGCGGCCGCATGAGCAGACTGGTCGCCGCT
RP: TCCAATGCATTGGTTATTATTAGGCGGAGGTCAGCTGGATGGCGAACACCTCGCCGCCGGCGGGGGACT
CGGCGCCGCCGGAGCCGCCGGATTTATACAGTTCGTCCATACC

NotI – Chrimson::tdTom::MsTLCN-motif – Acc65I
FP: ATAAGAATGCGGCCGCATGAGCAGACTGGTCGCCGCT
RP: TCCAATGCATTGGTTATTATTAGGAGGAGGTCAGCTGGATGGCGAACACCTCGCCGTCGGCGGGGGACT
CGGCGCCGCCGGAGCCGCCGGATTTATACAGTTCGTCCATACC

Long motifs — GeneArt constructs:
XhoI – NLG1-motif – Acc65I
CTCGAGGTGGTGCTGCGCACCGCCTGCCCCCCCGACTACACCCTGGCCATGCGCCGCTCCCCCGACGACGTGC
CCCTGATGACCCCCAACACCATCACCATGTAATAATAAGGTACC

XhoI – MLPH-motif – Acc65I
CTCGAGCGCGACCAGCCCCTGAACTCCAAGAAGAAGAAGCGCCTGCTGTCCTTCCGCGACGTGGACTTCGAG
GAGGACTCCGACTAATAATAAGGTACC

XhoI – AMPAR-motif – Acc65I
CTCGAGGAGTTCTGCTACAAGTCCCGCTCCGAGTCCAAGCGCATGAAGGGCTTCTGCCTGATCCCCCAGCAGT
CCATCAACGAGGCCATCCGCACCTCCACCCTGCCCCGCAACTCCGGCGCCTAATAATAAGGTACC

XhoI – nAChRα7-motif – Acc65I
CTCGAGGGCGAGGACAAGGTGCGCCCCGCCTGCCAGCACAAGCCCCGCCGCTGCTCCCTGGCCTCCGTGGAG
CTGTCCGCCGGCGCCGGCCCCCCCACCTCCAACGGCAACCTGCTGTACATCGGCTTCCGCGGCCTGGAGGG
CATGCACTAATAATAAGGTACC

XhoI – fusion-motif – Acc65I
CTCGAGCAGTCCCAGCCCATCCTGAACACCAAGGAGATGGCCCCCCAGTCCAAGCCCCCCGAGGAGCTGGA
GATGTCCTCCATGCCCTCCCCCGTGGCCCCCCTGCCCGCCCGCACCGAGGGCGTGATCGACATGCGCTCC
ATGTCCTCCATCGACTCCTTCATCTCCTGCGCCACCGACTTCCCCGAGGCCACCCGCTTCGGCTCCGGCTC
CGGCTCCGGCTCCGGCTCCGCCGAGTCCCCCGCCGACGGCGAGGTGTTCGCCATCCAGCTGACCTCCTCC
TAATAATAAGGTACC

Long motifs — fusion PCR:
Chrimson::tdTom::NLG1-motif
FP: ATAAGAATGCGGCCGCATGAGCAGACTGGTCGCCGCT
RP: GTCGGGGGGGCAGGCGGTGCGCAGCACCACGCCGCCGGAGCCGCCGGATTTATACAGTTCGTCCATACC
FP: TTTCTGTATGGTATGGACGAACTGTATAAATCCGGCGGCTCCGGCGGCGTGGTGCTGCGCACCGCCTGC
RP: TCCAATGCATTGGGGTACCTTATTATTACATGGTGATGGTGTT

Chrimson::tdTom::MLPH-motif
FP: ATAAGAATGCGGCCGCATGAGCAGACTGGTCGCCGCT
RP: CTTCTTCTTGGAGTTCAGGGGCTGGTCGCGGCCGCCGGAGCCGCCGGATTTATACAGTTCGTCCATACC
FP: TTTCTGTATGGTATGGACGAACTGTATAAATCCGGCGGCTCCGGCGGCCGCGACCAGCCCCTGAACTCC
RP: TCCAATGCATTGGGGTACCTTATTATTAGTCGGAGTCCTCCTC

Chrimson::tdTom::AMPAR-motif
FP: ATAAGAATGCGGCCGCATGAGCAGACTGGTCGCCGCT
RP: GGACTCGGAGCGGGACTTGTAGCAGAACTCGCCGCCGGAGCCGCCGGATTTATACAGTTCGTCCATACC
FP: TTTCTGTATGGTATGGACGAACTGTATAAATCCGGCGGCTCCGGCGGCGAGTTCTGCTACAAGTCCCGC
RP: TCCAATGCATTGGGGTACCTTATTATTAGGCGCCGGAGTTGCG

Chrimson::tdTom::nAChRα7-motif
FP: ATAAGAATGCGGCCGCATGAGCAGACTGGTCGCCGCT
RP: CTGGCAGGCGGGGCGCACCTTGTCCTCGCCGCCGCCGGAGCCGCCGGATTTATACAGTTCGTCCATACC
FP: TTTCTGTATGGTATGGACGAACTGTATAAATCCGGCGGCTCCGGCGGCGGCGAGGACAAGGTGCGCCCC
RP: TCCAATGCATTGGGGTACCTTATTATTAGTGCATGCCCTCCAG

Chrimson::tdTom::fusion-motif
FP: ATAAGAATGCGGCCGCATGAGCAGACTGGTCGCCGCT
RP: CTCCTTGGTGTTCAGGATGGGCTGGGACTGGCCGCCGGAGCCGCCGGATTTATACAGTTCGTCCATACC
FP: TTTCTGTATGGTATGGACGAACTGTATAAATCCGGCGGCTCCGGCGGCCAGTCCCAGCCCATCCTGAAC
RP: TCCAATGCATTGGGGTACCTTATTATTAGGAGGAGGTCAGCTG

Restricted expression of *Gt*ACR1

BgIII – FRT-stop-FRT – XhoI
FP: GGGGAAGATCTGAAGTTCCTATACTTTCTAGA
RP: CGCCGCTCGAGGAAGTTCCTATTCTCTAGAAA

References

Akrami, Athena, Charles D. Kopec, Mathew E. Diamond, and Carlos D. Brody (2018). "Posterior Parietal Cortex Represents Sensory History and Mediates Its Effects on Behaviour". *Nature* 554.7692, pp. 368–372.

Álvarez-Salvado, Efrén, Angela M Licata, Erin G Connor, Margaret K McHugh, Benjamin MN King, Nicholas Stavropoulos, Jonathan D Victor, John P Crimaldi, and Katherine I Nagel (2018). "Elementary Sensory-Motor Transformations Underlying Olfactory Navigation in Walking Fruit-Flies". *eLife* 7. Ed. by Ronald L Calabrese and Eve Marder, e37815.

Amin, Hoger, Anthi A Apostolopoulou, Raquel Suárez-Grimalt, Eleftheria Vrontou, and Andrew C Lin (2020). "Localized Inhibition in the Drosophila Mushroom Body". *eLife* 9. Ed. by Mani Ramaswami, Ronald L Calabrese, Mani Ramaswami, and Tamara Boto, e56954.

Andersen, R. A., C. Asanuma, G. Essick, and R. M. Siegel (1990). "Corticocortical Connections of Anatomically and Physiologically Defined Subdivisions within the Inferior Parietal Lobule". *Journal of Comparative Neurology* 296.1, pp. 65–113.

Aso, Yoshinori, Daisuke Hattori, Yang Yu, Rebecca M. Johnston, Nirmala A. Iyer, Teri-TB Ngo, Heather Dionne, L. F. Abbott, Richard Axel, Hiromu Tanimoto, and Gerald M. Rubin (2014a). "The Neuronal Architecture of the Mushroom Body Provides a Logic for Associative Learning". *eLife* 3, e04577.

Aso, Yoshinori, Divya Sitaraman, Toshiharu Ichinose, Karla R. Kaun, Katrin Vogt, Ghislain Belliart-Guérin, Pierre-Yves Plaçais, Alice A. Robie, Nobuhiro Yamagata, Christopher Schnaitmann, William J. Rowell, Rebecca M. Johnston, Teri-T. B. Ngo, Nan Chen, Wyatt Korff, Michael N. Nitabach, Ulrike Heberlein, Thomas Preat, Kristin M. Branson, Hiromu Tanimoto, and Gerald M. Rubin (2014b). "Mushroom Body Output Neurons Encode Valence and Guide Memory-Based Action Selection in Drosophila". *eLife* 3, e04580.

Bilz, Florian, Bart R. H. Geurten, Clare E. Hancock, Annekathrin Widmann, and André Fiala (2020). "Visualization of a Distributed Synaptic Memory Code in the Drosophila Brain". *Neuron*.

Blatt, G. J., R. A. Andersen, and G. R. Stoner (1990). "Visual Receptive Field Organization and Cortico-Cortical Connections of the Lateral Intraparietal Area (Area LIP) in the Macaque". *The Journal of Comparative Neurology* 299.4, pp. 421–445.

Bogacz, Rafal, Eric Brown, Jeff Moehlis, Philip Holmes, and Jonathan D. Cohen (2006). "The Physics of Optimal Decision Making: A Formal Analysis of Models of Performance in Two-Alternative Forced-Choice Tasks". *Psychological Review* 113.4, pp. 700–765.

Bouton, Mark E. (2004). "Context and Behavioral Processes in Extinction". *Learning & Memory (Cold Spring Harbor, N.Y.)* 11.5, pp. 485–494.

Britten, K. H., W. T. Newsome, M. N. Shadlen, S. Celebrini, and J. A. Movshon (1996). "A Relationship between Behavioral Choice and the Visual Responses of Neurons in Macaque MT". *Visual Neuroscience* 13.1, pp. 87–100.

Britten, K. H., M. N. Shadlen, W. T. Newsome, and J. A. Movshon (1992). "The Analysis of Visual Motion: A Comparison of Neuronal and Psychophysical Performance". *Journal of Neuroscience* 12.12, pp. 4745–4765.

Brody, Carlos D and Timothy D Hanks (2016). "Neural Underpinnings of the Evidence Accumulator". *Current Opinion in Neurobiology*. Neurobiology of Cognitive Behavior 37, pp. 149–157.

Brody, Carlos D., Adrián Hernández, Antonio Zainos, and Ranulfo Romo (2003). "Timing and Neural Encoding of Somatosensory Parametric Working Memory in Macaque Prefrontal Cortex". *Cerebral Cortex* 13.11, pp. 1196–1207.

Brunet, Lisa J., Geoffrey H. Gold, and John Ngai (1996). "General Anosmia Caused by a Targeted Disruption of the Mouse Olfactory Cyclic Nucleotide–Gated Cation Channel". *Neuron* 17.4, pp. 681–693.

Brunton, Bingni W., Matthew M. Botvinick, and Carlos D. Brody (2013). "Rats and Humans Can Optimally Accumulate Evidence for Decision-Making". *Science* 340.6128, pp. 95–98.

Cai, Xiang, Conrad W. Liang, Sukuman Muralidharan, Joseph P. Y. Kao, Cha-Min Tang, and Scott M. Thompson (2004). "Unique Roles of SK and Kv4.2 Potassium Channels in Dendritic Integration". *Neuron* 44.2, pp. 351–364.

Campbell, Robert A. A., Kyle S. Honegger, Hongtao Qin, Wanhe Li, Ebru Demir, and Glenn C. Turner (2013). "Imaging a Population Code for Odor Identity in the Drosophila Mushroom Body". *Journal of Neuroscience* 33.25, pp. 10568–10581.

Carandini, Matteo and Anne K. Churchland (2013). "Probing Perceptual Decisions in Rodents". *Nature Neuroscience* 16.7, p. 824.

Caron, Sophie J. C., Vanessa Ruta, L. F. Abbott, and Richard Axel (2013). "Random Convergence of Olfactory Inputs in the *Drosophila* Mushroom Body". *Nature* 497.7447, p. 113.

Chu, Po-Ju, Jacqueline F. Rivera, and Don B. Arnold (2006). "A Role for Kif17 in Transport of Kv4.2". *The Journal of Biological Chemistry* 281.1, pp. 365–373.

Cisek, Paul, Geneviève Aude Puskas, and Stephany El-Murr (2009). "Decisions in Changing Conditions: The Urgency-Gating Model". *Journal of Neuroscience* 29.37, pp. 11560–11571.

Claridge-Chang, Adam, Robert D. Roorda, Eleftheria Vrontou, Lucas Sjulson, Haiyan Li, Jay Hirsh, and Gero Miesenböck (2009). "Writing Memories with Light-Addressable Reinforcement Circuitry". *Cell* 139.2, pp. 405–415.

Clyne, Peter J., Coral G. Warr, Marc R. Freeman, Derek Lessing, Junhyong Kim, and John R. Carlson (1999). "A Novel Family of Divergent Seven-Transmembrane Proteins: Candidate Odorant Receptors in Drosophila". *Neuron* 22.2, pp. 327–338.

Cohen, Marlene R. and Adam Kohn (2011). "Measuring and Interpreting Neuronal Correlations". *Nature Neuroscience* 14.7, pp. 811–819.

Cohn, Raphael, Ianessa Morantte, and Vanessa Ruta (2015). "Coordinated and Compartmentalized Neuromodulation Shapes Sensory Processing in Drosophila". *Cell* 163.7, pp. 1742–1755.

Correia, Susana S., Silvia Bassani, Tyler C. Brown, Marie-France Lisé, Donald S. Backos, Alaa El-Husseini, Maria Passafaro, and José A. Esteban (2008). "Motor Protein-Dependent Transport of AMPA Receptors into Spines during Long-Term Potentiation". *Nature Neuroscience* 11.4, pp. 457–466.

Cunningham, John P. and Byron M. Yu (2014). "Dimensionality Reduction for Large-Scale Neural Recordings". *Nature Neuroscience* 17.11, pp. 1500–1509.

Currier, Timothy A. and Katherine I. Nagel (2020). "Multisensory Control of Navigation in the Fruit Fly". *Current Opinion in Neurobiology*. Systems Neuroscience 64, pp. 10–16.

DasGupta, Shamik, Clara Howcroft Ferreira, and Gero Miesenböck (2014). "FoxP Influences the Speed and Accuracy of a Perceptual Decision in Drosophila". *Science* 344.6186, pp. 901–904.

Demir, Mahmut, Nirag Kadakia, Hope D Anderson, Damon A Clark, and Thierry Emonet (2020). "Walking Drosophila Navigate Complex Plumes Using Stochastic Decisions Biased by the Timing of Odor Encounters". *eLife* 9. Ed. by Agnese Seminara, Ronald L Calabrese, Venkatesh N Murthy, and Antonio Celani, e57524.

Diao, Fengqiu, Jeremy Chaufty, Girma Waro, and Susan Tsunoda (2010). "SIDL Interacts with the Dendritic Targeting Motif of Shal (Kv4) K+ Channels in Drosophila". *Molecular and Cellular Neuroscience* 45.1, pp. 75–83.

Ditterich, Jochen, Mark E. Mazurek, and Michael N. Shadlen (2003). "Microstimulation of Visual Cortex Affects the Speed of Perceptual Decisions". *Nature Neuroscience* 6.8, pp. 891–898.

Dombeck, Daniel A. and Michael B. Reiser (2012). "Real Neuroscience in Virtual Worlds". *Current Opinion in Neurobiology*. Neurotechnology 22.1, pp. 3–10.

Drugowitsch, Jan, Rubén Moreno-Bote, Anne K. Churchland, Michael N. Shadlen, and Alexandre Pouget (2012). "The Cost of Accumulating Evidence in Perceptual Decision Making". *Journal of Neuroscience* 32.11, pp. 3612–3628.

Duan, Chunyu A., Marino Pagan, Alex T. Piet, Charles D. Kopec, Athena Akrami, Alexander J. Riordan, Jeffrey C. Erlich, and Carlos D. Brody (2021). "Collicular Circuits for Flexible Sensorimotor Routing". *Nature Neuroscience* 24.8, pp. 1110–1120.

Emiliani, Valentina, Adam E. Cohen, Karl Deisseroth, and Michael Häusser (2015). "All-Optical Interrogation of Neural Circuits". *Journal of Neuroscience* 35.41, pp. 13917–13926.

Endo, Keita, Yoshiko Tsuchimoto, and Hokto Kazama (2020). "Synthesis of Conserved Odor Object Representations in a Random, Divergent-Convergent Network". *Neuron* 108.2, 367–381.e5.

Evans, Dominic A., A. Vanessa Stempel, Ruben Vale, Sabine Ruehle, Yaara Lefler, and Tiago Branco (2018). "A Synaptic Threshold Mechanism for Computing Escape Decisions". *Nature* 558.7711, p. 590.

Farris, Sarah M. (2011). "Are Mushroom Bodies Cerebellum-like Structures?" *Arthropod Structure & Development*. Evolution of the Arthropod Nervous System: Part 2 40.4, pp. 368–379.

Feller, William (1968). *An Introduction to Probability Theory and Its Applications, Volume 1, 3rd Edition | Wiley*. 3rd. Vol. 1. New York, NY: Wiley.

Felsenberg, Johannes, Pedro F. Jacob, Thomas Walker, Oliver Barnstedt, Amelia J. Edmondson-Stait, Markus W. Pleijzier, Nils Otto, Philipp Schlegel, Nadiya Sharifi, Emmanuel Perisse, Carlas S. Smith, J. Scott Lauritzen, Marta Costa, Gregory S. X. E. Jefferis, Davi D. Bock, and Scott Waddell (2018). "Integration of Parallel Opposing Memories Underlies Memory Extinction". *Cell* 175.3, 709–722.e15.

Fişek, Mehmet and Rachel I. Wilson (2014). "Stereotyped Connectivity and Computations in Higher-Order Olfactory Neurons". *Nature Neuroscience* 17.2, pp. 280–288.

Fries, W. (1984). "Cortical Projections to the Superior Colliculus in the Macaque Monkey: A Retrograde Study Using Horseradish Peroxidase". *The Journal of Comparative Neurology* 230.1, pp. 55–76.

Fukuda, Mitsunori and Taruho S. Kuroda (2004). "Missense Mutations in the Globular Tail of Myosin-Va in Dilute Mice Partially Impair Binding of Slac2-a/Melanophilin". *Journal of Cell Science* 117.Pt 4, pp. 583–591.

Gamerman, Dani and Hedibert F. Lopes (2006). *Markov Chain Monte Carlo: Stochastic Simulation for Bayesian Inference, Second Edition*. Second. Chapman and Hall/CRC.

Gao, Qian and Andrew Chess (1999). "Identification of Candidate Drosophila Olfactory Receptors from Genomic DNA Sequence". *Genomics* 60.1, pp. 31–39.

Gao, Qian, Bingbing Yuan, and Andrew Chess (2000). "Convergent Projections of *Drosophila* Olfactory Neurons to Specific Glomeruli in the Antennal Lobe". *Nature Neuroscience* 3.8, p. 780.

Gold, Joshua I. and Michael N. Shadlen (2007). "The Neural Basis of Decision Making". *Annual Review of Neuroscience* 30.1, pp. 535–574.

Gorur-Shandilya, Srinivas, Mahmut Demir, Junjiajia Long, Damon A Clark, and Thierry Emonet (2017). "Olfactory Receptor Neurons Use Gain Control and Complementary Kinetics to Encode Intermittent Odorant Stimuli". *eLife* 6. Ed. by Fred Rieke, e27670.

Govorunova, Elena G., Oleg A. Sineshchekov, Roger Janz, Xiaoqin Liu, and John L. Spudich (2015). "Natural Light-Gated Anion Channels: A Family of Microbial Rhodopsins for Advanced Optogenetics". *Science*, aaa7484.

Groschner, Lukas N., Laura Chan Wah Hak, Rafal Bogacz, Shamik DasGupta, and Gero Miesenböck (2018). "Dendritic Integration of Sensory Evidence in Perceptual Decision-Making". *Cell* 0.0.

Groschner, Lukas N. and Gero Miesenböck (2019). "Mechanisms of Sensory Discrimination: Insights from Drosophila Olfaction". *Annual Review of Biophysics* 48.1, null.

Groszer, Matthias, David A. Keays, Robert M. J. Deacon, Joseph P. de Bono, Shweta Prasad-Mulcare, Simone Gaub, Muriel G. Baum, Catherine A. French, Jérôme Nicod,

Julie A. Coventry, Wolfgang Enard, Martin Fray, Steve D. M. Brown, Patrick M. Nolan, Svante Pääbo, Keith M. Channon, Rui M. Costa, Jens Eilers, Günter Ehret, J. Nicholas P. Rawlins, and Simon E. Fisher (2008). "Impaired Synaptic Plasticity and Motor Learning in Mice with a Point Mutation Implicated in Human Speech Deficits". *Current biology: CB* 18.5, pp. 354–362.

Gruntman, Eyal and Glenn C. Turner (2013). "Integration of the Olfactory Code across Dendritic Claws of Single Mushroom Body Neurons". *Nature neuroscience* 16.12, pp. 1821–1829.

Guo, Zengcai V., Nuo Li, Daniel Huber, Eran Ophir, Diego Gutnisky, Jonathan T. Ting, Guoping Feng, and Karel Svoboda (2014). "Flow of Cortical Activity Underlying a Tactile Decision in Mice". *Neuron* 81.1, pp. 179–194.

Haesler, Sebastian, Christelle Rochefort, Benjamin Georgi, Pawel Licznerski, Pavel Osten, and Constance Scharff (2007). "Incomplete and Inaccurate Vocal Imitation after Knockdown of FoxP2 in Songbird Basal Ganglia Nucleus Area X". *PLoS biology* 5.12, e321.

Hallem, Elissa A. and John R. Carlson (2006). "Coding of Odors by a Receptor Repertoire". *Cell* 125.1, pp. 143–160.

Hallem, Elissa A., Michael G. Ho, and John R. Carlson (2004). "The Molecular Basis of Odor Coding in the Drosophila Antenna". *Cell* 117.7, pp. 965–979.

Hamdan, Fadi F., Hussein Daoud, Daniel Rochefort, Amélie Piton, Julie Gauthier, Mathieu Langlois, Gila Foomani, Sylvia Dobrzeniecka, Marie-Odile Krebs, Ridha Joober, Ronald G. Lafrenière, Jean-Claude Lacaille, Laurent Mottron, Pierre Drapeau, Miriam H. Beauchamp, Michael S. Phillips, Eric Fombonne, Guy A. Rouleau, and Jacques L. Michaud (2010). "De Novo Mutations in FOXP1 in Cases with Intellectual Disability, Autism, and Language Impairment". *The American Journal of Human Genetics* 87.5, pp. 671–678.

Handler, Annie, Thomas G. W. Graham, Raphael Cohn, Ianessa Morantte, Andrew F. Siliciano, Jianzhi Zeng, Yulong Li, and Vanessa Ruta (2019). "Distinct Dopamine Receptor Pathways Underlie the Temporal Sensitivity of Associative Learning". *Cell* 178.1, 60–75.e19.

Hanks, Timothy D., Jochen Ditterich, and Michael N. Shadlen (2006). "Microstimulation of Macaque Area LIP Affects Decision-Making in a Motion Discrimination Task". *Nature Neuroscience* 9.5, pp. 682–689.

Hanks, Timothy D., Charles D. Kopec, Bingni W. Brunton, Chunyu A. Duan, Jeffrey C. Erlich, and Carlos D. Brody (2015). "Distinct Relationships of Parietal and Prefrontal Cortices to Evidence Accumulation". *Nature* 520.7546, pp. 220–223.

Hanks, Timothy D., Mark E. Mazurek, Roozbeh Kiani, Elisabeth Hopp, and Michael N. Shadlen (2011). "Elapsed Decision Time Affects the Weighting of Prior Probability in a Perceptual Decision Task". *Journal of Neuroscience* 31.17, pp. 6339–6352.

Hanks, Timothy D. and Christopher Summerfield (2017). "Perceptual Decision Making in Rodents, Monkeys, and Humans". *Neuron* 93.1, pp. 15–31.

Harvey, Christopher D., Philip Coen, and David W. Tank (2012). "Choice-Specific Sequences in Parietal Cortex during a Virtual-Navigation Decision Task". *Nature* 484.7392, pp. 62–68.

Heisenberg, Martin, Alexander Borst, Sibylle Wagner, and Duncan Byers (1985). "Drosophila Mushroom Body Mutants Are Deficient in Olfactory Learning". *Journal of Neurogenetics* 2.1, pp. 1–30.

Hernández, Adrián, Antonio Zainos, and Ranulfo Romo (2002). "Temporal Evolution of a Decision-Making Process in Medial Premotor Cortex". *Neuron* 33.6, pp. 959–972.

Hige, Toshihide, Yoshinori Aso, Mehrab N. Modi, Gerald M. Rubin, and Glenn C. Turner (2015). "Heterosynaptic Plasticity Underlies Aversive Olfactory Learning in Drosophila". *Neuron* 88.5, pp. 985–998.

Hildebrand, John G. and Gordon M. Shepherd (1997). "MECHANISMS OF OLFACTORY DISCRIMINATION: Converging Evidence for Common Principles Across Phyla". *Annual Review of Neuroscience* 20.1, pp. 595–631.

Hirokawa, Junya, Alexander Vaughan, Paul Masset, Torben Ott, and Adam Kepecs (2019). "Frontal Cortex Neuron Types Categorically Encode Single Decision Variables". *Nature* 576.7787, pp. 446–451.

Huk, Alexander C. and Michael N. Shadlen (2005). "Neural Activity in Macaque Parietal Cortex Reflects Temporal Integration of Visual Motion Signals during Perceptual Decision Making". *Journal of Neuroscience* 25.45, pp. 10420–10436.

Ito, Iori, Rose Chik-ying Ong, Baranidharan Raman, and Mark Stopfer (2008). "Sparse Odor Representation and Olfactory Learning". *Nature Neuroscience* 11.10, p. 1177.

Jacob, Pedro F. and Scott Waddell (2020). "Spaced Training Forms Complementary Long-Term Memories of Opposite Valence in Drosophila". *Neuron* 106.6, 977–991.e4.

Jeanne, James M. and Rachel I. Wilson (2015). "Convergence, Divergence, and Reconvergence in a Feedforward Network Improves Neural Speed and Accuracy". *Neuron* 88.5, pp. 1014–1026.

Jenett, Arnim, Gerald M. Rubin, Teri-T. B. Ngo, David Shepherd, Christine Murphy, Heather Dionne, Barret D. Pfeiffer, Amanda Cavallaro, Donald Hall, Jennifer Jeter, Nirmala Iyer, Dona Fetter, Joanna H. Hausenfluck, Hanchuan Peng, Eric T. Trautman, Robert R. Svirskas, Eugene W. Myers, Zbigniew R. Iwinski, Yoshinori Aso, Gina M. DePasquale, Adrianne Enos, Phuson Hulamm, Shing Chun Benny Lam, Hsing-Hsi Li, Todd R. Laverty, Fuhui Long, Lei Qu, Sean D. Murphy, Konrad Rokicki, Todd Safford, Kshiti Shaw, Julie H. Simpson, Allison Sowell, Susana Tae, Yang Yu, and Christopher T. Zugates (2012). "A GAL4-Driver Line Resource for Drosophila Neurobiology". *Cell Reports* 2.4, pp. 991–1001.

Johnston, W. Jeffrey, Stephanie E. Palmer, and David J. Freedman (2020). "Nonlinear Mixed Selectivity Supports Reliable Neural Computation". *PLOS Computational Biology* 16.2, e1007544.

Jun, Elizabeth J., Alex R. Bautista, Michael D. Nunez, Daicia C. Allen, Jung H. Tak, Eduardo Alvarez, and Michele A. Basso (2021). "Causal Role for the Primate Superior Colliculus in the Computation of Evidence for Perceptual Decisions". *Nature Neuroscience*, pp. 1–11.

Kadakia, Nirag and Thierry Emonet (2019). "Front-End Weber-Fechner Gain Control Enhances the Fidelity of Combinatorial Odor Coding". *eLife* 8. Ed. by Fred Rieke, Catherine Dulac, and Katherine I. Nagel, e45293.

Kanerva, Pentti (1988). *Sparse Distributed Memory*. Cambridge, MA, USA: MIT Press.

Kapitein, Lukas C., Max A. Schlager, Marijn Kuijpers, Phebe S. Wulf, Myrrhe van Spronsen, Frederick C. MacKintosh, and Casper C. Hoogenraad (2010). "Mixed Microtubules Steer Dynein-Driven Cargo Transport into Dendrites". *Current biology: CB* 20.4, pp. 290–299.

Kass, Robert E. and Larry Wasserman (1995). "A Reference Bayesian Test for Nested Hypotheses and Its Relationship to the Schwarz Criterion". *Journal of the American Statistical Association* 90.431, pp. 928–934.

Katz, Leor N., Jacob L. Yates, Jonathan W. Pillow, and Alexander C. Huk (2016). "Dissociated Functional Significance of Decision-Related Activity in the Primate Dorsal Stream". *Nature* 535.7611, pp. 285–288.

Keene, Alex C. and Scott Waddell (2007). "*Drosophila* Olfactory Memory: Single Genes to Complex Neural Circuits". *Nature Reviews Neuroscience* 8.5, p. 341.

Kempf, Anissa, Seoho M. Song, Clifford B. Talbot, and Gero Miesenböck (2019). "A Potassium Channel β-Subunit Couples Mitochondrial Electron Transport to Sleep". *Nature*, p. 1.

Kersten, Daniel, Pascal Mamassian, and Alan Yuille (2004). "Object Perception as Bayesian Inference". *Annual Review of Psychology* 55, pp. 271–304.

Kiani, Roozbeh, Christopher J. Cueva, John B. Reppas, and William T. Newsome (2014). "Dynamics of Neural Population Responses in Prefrontal Cortex Indicate Changes of Mind on Single Trials". *Current Biology* 24.13, pp. 1542–1547.

Kim, Sung Soo, Ann M. Hermundstad, Sandro Romani, L. F. Abbott, and Vivek Jayaraman (2019). "Generation of Stable Heading Representations in Diverse Visual Scenes". *Nature* 576.7785, pp. 126–131.

Klapoetke, Nathan C., Yasunobu Murata, Sung Soo Kim, Stefan R. Pulver, Amanda Birdsey-Benson, Yong Ku Cho, Tania K. Morimoto, Amy S. Chuong, Eric J. Carpenter, Zhijian Tian, Jun Wang, Yinlong Xie, Zhixiang Yan, Yong Zhang, Brian Y. Chow, Barbara Surek, Michael Melkonian, Vivek Jayaraman,

Martha Constantine-Paton, Gane Ka-Shu Wong, and Edward S. Boyden (2014). "Independent Optical Excitation of Distinct Neural Populations". *Nature Methods* 11.3, pp. 338–346.

Kobak, Dmitry, Wieland Brendel, Christos Constantinidis, Claudia E Feierstein, Adam Kepecs, Zachary F Mainen, Xue-Lian Qi, Ranulfo Romo, Naoshige Uchida, and Christian K Machens (2016). "Demixed Principal Component Analysis of Neural Population Data". *eLife* 5. Ed. by Mark CW van Rossum, e10989.

Konopka, Genevieve, Jamee M. Bomar, Kellen Winden, Giovanni Coppola, Zophonias O. Jonsson, Fuying Gao, Sophia Peng, Todd M. Preuss, James A. Wohlschlegel, and Daniel H. Geschwind (2009). "Human-Specific Transcriptional Regulation of CNS Development Genes by FOXP2". *Nature* 462.7270, pp. 213–217.

Kurtovic, Amina, Alexandre Widmer, and Barry J. Dickson (2007). "A Single Class of Olfactory Neurons Mediates Behavioural Responses to a Drosophila Sex Pheromone". *Nature* 446.7135, pp. 542–546.

Kvon, Evgeny Z., Tomas Kazmar, Gerald Stampfel, J. Omar Yáñez-Cuna, Michaela Pagani, Katharina Schernhuber, Barry J. Dickson, and Alexander Stark (2014). "Genome-Scale Functional Characterization of *Drosophila* Developmental Enhancers *in Vivo*". *Nature* 512.7512, p. 91.

Kyriazi, Pinelopi, Drew B. Headley, and Denis Pare (2018). "Multi-Dimensional Coding by Basolateral Amygdala Neurons". *Neuron* 99.6, 1315–1328.e5.

Lai, Cecilia S. L., Simon E. Fisher, Jane A. Hurst, Faraneh Vargha-Khadem, and Anthony P. Monaco (2001). "A Forkhead-Domain Gene Is Mutated in a Severe Speech and Language Disorder". *Nature* 413.6855, pp. 519–523.

Lasiecka, Zofia M. and Bettina Winckler (2011). "Mechanisms of Polarized Membrane Trafficking in Neurons — Focusing in on Endosomes". *Molecular and Cellular Neuroscience*. Membrane Trafficking and Cytoskeletal Dynamics in Neuronal Function 48.4, pp. 278–287.

Latimer, Kenneth W., Jacob L. Yates, Miriam L. R. Meister, Alexander C. Huk, and Jonathan W. Pillow (2015). "Single-Trial Spike Trains in Parietal Cortex Reveal Discrete Steps during Decision-Making". *Science* 349.6244, pp. 184–187.

Lewis, Tommy L., Tianyi Mao, Karel Svoboda, and Don B. Arnold (2009). "Myosin-Dependent Targeting of Transmembrane Proteins to Neuronal Dendrites". *Nature Neuroscience* 12.5, p. 568.

Li, Feng, Jack W Lindsey, Elizabeth C Marin, Nils Otto, Marisa Dreher, Georgia Dempsey, Ildiko Stark, Alexander S Bates, Markus William Pleijzier, Philipp Schlegel, Aljoscha Nern, Shin-ya Takemura, Nils Eckstein, Tansy Yang, Audrey Francis, Amalia Braun, Ruchi Parekh, Marta Costa, Louis K Scheffer, Yoshinori Aso, Gregory SXE Jefferis, Larry F Abbott, Ashok Litwin-Kumar, Scott Waddell, and Gerald M Rubin (2020). "The Connectome of the Adult Drosophila Mushroom Body Provides Insights into Function". *eLife* 9. Ed. by Leslie C Griffith, Eve Marder, Leslie C Griffith, Jason Pipkin, and Chris Q Doe, e62576.

Lin, Andrew C., Alexei M. Bygrave, Alix de Calignon, Tzumin Lee, and Gero Miesenböck (2014). "Sparse, Decorrelated Odor Coding in the Mushroom Body Enhances Learned Odor Discrimination". *Nature Neuroscience* 17.4, p. 559.

Lin, Michael Z. and Mark J. Schnitzer (2016). "Genetically Encoded Indicators of Neuronal Activity". *Nature Neuroscience* 19.9, pp. 1142–1153.

Litwin-Kumar, Ashok, Kameron Decker Harris, Richard Axel, Haim Sompolinsky, and L. F. Abbott (2017). "Optimal Degrees of Synaptic Connectivity". *Neuron* 93.5, 1153–1164.e7.

Loesche, Frank and Michael B. Reiser (2021). "An Inexpensive, High-Precision, Modular Spherical Treadmill Setup Optimized for Drosophila Experiments". *Frontiers in Behavioral Neuroscience* 15, p. 138.

Mahn, Mathias, Lihi Gibor, Pritish Patil, Katayun Cohen-Kashi Malina, Shir Oring, Yoav Printz, Rivka Levy, Ilan Lampl, and Ofer Yizhar (2018). "High-Efficiency Optogenetic Silencing with Soma-Targeted Anion-Conducting Channelrhodopsins". *Nature Communications* 9.1, p. 4125.

Malyshev, A. Y., M. V. Roshchin, G. R. Smirnova, D. A. Dolgikh, P. M. Balaban, and M. A. Ostrovsky (2017). "Chloride Conducting Light Activated Channel GtACR2 Can Produce Both Cessation of Firing and Generation of Action Potentials in Cortical Neurons in Response to Light". *Neuroscience Letters* 640, pp. 76–80.

Marr, David (1969). "A Theory of Cerebellar Cortex". *The Journal of Physiology* 202.2, pp. 437–470.

Mauss, Alex S., Christian Busch, and Alexander Borst (2017). "Optogenetic Neuronal Silencing in Drosophila during Visual Processing". *Scientific Reports* 7.1, p. 13823.

Meister, Miriam L. R., Jay A. Hennig, and Alexander C. Huk (2013). "Signal Multiplexing and Single-Neuron Computations in Lateral Intraparietal Area During Decision-Making". *Journal of Neuroscience* 33.6, pp. 2254–2267.

Messier, Jessica E, Hongmei Chen, Zhao-Lin Cai, and Mingshan Xue (2018). "Targeting Light-Gated Chloride Channels to Neuronal Somatodendritic Domain Reduces Their Excitatory Effect in the Axon". *eLife* 7. Ed. by Indira M Raman and Gary L Westbrook, e38506.

Miesenböck, Gero (2009). "The Optogenetic Catechism". *Science* 326.5951, pp. 395–399.

Mitsui, Sachiko, Michiko Saito, Ken Hayashi, Kensaku Mori, and Yoshihiro Yoshihara (2005). "A Novel Phenylalanine-Based Targeting Signal Directs Telencephalin to Neuronal Dendrites". *Journal of Neuroscience* 25.5, pp. 1122–1131.

Mohammad, Farhan, James C. Stewart, Stanislav Ott, Katarina Chlebikova, Jia Yi Chua, Tong-Wey Koh, Joses Ho, and Adam Claridge-Chang (2017). "Optogenetic Inhibition of Behavior with Anion Channelrhodopsins". *Nature Methods* 14.3, pp. 271–274.

Mori, Kensaku and Hitoshi Sakano (2021). "Olfactory Circuitry and Behavioral Decisions". *Annual Review of Physiology* 83.1, pp. 231–256.

Mountcastle, V. B., M. A. Steinmetz, and R. Romo (1990). "Frequency Discrimination in the Sense of Flutter: Psychophysical Measurements Correlated with Postcentral Events in Behaving Monkeys". *Journal of Neuroscience* 10.9, pp. 3032–3044.

Murthy, Mala, Ila Fiete, and Gilles Laurent (2008). "Testing Odor Response Stereotypy in the Drosophila Mushroom Body". *Neuron* 59.6, pp. 1009–1023.

Nagel, Katherine I. and Rachel I. Wilson (2011). "Biophysical Mechanisms Underlying Olfactory Receptor Neuron Dynamics". *Nature Neuroscience* 14.2, pp. 208–216.

Nern, Aljoscha, Barret D. Pfeiffer, Karel Svoboda, and Gerald M. Rubin (2011). "Multiple New Site-Specific Recombinases for Use in Manipulating Animal Genomes". *Proceedings of the National Academy of Sciences* 108.34, pp. 14198–14203.

Newsome, William T., Kenneth H. Britten, and J. Anthony Movshon (1989). "Neuronal Correlates of a Perceptual Decision". *Nature* 341.6237, pp. 52–54.

Newville, Matthew, Till Stensitzki, Daniel B. Allen, Michal Rawlik, Antonino Ingargiola, and Andrew Nelson (2016). "Lmfit: Non-Linear Least-Square Minimization and Curve-Fitting for Python". *Astrophysics Source Code Library*, ascl:1606.014.

Nicolaï, Laura J. J., Ariane Ramaekers, Tim Raemaekers, Andrzej Drozdzecki, Alex S. Mauss, Jiekun Yan, Matthias Landgraf, Wim Annaert, and Bassem A. Hassan (2010). "Genetically Encoded Dendritic Marker Sheds Light on Neuronal Connectivity in Drosophila". *Proceedings of the National Academy of Sciences* 107.47, pp. 20553–20558.

Nojima, Tetsuya, Annika Rings, Aaron M. Allen, Nils Otto, Thomas A. Verschut, Jean-Christophe Billeter, Megan C. Neville, and Stephen F. Goodwin (2021). "A Sex-Specific Switch between Visual and Olfactory Inputs Underlies Adaptive Sex Differences in Behavior". *Current Biology* 31.6, 1175–1191.e6.

Okazawa, Gouki, Christina E. Hatch, Allan Mancoo, Christian K. Machens, and Roozbeh Kiani (2021). "Representational Geometry of Perceptual Decisions in the Monkey Parietal Cortex". *Cell* 184.14, 3748–3761.e18.

Olsen, Shawn R., Vikas Bhandawat, and Rachel I. Wilson (2007). "Excitatory Interactions between Olfactory Processing Channels in the Drosophila Antennal Lobe". *Neuron* 54.1, pp. 89–103.

— (2010). "Divisive Normalization in Olfactory Population Codes". *Neuron* 66.2, pp. 287–299.

Osterweil, Emily, David G. Wells, and Mark S. Mooseker (2005). "A Role for Myosin VI in Postsynaptic Structure and Glutamate Receptor Endocytosis". *The Journal of Cell Biology* 168.2, pp. 329–338.

Owald, David, Johannes Felsenberg, Clifford B. Talbot, Gaurav Das, Emmanuel Perisse, Wolf Huetteroth, and Scott Waddell (2015). "Activity of Defined Mushroom Body Output Neurons Underlies Learned Olfactory Behavior in Drosophila". *Neuron* 86.2, pp. 417–427.

Owald, David and Scott Waddell (2015). "Olfactory Learning Skews Mushroom Body Output Pathways to Steer Behavioral Choice in Drosophila". *Current Opinion in Neurobiology.* Circuit Plasticity and Memory 35, pp. 178–184.

Palmer, John, Alexander C. Huk, and Michael N. Shadlen (2005). "The Effect of Stimulus Strength on the Speed and Accuracy of a Perceptual Decision". *Journal of Vision* 5.5, pp. 1–1.

Pannunzi, Mario and Thomas Nowotny (2019). "Odor Stimuli: Not Just Chemical Identity". *Frontiers in Physiology* 10, p. 1428.

Papadopoulou, Maria, Stijn Cassenaer, Thomas Nowotny, and Gilles Laurent (2011). "Normalization for Sparse Encoding of Odors by a Wide-Field Interneuron". *Science* 332.6030, pp. 721–725.

Park, Il Memming, Miriam L. R. Meister, Alexander C. Huk, and Jonathan W. Pillow (2014). "Encoding and Decoding in Parietal Cortex during Sensorimotor Decision-Making". *Nature Neuroscience* 17.10, pp. 1395–1403.

Parnas, Moshe, Andrew C. Lin, Wolf Huetteroth, and Gero Miesenböck (2013). "Odor Discrimination in Drosophila: From Neural Population Codes to Behavior". *Neuron* 79.5, pp. 932–944.

Parthasarathy, Aishwarya, Roger Herikstad, Jit Hon Bong, Felipe Salvador Medina, Camilo Libedinsky, and Shih-Cheng Yen (2017). "Mixed Selectivity Morphs Population Codes in Prefrontal Cortex". *Nature Neuroscience* 20.12, pp. 1770–1779.

Pavlou, Hania J and Stephen F Goodwin (2013). "Courtship Behavior in Drosophila Melanogaster: Towards a 'Courtship Connectome'". *Current Opinion in Neurobiology.* Neurogenetics 23.1, pp. 76–83.

Peixoto, Diogo, Jessica R. Verhein, Roozbeh Kiani, Jonathan C. Kao, Paul Nuyujukian, Chandramouli Chandrasekaran, Julian Brown, Sania Fong, Stephen I. Ryu, Krishna V. Shenoy, and William T. Newsome (2021). "Decoding and Perturbing Decision States in Real Time". *Nature*, pp. 1–6.

Petreanu, Leopoldo, Daniel Huber, Aleksander Sobczyk, and Karel Svoboda (2007). "Channelrhodopsin-2–Assisted Circuit Mapping of Long-Range Callosal Projections". *Nature Neuroscience* 10.5, pp. 663–668.

Pfeiffer, Barret D., Teri-T. B. Ngo, Karen L. Hibbard, Christine Murphy, Arnim Jenett, James W. Truman, and Gerald M. Rubin (2010). "Refinement of Tools for Targeted Gene Expression in Drosophila". *Genetics* 186.2, pp. 735–755.

Pimentel, Diogo, Jeffrey M. Donlea, Clifford B. Talbot, Seoho M. Song, Alexander J. F. Thurston, and Gero Miesenböck (2016). "Operation of a Homeostatic Sleep Switch". *Nature* 536.7616, pp. 333–337.

Platt, Michael L. and Paul W. Glimcher (1999). "Neural Correlates of Decision Variables in Parietal Cortex". *Nature* 400.6741, pp. 233–238.

Quinn, William G., William A. Harris, and Seymour Benzer (1974). "Conditioned Behavior in Drosophila Melanogaster". *Proceedings of the National Academy of Sciences of the United States of America* 71.3, pp. 708–712.

Raposo, David, Matthew T. Kaufman, and Anne K. Churchland (2014). "A Category-Free Neural Population Supports Evolving Demands during Decision-Making". *Nature Neuroscience* 17.12, pp. 1784–1792.

Ratcliff, Roger and Philip L. Smith (2004). "A Comparison of Sequential Sampling Models for Two-Choice Reaction Time". *Psychological Review* 111.2, pp. 333–367.

Ratcliff, Roger, Philip L. Smith, Scott D. Brown, and Gail McKoon (2016). "Diffusion Decision Model: Current Issues and History". *Trends in Cognitive Sciences* 20.4, pp. 260–281.

Ratcliff, Roger, Philip L. Smith, and Gail McKoon (2015). "Modeling Regularities in Response Time and Accuracy Data With the Diffusion Model". *Current Directions in Psychological Science* 24.6, pp. 458–470.

Resulaj, Arbora, Sarah Ruediger, Shawn R Olsen, and Massimo Scanziani (2018). "First Spikes in Visual Cortex Enable Perceptual Discrimination". *eLife* 7. Ed. by Inna Slutsky, e34044.

Rigotti, Mattia, Omri Barak, Melissa R. Warden, Xiao-Jing Wang, Nathaniel D. Daw, Earl K. Miller, and Stefano Fusi (2013). "The Importance of Mixed Selectivity in Complex Cognitive Tasks". *Nature* 497.7451, pp. 585–590.

Rivera, Jacqueline F., Shoeb Ahmad, Michael W. Quick, Emily R. Liman, and Don B. Arnold (2003). "An Evolutionarily Conserved Dileucine Motif in Shal K+ Channels Mediates Dendritic Targeting". *Nature Neuroscience* 6.3, pp. 243–250.

Roitman, Jamie D. and Michael N. Shadlen (2002). "Response of Neurons in the Lateral Intraparietal Area during a Combined Visual Discrimination Reaction Time Task". *Journal of Neuroscience* 22.21, pp. 9475–9489.

Romo, Ranulfo, Adrián Hernández, and Antonio Zainos (2004). "Neuronal Correlates of a Perceptual Decision in Ventral Premotor Cortex". *Neuron* 41.1, pp. 165–173.

Romo, Ranulfo, Adrián Hernández, Antonio Zainos, Luis Lemus, and Carlos D. Brody (2002). "Neuronal Correlates of Decision-Making in Secondary Somatosensory Cortex". *Nature Neuroscience* 5.11, pp. 1217–1225.

Rosales, Carlos R., Kyle D. Osborne, Griselda V. Zuccarino, Peter Scheiffele, and Michael A. Silverman (2005). "A Cytoplasmic Motif Targets Neuroligin-1 Exclusively to Dendrites of Cultured Hippocampal Neurons". *European Journal of Neuroscience* 22.9, pp. 2381–2386.

Rost, Benjamin R., Franziska Schneider-Warme, Dietmar Schmitz, and Peter Hegemann (2017). "Optogenetic Tools for Subcellular Applications in Neuroscience". *Neuron* 96.3, pp. 572–603.

Ruberti, Francesca and Carlos G. Dotti (2000). "Involvement of the Proximal C Terminus of the AMPA Receptor Subunit GluR1 in Dendritic Sorting". *Journal of Neuroscience* 20.11, RC78–RC78.

Salzman, C. D., Kenneth H. Britten, and William T. Newsome (1990). "Cortical Microstimulation Influences Perceptual Judgements of Motion Direction". *Nature* 346.6280, pp. 174–177.

Salzman, C. D., C. M. Murasugi, K. H. Britten, and W. T. Newsome (1992). "Microstimulation in Visual Area MT: Effects on Direction Discrimination Performance". *Journal of Neuroscience* 12.6, pp. 2331–2355.

Sato, Koji, Maurizio Pellegrino, Takao Nakagawa, Tatsuro Nakagawa, Leslie B. Vosshall, and Kazushige Touhara (2008). "Insect Olfactory Receptors Are Heteromeric Ligand-Gated Ion Channels". *Nature* 452.7190, p. 1002.

Scott, Benjamin B., Christine M. Constantinople, Athena Akrami, Timothy D. Hanks, Carlos D. Brody, and David W. Tank (2017). "Fronto-Parietal Cortical Circuits Encode Accumulated Evidence with a Diversity of Timescales". *Neuron* 95.2, 385–398.e5.

Seelig, Johannes D., M. Eugenia Chiappe, Gus K. Lott, Anirban Dutta, Jason E. Osborne, Michael B. Reiser, and Vivek Jayaraman (2010). "Two-Photon Calcium Imaging from Head-Fixed Drosophila during Optomotor Walking Behavior". *Nature Methods* 7.7, pp. 535–540.

Séjourné, Julien, Pierre-Yves Plaçais, Yoshinori Aso, Igor Siwanowicz, Séverine Trannoy, Vladimiros Thoma, Stevanus R. Tedjakumala, Gerald M. Rubin, Paul Tchénio, Kei Ito, Guillaume Isabel, Hiromu Tanimoto, and Thomas Preat (2011). "Mushroom Body Efferent Neurons Responsible for Aversive Olfactory Memory Retrieval in *Drosophila*". *Nature Neuroscience* 14.7, pp. 903–910.

Shadlen, Michael N. and Roozbeh Kiani (2013). "Decision Making as a Window on Cognition". *Neuron* 80.3, pp. 791–806.

Shemesh, Or A., Dimitrii Tanese, Valeria Zampini, Changyang Linghu, Kiryl Piatkevich, Emiliano Ronzitti, Eirini Papagiakoumou, Edward S. Boyden, and Valentina Emiliani (2017). "Temporally Precise Single-Cell-Resolution Optogenetics". *Nature Neuroscience* 20.12, pp. 1796–1806.

Spiess, Andrej-Nikolai and Natalie Neumeyer (2010). "An Evaluation of R2 as an Inadequate Measure for Nonlinear Models in Pharmacological and Biochemical Research: A Monte Carlo Approach". *BMC Pharmacology* 10.1, p. 6.

Stevens, Charles F. (2015). "What the Fly's Nose Tells the Fly's Brain". *Proceedings of the National Academy of Sciences* 112.30, pp. 9460–9465.

Stine, Gabriel M, Ariel Zylberberg, Jochen Ditterich, and Michael N Shadlen (2020). "Differentiating between Integration and Non-Integration Strategies in Perceptual Decision Making". *eLife* 9. Ed. by Valentin Wyart, Michael J Frank, Valentin Wyart, and Marius Usher, e55365.

Störtkuhl, Klemens F., Bernhard T. Hovemann, and John R. Carlson (1999). "Olfactory Adaptation Depends on the Trp Ca2+Channel in Drosophila". *Journal of Neuroscience* 19.12, pp. 4839–4846.

Strauss, Roland (2002). "The Central Complex and the Genetic Dissection of Locomotor Behaviour". *Current Opinion in Neurobiology* 12.6, pp. 633–638.

Su, Hailing and Diane K. O'Dowd (2003). "Fast Synaptic Currents in Drosophila Mushroom Body Kenyon Cells Are Mediated by $\boldsymbol{\alpha}$-Bungarotoxin-Sensitive Nicotinic Acetylcholine Receptors and Picrotoxin-Sensitive GABA Receptors". *Journal of Neuroscience* 23.27, pp. 9246–9253.

Sugrue, Leo P., Greg S. Corrado, and William T. Newsome (2004). "Matching Behavior and the Representation of Value in the Parietal Cortex". *Science* 304.5678, pp. 1782–1787.

Sun, Yuanjie, Rong Qiu, Xiaonan Li, Yaxin Cheng, Shan Gao, Fanchen Kong, Li Liu, and Yan Zhu (2020). "Social Attraction in Drosophila Is Regulated by the Mushroom Body and Serotonergic System". *Nature Communications* 11.1, p. 5350.

Szyszka, Paul, Richard C. Gerkin, C. Giovanni Galizia, and Brian H. Smith (2014). "High-Speed Odor Transduction and Pulse Tracking by Insect Olfactory Receptor Neurons". *Proceedings of the National Academy of Sciences* 111.47, pp. 16925–16930.

Tanaka, Nobuaki K., Hiromu Tanimoto, and Kei Ito (2008). "Neuronal Assemblies of the Drosophila Mushroom Body". *Journal of Comparative Neurology* 508.5, pp. 711–755.

Tomchik, Seth M. and Ronald L. Davis (2009). "Dynamics of Learning-Related cAMP Signaling and Stimulus Integration in the Drosophila Olfactory Pathway". *Neuron* 64.4, pp. 510–521.

Tóth, Judit, Mihály Kovács, Fei Wang, László Nyitray, and James R. Sellers (2005). "Myosin V from Drosophila Reveals Diversity of Motor Mechanisms within the Myosin V Family". *The Journal of Biological Chemistry* 280.34, pp. 30594–30603.

Treves, Alessandro and Edmund T Rolls (1991). "What Determines the Capacity of Autoassociative Memories in the Brain?" *Network: Computation in Neural Systems* 2.4, pp. 371–397.

Turner, Glenn C., Maxim Bazhenov, and Gilles Laurent (2008). "Olfactory Representations by Drosophila Mushroom Body Neurons". *Journal of Neurophysiology*.

Turner-Evans, Daniel B., Kristopher T. Jensen, Saba Ali, Tyler Paterson, Arlo Sheridan, Robert P. Ray, Tanya Wolff, J. Scott Lauritzen, Gerald M. Rubin, Davi D. Bock, and Vivek Jayaraman (2020). "The Neuroanatomical Ultrastructure and Function of a Biological Ring Attractor". *Neuron* 108.1, 145–163.e10.

Uchida, Naoshige, Adam Kepecs, and Zachary F. Mainen (2006). "Seeing at a Glance, Smelling in a Whiff: Rapid Forms of Perceptual Decision Making". *Nature Reviews Neuroscience* 7.6, pp. 485–491.

Uchida, Naoshige and Zachary F. Mainen (2003). "Speed and Accuracy of Olfactory Discrimination in the Rat". *Nature Neuroscience* 6.11, p. 1224.

Vickers, D. (1970). "Evidence for an Accumulator Model of Psychophysical Discrimination". *Ergonomics* 13.1, pp. 37–58.

Villette, Vincent, Mariya Chavarha, Ivan K. Dimov, Jonathan Bradley, Lagnajeet Pradhan, Benjamin Mathieu, Stephen W. Evans, Simon Chamberland, Dongqing Shi, Renzhi Yang, Benjamin B. Kim, Annick Ayon, Abdelali Jalil, François St-Pierre, Mark J. Schnitzer, Guoqiang Bi, Katalin Toth, Jun Ding, Stéphane Dieudonné, and Michael Z. Lin (2019). "Ultrafast Two-Photon Imaging of a High-Gain Voltage Indicator in Awake Behaving Mice". *Cell* 179.7, 1590–1608.e23.

Vosshall, Leslie B., Hubert Amrein, Pavel S. Morozov, Andrey Rzhetsky, and Richard Axel (1999). "A Spatial Map of Olfactory Receptor Expression in the Drosophila Antenna". *Cell* 96.5, pp. 725–736.

Vosshall, Leslie B., Allan M. Wong, and Richard Axel (2000). "An Olfactory Sensory Map in the Fly Brain". *Cell* 102.2, pp. 147–159.

Vrontou, Eleftheria, Lukas N. Groschner, Susanne Szydlowski, Ruth Brain, Alina Krebbers, and Gero Miesenböck (2021). "Response Competition between Neurons and Antineurons in the Mushroom Body". *Current Biology* 0.0.

Wald, Abraham (1947). *Sequential Analysis*. Sequential Analysis. Oxford, England: John Wiley, pp. xii, 212.

Wei, Aguan, Manuel Covarrubias, Alice Butler, Keith Baker, Michael Pak, and Lawrence Salkoff (1990). "K+ Current Diversity Is Produced by an Extended Gene Family Conserved in Drosophila and Mouse". *Science* 248.4955, pp. 599–603.

Wicher, Dieter, Ronny Schäfer, René Bauernfeind, Marcus C. Stensmyr, Regine Heller, Stefan H. Heinemann, and Bill S. Hansson (2008). "*Drosophila* Odorant Receptors Are Both Ligand-Gated and Cyclic-Nucleotide-Activated Cation Channels". *Nature* 452.7190, p. 1007.

Wiecki, Thomas V., Imri Sofer, and Michael J. Frank (2013). "HDDM: Hierarchical Bayesian Estimation of the Drift-Diffusion Model in Python". *Frontiers in Neuroinformatics* 7.

Wu, Chaowen, Elena Ivanova, Yi Zhang, and Zhuo-Hua Pan (2013). "rAAV-Mediated Subcellular Targeting of Optogenetic Tools in Retinal Ganglion Cells In Vivo". *PLOS ONE* 8.6, e66332.

Xu, Jian, Yongling Zhu, and Stephen F. Heinemann (2006). "Identification of Sequence Motifs That Target Neuronal Nicotinic Receptors to Dendrites and Axons". *Journal of Neuroscience* 26.38, pp. 9780–9793.

Yartsev, Michael M, Timothy D Hanks, Alice Misun Yoon, and Carlos D Brody (2018). "Causal Contribution and Dynamical Encoding in the Striatum during Evidence Accumulation". *eLife* 7. Ed. by Joshua I Gold, Timothy E Behrens, Joshua I Gold, and Mark D Humphries, e34929.

Yates, Jacob L., Il Memming Park, Leor N. Katz, Jonathan W. Pillow, and Alexander C. Huk (2017). "Functional Dissection of Signal and Noise in MT and LIP during Decision-Making". *Nature Neuroscience* 20.9, p. 1285.

Zhang, Zihui, Lloyd E. Russell, Adam M. Packer, Oliver M. Gauld, and Michael Häusser (2018). "Closed-Loop All-Optical Interrogation of Neural Circuits in Vivo". *Nature Methods* 15.12, pp. 1037–1040.

Zhou, Yang and David J. Freedman (2019). "Posterior Parietal Cortex Plays a Causal Role in Perceptual and Categorical Decisions". *Science* 365.6449, pp. 180–185.

Zhou, Yang, Matthew C Rosen, Sruthi K Swaminathan, Nicolas Y Masse, Ou Zhu, and David J Freedman (2021). "Distributed Functions of Prefrontal and Parietal Cortices during Sequential Categorical Decisions". *eLife* 10. Ed. by Anna Wang Roe, Joshua I Gold, and Klaus Wimmer, e58782.

Zohary, Ehud, Michael N. Shadlen, and William T. Newsome (1994). "Correlated Neuronal Discharge Rate and Its Implications for Psychophysical Performance". *Nature* 370.6485, pp. 140–143.

Zoltowski, David M., Kenneth W. Latimer, Jacob L. Yates, Alexander C. Huk, and Jonathan W. Pillow (2019). "Discrete Stepping and Nonlinear Ramping Dynamics Underlie Spiking Responses of LIP Neurons during Decision-Making". *Neuron* 102.6, 1249–1258.e10.